Andreas Kammel

Analysis of zonal flow bifurcations in 3D drift wave turbulence simulations

TECHNISCHE UNIVERSITÄT MÜNCHEN
Max-Planck-Institut für Plasmaphysik

Analysis of zonal flow bifurcations in 3D drift wave turbulence simulations

Andreas Kammel

Vollständiger Abdruck der von der Fakultät für Physik
der Technischen Universität München
zur Erlangung des akademischen Grades eines
Doktors der Naturwissenschaften (Dr. rer. nat.)
genehmigten Dissertation.

Vorsitzender: Univ.-Prof. Dr. Rudolf Gross
Prüfer der Dissertation:
1. Priv.-Doz. Dr. Klaus Hallatschek
2. Univ.-Prof. Dr. Harald Friedrich

Die Dissertation wurde am 13.06.2012 bei der Technischen Universität München
eingereicht und durch die Fakultät für Physik am 12.09.2012 angenommen.

Abstract

The main issue of experimental magnetic fusion devices lies with their inherently high turbulent transport, preventing long-term plasma confinement. A deeper understanding of the underlying transport processes is therefore desirable, especially in the high-gradient tokamak edge which marks the location of the drift wave regime as well as the outer boundary of the still badly understood high confinement mode. One of the most promising plasma features possibly connected to a complete bifurcation theory for the transition to this H-mode is found in large-scale phenomena capable of regulating radial transport through vortex shearing - i.e. zonal flows, linearly stable large-scale poloidal $\vec{E} \times \vec{B}$-modes based on radial flux surface averages of the potential gradient generated through turbulent self-organization.

Despite their relevance, few detailed turbulence studies of drift wave-based zonal flows have been undertaken, and none of them have explicitly targeted bifurcations - or, within a resistive sheared-slab environment, observed zonal flows at all. In this work, both analytical means and the two-fluid code NLET are used to analyze a reduced set of Hasegawa-Wakatani equations, describing a sheared collisional drift wave system without curvature. The characteristics of the drift waves themselves, as well as those of the drift wave-based zonal flows and their retroaction on the drift wave turbulence are examined. The single dimensionless parameter $\hat{\rho}_s$ proposed in previous analytical models is examined numerically and shown to divide the drift wave scale into two transport regimes, the behavioral characteristics of which agree perfectly with theoretical expectations. This transport transition correlates with a transition from pure drift wave turbulence at low $\hat{\rho}_s$ into the high-$\hat{\rho}_s$ zonal flow regime. The associated threshold has been more clearly identified by tracing it back to a tipping of the ratio between a newly proposed frequency gradient length at the resonances and the shear flow gradient length, leading to Reynolds stress asymmetries.

In the zonal flow regime, shear flow-dependency of the radial group velocity results in a quantitative expression of the repulsion of drift wave turbulence by zonal flows moving opposite to the electron diamagnetic drift direction (dubbed negative flows) and attraction around the positive flows. The transport bifurcation anticipated to ensue - expressed through density corrugations and asymmetric flows - is confirmed numerically and subsequently analyzed in great detail, marking the first finding of such a bifurcation within a self-consistent drift wave turbulence simulation. If these bifurcations were to be reproduced in an actual fusion device, improvements of confinement due to increased negative flow repulsion as well as shear flow stalling effects might be feasible.

Contents

Abstract **I**

Contents **III**

1 Introduction **1**

1.1 Overview 1

1.2 Outline 3

2 Theoretical background **7**

2.1 A beginner's guide to plasma physics 7

2.2 Drift mechanisms 10

2.2.1 General drift velocity 10

2.2.2 Drift motions 11

2.3 The Braginskii equations 13

2.3.1 Derivation 14

2.4 A short theory of turbulence 16

2.4.1 Primary and secondary instabilities 16

2.4.2 Turbulence cascades 17

3 Numerical analysis **21**

3.1 The Hasegawa-Wakatani equations 22

3.1.1 Time and length scales 22

3.1.2 The two-fluid equations 25

3.2 The reduced equations . . . 26
3.2.1 Ohm's Law . . . 26
3.2.2 The vorticity equation . . . 27
3.2.3 The electron continuity equation . . . 28
3.3 The resulting drift wave system . . . 29

4 Drift waves **31**
4.1 Basic concept . . . 32
4.1.1 Parallel and perpendicular dynamics . . . 34
4.2 Drift wave dispersion . . . 36
4.2.1 Adiabatic group and phase velocities . . . 36
4.2.2 Non-adiabatic drift waves . . . 37
4.2.3 Calculation of growth rate and stability . . . 40
4.3 Shear and instability . . . 42
4.3.1 Resonant reflections . . . 43
4.3.2 Onset of turbulence . . . 44
4.3.3 Numerical considerations . . . 45
4.4 A single dimensionless parameter . . . 47
4.4.1 Alfvénic influence . . . 48
4.4.2 Mixing length estimate . . . 49
4.4.3 Two distinct transport regimes . . . 50

5 Zonal flows **57**
5.1 Basic concept . . . 58
5.2 Drift wave self-interaction . . . 59
5.2.1 Reynolds stresses . . . 59
5.2.2 Drift wave propagation and self-focusing . . . 61
5.3 Drift wave impact on zonal flows . . . 62
5.3.1 Conditions for growth . . . 65
5.3.2 Zonal flow feedback . . . 69

5.4 Zonal flow regime . . . 69
5.4.1 Numerical parameters . . . 69
5.4.2 Regime transition . . . 71
5.4.3 A balance of gradients . . . 72

6 Bifurcations **77**
6.1 Transport bifurcation . . . 78
6.1.1 Robustness of the stationary states . . . 78
6.1.2 Parameter analysis . . . 82
6.1.3 Correlation with drift wave intensity . . . 87
6.1.4 Spectral dependencies . . . 88
6.2 Basic bifurcation mechanism . . . 88
6.2.1 Sub-structure . . . 91
6.2.2 Influence of a chemical potential? . . . 91
6.3 Radial downhill streaks . . . 93
6.3.1 Streak generation . . . 100

7 Implications **105**
7.1 Fusion devices . . . 106
7.2 Two-dimensional atmospheric zonal flows . . . 107
7.2.1 Geostrophic modes: About climate change . . . 108
7.2.2 Beyond Jupiter . . . 109

8 Conclusions **111**

A Turbulent transport measurements **121**

Bibliography **123**

Chapter 1

Introduction

A main issue diminishing energy retention of tokamak and stellarator fusion devices is a reduction of plasma confinement due to strong levels of transport, exceeding both classical and neoclassical estimates. This kind of transport is caused by microscopic turbulence, redirecting the main focus of fusion research towards finding ways of controlling the responsible instabilities. A major candidate for a suppression mechanism has been found in zonal flows, linearly stable poloidal $\vec{E} \times \vec{B}$-modes which are capable of shearing the turbulent eddies apart, thereby reducing radial transport.
The high-gradient edge of modern fusion devices serves as a source of energy for a number of such unstable modes, including drift waves, poloidally propagating magnetized plasma modes. In this region, the H-mode [1], a high-confinement transport regime crucial to the economical operation of any fusion reactor, has been discovered, leading to renewed interest in drift wave-based zonal flows.

1.1 Overview

For the first two decades after World War Two, fusion research had been conducted with much optimism. The development of the tokamak - a torus-shaped device with a toroidal magnetic field maintained by (superconducting) coils and a stabilizing, current-induced poloidal field - in the 1950s led to a severe improvement in confinement when compared to earlier pinch models or simple magnetic mirrors [2]. By the 1960s, however, the naïve hope of achieving efficient, extremely small fusion devices had to be discarded after collision-induced classical transport (and later, neoclassical transport, which includes the geometry effects of banana-shaped particle orbits and drift-based Pfirsch-Schlüter currents due to the magnetic field curvature) was found to be insufficient to account for the massive heat losses that were experienced [3]. As has been thoroughly described in many review papers [4, 5, 6, 7], turbulent transport caused by a number of instabilities - notably (collisional) drift waves [8] and ion temperature gradient modes [9] -, and their complex interactions had to be taken into account, rendering the previously applied bifurcation-free scaling laws and global diffusion coefficients inaccurate [10]. The discovery of large-scale phenomena further complicated this picture [11]. A great step forward was achieved only in 1982 when

a transport bifurcation leading to a high-confinement regime with steep density gradients at the edge, the so-called H-mode, was discovered unexpectedly [1]. Albeit still being insufficiently understood, the H-mode has by now become indispensable to the success of modern fusion devices.

Due to the high complexity of the experienced plasma features, it was soon obvious that the microscopic behavior of the plasma had to be understood [12, 13] in order to make predictions for its large-scale behavior [14], including the H-mode. Thus, the interaction of the turbulence with itself as well as the large-scale flow phenomena within the plasma had to be analyzed, especially in the high-gradient plasma edge [15, 16]. By constructing an analytical three-wave model it was discovered that the anisotropy of turbulent mode propagation velocities leads to an inverse energy cascade - as opposed to the more common Richardson cascade towards smaller scales [17] - growing towards increasingly larger scales, forming zonal[1] flows [19, 20]. These are characterized by zero poloidal and toroidal wavenumber [21] and uniform radial layers of oppositely directed bands, and are able to shear the eddies apart [22, 23, 24], thus reducing turbulent transport [25]. The zonal flow picture is complicated by the influence of geodesic curvature, in which case a parallel return flow is required to cancel out any of the divergences occurring in the poloidal flow [26]. These divergences develop due to the constant magnetic flux enforcing fluid compression when moving towards the high field side[2]. If the available fluctuation energy proves insufficient to overcome this resistance - and generally, this is the case [25] -, the absence of a parallel return flow results in an oscillatory motion: A geodesic acoustic mode is formed [27].

The underlying collisional drift wave turbulence [28, 29, 30] from which zonal flows may develop in the cool plasma edge [31, 32] - ubiquitously so in actual fusion devices [33, 34] - can be described by the Braginskii [35]-based two-fluid Hasegawa-Wakatani equations, which were first analyzed numerically in the 1980s [36, 37]. This Braginskii system is derived from a Boltzmann-based two-fluid analog to the magnetohydrodynamic moment equations, leading to a set of six equations. Discarding magnetic geometry, Hasegawa and Wakatani were able to show that the resulting drift waves interact nonlinearly with each other, exciting zonal flows through the divergence of Reynolds stresses [38]. A wave-kinetic scattering process - also applicable to atmospheric Rossby waves [39] - was proposed as the cause for zonal flow growth excitation, at least when a separation of flow and turbulence scales in both space and time is assumed [40]. Since the 1990s, numerical simulations utilizing both 3D fluid and 5D gyroorbit-averaged gyrokinetic [41, 42] approaches have been able to confirm these results [11], observing transport reduction under certain conditions of structure formation [43] with flow shearing or trapping effects [44]. Most recently, a refined wave-kinetic approach was used to derive the zonal flow steady state for collisional drift waves [45, 46], with a confirmation of the resulting energy flux modulations provided by two-fluid Braginskii studies [47, 48]. While the applicability of these results is hampered by an absence of a strict separation of scales under realistic circumstances (zonal flows, for example, exhibit eddy-sized radial wavelengths while similarly spanning the entire torus)

[1] The word zonal in zonal flows stems from their latitudinal counterparts in Earth's atmosphere [18].

[2] Under the (realistic) assumption that the magnetic pressure exceeds the thermal pressure.

and the fact that the turbulence cannot always be considered weak [49], they allude to the existence of a finite [50, 51] zonal flow onset corresponding to a certain minimum level of drift wave turbulence growth [25].
Despite all this progress, the exact drift wave zonal flow interaction mechanisms are a subject of ongoing controversy. The predator-prey model [52], which features prominently in the modern literature [11, 34], suggests a zonal flow feedback on drift waves based on the rationale that zonal flows shear apart the turbulent eddies, with the drift waves being modulationally unstable to perturbations in the shear flow [53]. However, zonal flows have been shown (in [54] and again, in this work) to retain their strength in a drift wave-poor environment as well, with drift waves actually being amplified - not weakened - by reflections at resonant surfaces and radial zonal flow maxima.
With as well as without the assumptions of extended predator-prey models, bifurcations in the turbulence intensity between strongly and weakly collisionally damped zonal flows were discovered [55, 56, 57]. These were not the only ones: Transport bifurcations of the temperature and flow gradients following heat input [58] or large-scale condensates [59] were found, while even zonal flow excitation itself may be caused by drift wave mode bifurcations [60]. Another bifurcation was provided by a radial heat flux analysis [25], yielding an increased heat flux concentration at the zonal flows in the electron diamagnetic drift direction, rendering it plausible to expect a similar effect for the density flux. Most importantly, the transition between H-mode and L-mode still remains a largely unsolved puzzle, even with flow- [61, 62] and bifurcation-based ansätze [52], turning such symmetry breakings and their necessary preliminaries into a focal point for this work - resulting in the aim to conduct an analysis of possible bifurcations within a drift wave zonal flow framework.

1.2 Outline

As has been discussed in Section 1.1, flow and transport bifurcations are a topic of paramount interest to the fusion research community. Thus, the intent of this work is to find flow-induced bifurcations within a turbulent resistive drift wave zonal flow framework utilizing self-consistent first principles numerical computations and theoretical considerations, to examine their characteristics and to analyze their possible ramifications for confinement fusion as well as fields beyond plasma physics.

The necessary theoretical basics are dealt with in Chapter 2. After a concise introduction to plasma physics, the concept of gyration-based drift motions under the influence of a magnetic field is discussed, with the main focus being put on the $\vec{E} \times \vec{B}$-drift caused by an electrostatic potential. These drifts mark the relevant perpendicular motions within the two-fluid moment equations (which are analogs to the basic magnetohydrodynamic moment equations), leading to the Braginskii equations, which are subsequently refined to describe a drift wave system proper. Finally, the chapter is rounded off by a short introduction into the concept of turbulence - from Rayleigh-Taylor-style primary instabilities to a derivation of the Richardson cascade occurring in full-blown 3D turbulence.

In Chapter 3, the numerical methods employed in this work are examined, and the decision in favor of the self-consistent nonlinear two-fluid code NLET [16] - as opposed to gyrofluid or gyrokinetic codes - is elucidated. NLET is based on the dimensionless Braginskii equations, a subset of which - the Hasegawa-Wakatani equations - are utilized in this work. Based on these equations, a set of customized time and length scales is defined, and a threshold value of a single dimensionless parameter $\hat{\rho}_s$ (defined in [63]) dividing the system into two different regimes is described. With these definitions, a detailed analysis of the three equations governing the described drift wave system, the generalized Ohm's law, the vorticity equation and the electron continuity equation is given, including a physical interpretation for all sub-terms. Finally, the fundamental drift wave equation system is derived, dependent only on the density n, the electrostatic potential ϕ and the parameter $\hat{\rho}_s$.
A detailed introduction into the appearance and linear characteristics of drift waves, poloidally drifting, fishbone-shaped modes occurring in the high density gradient edge of magnetized confinement plasmas, is provided in Chapter 4. The basic physical concept - a small density perturbation leading to a delay in ion reaction (when compared to the electron response) and thus to radial $\vec{E} \times \vec{B}$-flows, which propel the drift waves poloidally for any given radial density gradient - is examined. After a derivation of the dispersion relations, including the phase and group velocities of both adiabatic and nonadiabatic drift waves as well as the drift wave growth rate γ, the effects of magnetic shear and resonant surfaces are introduced, culminating in a discussion of drift wave stability under the specific conditions of this work. A major task thereafter lies with the identification and elimination of potential numerical instabilities and artificial pollutions. With these considerations, the claim of $\hat{\rho}_s$ being the single parameter determining the development of the drift wave equation system can finally be examined. Two associated regimes are analyzed, as well as a potential third scale based on Alfvén waves. A mixing length estimate is utilized to derive an analytical relation between these distinctly different scales for low and high $\hat{\rho}_s$, yielding convergence of the transport levels in both regimes in their respective units. The in-between threshold value of $\hat{\rho}_s$ is then compared to the onset of large-scale phenomena. Several convergence issues are identified and dealt with before these theoretical predictions are confronted with the numerical results, reaching excellent agreement.
Chapter 5 deals with the poloidal zonal flows emerging from the aforementioned drift wave turbulence. After an introduction to the fundamental concepts of zonal flows as well as their transport-reducing capabilities conveyed through eddy-shearing, the interaction between drift waves and shear flows is discussed in detail. Turbulent self-interaction of drift waves leads to Reynolds stresses, allowing the drift waves to impact the zonal flow structure. A drift wave action invariant is used to quantify the associated change in zonal flow amplitude in relation to the drift wave intensity, yielding a set of conditions necessary for drift wave-induced zonal flow growth. Conversely, drift-wave propagation patterns under the influence of a specific shear flow are derived, shedding light on an important asymmetry: While drift waves close to flows in the electron diamagnetic drift direction - dubbed positive flows - exhibit attraction towards (and, for low-energy modes, even trapping around) these flow maxima, negative flows are found to repulse the turbulence, reducing turbulent transport in their vicinity. With this improved understanding of the drift wave zonal flow interaction,

parameter studies focusing on $\hat{\rho}_s$ are undertaken, and the zonal flow regime transition - found to correlate with the transport transition - is finally realized as well as explained theoretically via a balance between a resonance gradient and the flow shear gradient.
Building on the previously established results, the main focus of Chapter 6 is put on the analysis of bifurcations within the zonal flow regime. The asymmetrical force exerted by the flows on the drift waves - and thus also their influence on the turbulent transport levels - provide the pivotal clue, leading to a prediction of corrugations on top of the background density gradient as the only way of maintaining the transport balance. Extensive numerical computations are performed to verify the robustness and the characteristics of these analytical considerations under a number of exterior influences, revealing another major transport bifurcation byproduct, an asymmetry in the zonal flow pattern. A comprehensive parameter analysis ensues, concerned with the respective energy distributions, turbulence spectra, self-similarities, bifurcation strengths, time scales necessary for achieving a steady state and the correlations with drift wave intensity as well as other drift wave parameters. This is supplemented by a subsequent comparison with the low-$\hat{\rho}_s$ flow-free regime and an analysis of the finer sub-structure of the corrugations. The observed zonal flow dependencies are then thoroughly discussed, and a detailed qualitative bifurcation mechanism as well as a quantitative ansatz are proposed and tested against the observed feature set. One apparent contradiction remains: Radial streaks, shown to consist of drift wave vortices, are observed to propagate opposite to any given flow gradient, thus apparently contradicting the paradigm of turbulence repulsion by negative flows. An extensive study of these downhill streaks, starting with a combined analytical-numerical approach concerned with the behavior of drift wave modes in k-space leads to a proposition of four ansätze capable of explaining the apparent contradiction based on amplification, acceleration, scattering and transport effects, and a viability analysis for each one of them.
Chapter 7 deals with the implications of this work for magnetic confinement devices, being especially concerned with the stalling effects and repulsion around the bifurcation-steepened negative flows. While experimental results are still scarce as of this date, one of the most worthwhile mid-term endeavors is identified: An attempt to fine-tune the experiment to reach the transitional value of $\hat{\rho}_s$ in order to achieve maximal amplitudes of flow asymmetry. However, the ramifications of such a bifurcation transcend interest in the behavior of drift-wave based zonal flows. Consequently, the ubiquitous zonal flows which influence the macroscopic behavior of many different systems besides magnetic confinement, ranging from fusion plasmas to atmospheric, submarine or even solar modes, are discussed. Some systems are more easily observable than others, the most prominent example being the characteristic brownish-white bands in Jupiter's atmosphere, fostered by strong, rotation-induced Taylor-Proudman columns [64]. The similarities between the interaction of geostrophic modes, Coriolis and pressure forces in an atmosphere and the drift waves, magnetic fields and density gradients in a plasma are highlighted, permitting speculations about the transferability of the results of this work to gas giants. The potential implications for the Jovian planets - as well as many other astrophysical systems - are examined, up to long-term predictions for two vastly different planet-wide climate scenarios. Finally, the possibility of such a climate bifurcation on Earth itself is discussed.

Chapter 2

Theoretical background

This chapter serves as a short reminder of the main concepts in plasma physics, as well as being an introduction to drift motions and, finally, the Braginskii equations on which the Hasegawa-Wakatani equations which are utilized in this work are based.

Essential plasma concepts such as the quasi-neutrality condition and its implications, the definition of an ideal plasma and the fundamental properties of major fusion devices are introduced in Section 2.1.
Drift motions caused by charged particles gyrating under the influence of a magnetic field while experiencing a force $\vec{F}$ are discussed in Section 2.2. Special focus is hereby put on the $\vec{E} \times \vec{B}$-drift, which plays a crucial role in understanding the density-gradient-driven drift waves that will be discussed in Chapter 4.
Section 2.3 concerns itself with the Braginskii equations, a set of two-fluid equations governing the motions of the ions and electrons. Their derivation from the Boltzmann equations via the continuity and force equations for both particle species is presented.
Finally, an overview over nonlinear instabilities and turbulence is provided in Section 2.4. Starting with primary and secondary instabilities, basic insight into the development of turbulence is gained, followed by a discussion of the cascades occurring in fully developed turbulence, including Kolmogorov's 5/3-law.

2.1 A beginner's guide to plasma physics

A plasma is composed of nothing but ionized gas, thus representing the most common aggregate state in nature, accounting for other 99% of the total visible matter. Its characteristics are defined by strong Coulomb interactions between the positive and negative charges - dwarfing the r^{-7}-dependent Van-der-Waals forces between neutral atoms in comparison. Also, since both positively and negatively charged species move freely parallel to $\vec{B}$, plasmas exhibit high electrical conductivity, making them strongly influenceable by electromagnetic fields.
Unsurprisingly, the most basic equations of plasma physics are the same as in electrodynamics, the Maxwell equations [65]:

$$\nabla \cdot \vec{D} = 0 \tag{2.1}$$

$$\nabla \times \vec{E} = -\dot{\vec{B}} \tag{2.2}$$

$$\nabla \cdot \vec{B} = 0 \tag{2.3}$$

$$\nabla \times \vec{H} = \vec{j} \tag{2.4}$$

where the displacement current has been omitted for non-relativistic plasmas where $\dot{\vec{D}} \ll \vec{j}$. ρ can be discarded as well, rendering the electric field retrievable via Ohm's Law

$$\vec{j} = \sigma_{el}\left(\vec{E} + \vec{v} \times \vec{B}\right) \tag{2.5}$$

This omission of ρ is valid due to the macroscopic quasi-neutrality [66] of a plasma,

$$\frac{n_e - Z_i n_i}{n_e} \ll 1 \tag{2.6}$$

Even slight deviations from this state already yield strong electric fields and thus currents aimed at repositioning the charged particles. Due to this quasi-neutrality, electric fields within the plasma are effectively cut off, decaying exponentially: Solving the Poisson equation for a test charge in a plasma, $\Delta\Phi = -\frac{\rho}{\epsilon_0} = -\frac{q\delta(r)}{\epsilon_0} + e\frac{n_e - n_i}{\epsilon_0}$, and assuming a Boltzmann distribution $n_e - n_i = n_{e,0}\left(e^{\frac{e\Phi}{kT}} - e^{-\frac{e\Phi}{kT}}\right) \approx 2n_{e,0}\frac{e\Phi}{kT}$ yields the potential

$$\Phi(r) = -\frac{e}{4\pi\epsilon_0 r} e^{-\frac{\sqrt{2}r}{\lambda_D}} \tag{2.7}$$

where λ_D marks the Debye length

$$\lambda_D = \sqrt{\frac{\epsilon_0 kT}{n_{e,0}e^2}} \tag{2.8}$$

Fusion plasmas tend to have particle densities of close to $n_e \sim 10^{20}$ m^{-3} and temperatures of approx. $T \sim 20$ keV, thus yielding $\lambda_D \sim 100\ \mu$m, guaranteeing a good approximation to quasi-neutrality for larger length scales.
Quasi-neutrality can be understood more thoroughly by comparing magnetic and electric field energies in an ideal conductor ($\sigma \to \infty$),

$$\frac{\epsilon_0 E^2}{B^2/\mu_0} = \epsilon_0\mu_0 v^2 = \frac{v^2}{c^2} \tag{2.9}$$

with $|\vec{v}|$ from (2.5).
In this case, magnetic field energy dominates, electrical components in the Maxwell stress tensor are removed and electric fields are quickly neutralized via the movement of electric charges, ensuring quasi-neutrality - magnetic fields, on the other hand, can be easily

maintained through currents in the plasma.

Quasi-neutrality fails above the electron plasma frequency, the so-called cut-off frequency up to which the faster electrons are quick enough to almost instantaneously shield dynamic deviations from quasi-neutrality, effectively preventing all electromagnetic waves from penetrating the plasma. The plasma frequency is the eigenfrequency of a harmonic oscillator with $m_e d^2x/dt^2 = -e^2 n_e x/\epsilon_0$, Langmuir waves which are caused by a displacement of the electrons against a stationary positive background, yielding close to 10^{12} Hz in typical fusion plasmas:

$$\omega_{pe} = \sqrt{\frac{n_e e^2}{m_e \epsilon_0}} \tag{2.10}$$

The ion plasma frequency frequency ω_{pi} is smaller by a factor of $\sqrt{m_i/m_e}$ and therefore irrelevant for plasma shielding.

In fusion plasmas, the number of particles N_D within a Debye sphere fulfills $N_D \gg 1$, rendering them quasi-neutral. However, fusion plasmas are not only quasi-neutral (and predominately unrelativistic since $m_e = 511$ keV is one or two orders of magnitude larger than typical fusion temperatures), but also ideal, meaning that the Coulomb interactions are weak in comparison to the particles' thermal velocities (with $n^{-1/3}$ marking the mean particle distance):

$$\frac{3kT}{2} > \frac{e^2}{4\pi\epsilon_0} n^{1/3} \tag{2.11}$$

This condition is fulfilled in all modern fusion devices.

In a tokamak, the most common fusion device, toroidally shaped with major radius R and minor radius r, such an ideal plasma is - more or less effectively - trapped within a magnetic cage. From a macroscopic perspective, the electrons and ions in such a magnetically confined plasma follow the magnetic field lines as long as they are left undisturbed by collisions.
As will be seen in the next section, a simple toroidal magnetic field (winding around the major radius) caused by magnetic field coils (winding around the minor radius) is insufficient. In order to ensure stability, a toroidal current has to be induced to build up an additional poloidal field - creating the need for pulsed operation, since a central solenoid with limited maximal induction current j_{max} is utilized.

There is an alternative concept, the stellarator, superior in that it creates an intrinsic poloidal field by intricately woven coils without the need for externally induced currents. However, it is more complex both in construction and operation and allows for less usable volume with respect to the same major radius as a tokamak device.

2.2 Drift mechanisms

Before any further explanations can be reached, the way particles move in a plasma needs to be examined. The parallel (with respect to the magnetic field lines) component of the electrons' and ions' movement is unrestricted except for magnetic mirror forces, but in the perpendicular plane, the particles are forced to gyrate in a circular motion around the magnetic field lines, leading to screw-like orbits [66].
Equating centrifugal force and Lorentz force provides the gyroradius, in scalar notation

$$|q|vB = \frac{mv^2}{r} \quad \Rightarrow \quad r_g = \frac{mv}{|q|B} \tag{2.12}$$

which turns out to be approximately $10 - 50\ \mu$m for electrons and a few mm for ions in a typical fusion device. Later in this work, a specific gyroradius for electron temperature and ion mass will be dubbed ρ_s.
On this orbit, the particles gyrate (with the direction of rotation depending on the sign of their charge) with the gyrofrequency, which is also known as the cyclotron or Larmor frequency

$$\omega_g = \frac{|q|B}{m} \tag{2.13}$$

due to (2.12) yielding $v = \frac{|q|Br}{m}$.

The concept of gyration is crucial for understanding drift motion from the particles' perspective.

2.2.1 General drift velocity

The force law

$$\vec{F} = q\left(\vec{E} + \vec{v} \times \vec{B}\right) \tag{2.14}$$

is valid for arbitrary particles with charge q and velocity $\vec{v}$, featuring prominently in Ohm's law $\vec{j} = \sigma\vec{E}_{comoving} = \sigma\left(\vec{E} + \vec{v} \times \vec{B}\right)$, being Lorentz-transformed for $\vec{v} \ll c$.
For materials with very high conductivity, even the smallest electric fields are shorted out almost immediately, leading to

$$\vec{E} + \vec{v} \times \vec{B} = 0 \tag{2.15}$$

in this limit. From a comoving perspective, electric fields with $\sigma \to \infty$ may thus only exist in the context of a drift motion, where the plasma evades a force $\vec{F} \perp \vec{B}$ by drifting away,

yielding $\vec{F}_{total} = 0$. The simplest drift is found by expanding (2.15) with $\times\vec{B}$, using the identity $(\vec{v}\times\vec{B})\times\vec{B} = (\vec{v}\cdot\vec{B})\vec{B} - B^2\vec{v} = -B^2\vec{v}_\perp$. This yields the ion and electron velocity orthogonal to the magnetic field, called the $\vec{E}\times\vec{B}$ drift velocity

$$\vec{v}_{ExB} = \frac{\vec{E}\times\vec{B}}{B^2} \tag{2.16}$$

The $\vec{E}\times\vec{B}$ drift velocity marks the most important of the particles' velocities apart from the inherent screw-like orbits - which are replaced in many treatments with gyro-orbit-averaged guiding centers - as well as marking the most basic and most important drift velocity. Basically, $\vec{E}\times\vec{B}$-induced motion plays an important role whenever electric fields are present in a plasma. Other than most drift motions, the $\vec{E}\times\vec{B}$ drift does not distinguish between electrons and ions - neither mass nor charge enter the equation.
No acceleration occurs, explaining the drift expression in accordance with e.g. the electron drift in a conductor.

The electrostatic force $\vec{F} = q\vec{E}$ may be the most basic example of a force causing drift motion, but of course it is not the only one: Any force term $\vec{F}$ which stands perpendicular to the magnetic field in the Lorentz force term can drive drifts. Accordingly, the drift velocity for an arbitrary force $\vec{F}$ with $\vec{F}\perp\vec{B}$ is

$$\vec{v}_{drift} = \frac{\vec{F}\times\vec{B}}{qB^2} \tag{2.17}$$

2.2.2 Drift motions

The most important drifts [67, 66], especially with respect to this work, are:

$\vec{E}\times\vec{B}$ drift: Caused by electric fields with $\vec{F} = q\vec{E}$, thus yielding

$$\vec{v}_{ExB} = \frac{\vec{E}\times\vec{B}}{B^2} \tag{2.18}$$

The $\vec{E}\times\vec{B}$ drift can be understood in the particle picture by observing what happens when an electron or ion moves on the gyroradius' half-circle which corresponds to an accelerating electric field. Here, the velocity v and thus the gyroradius (2.12) increases while it decreases on the half-circle opposing $\vec{E}$, leading to a net movement orthogonal to $\vec{E}$ as well as $\vec{B}$.
As mentioned, the $\vec{E}\times\vec{B}$ drift is indifferent to the mass and charge of a particle, leading to the same global motion for all particles.

Diamagnetic drift: Caused by pressure gradients of the form $\vec{F} = -\nabla p/n$, thus, according to (2.17), leading to

$$\vec{v}_{dia} = -\frac{\nabla p \times \vec{B}}{qnB^2} \tag{2.19}$$

Despite a current developing, the diamagnetic drift is merely a virtual drift, as no actual particle movement takes place. In the direction of the pressure gradient, the number of gyrating particles increases. Therefore, at any point in space, more half-circles of the prevailing up-gradient particles $\perp \left(\nabla p, \vec{B}\right)$ are present than half-circles of down-gradient particles $\perp \left(-\nabla p, \vec{B}\right)$, leading to an apparent drift motion perpendicular to ∇p as well as $\vec{B}$.
The magnetic field the current produces weakens the original magnetic field, making the plasma behave diamagnetic (as do the particles within, due to the circular gyrocurrent acting to weaken $\vec{B}$). From (2.19) follows $\vec{j} \times \vec{B} = \nabla p_\perp$, the time-independent equilibrium condition for flux surfaces - thus diamagnetic currents are able to compensate a pressure gradient perpendicular to the magnetic field.

∇B and curvature drifts: Caused by a gradient in the magnetic field with $\vec{F} = -\mu \nabla B$ where $B = |\vec{B}|$ and the magnetic moment $\mu = IA = q\frac{\omega_g}{2\pi}\pi r_g^2 = q\frac{qB}{2m}\left(\frac{mv_\perp}{qB}\right)^2 = \frac{mv_\perp^2}{2B}$, thus the ∇B drift comes out as

$$\vec{v}_{\nabla B} = -\frac{E_{kin,\perp}\left(\nabla B \times \vec{B}\right)}{qB^3} \tag{2.20}$$

Due to the curvature of the magnetic field lines, a second magnetic field gradient term exists for the parallel velocity, resulting in the so-called curvature drift

$$\vec{v}_{curv} = -\frac{2E_{kin,\parallel}\left(\nabla B \times \vec{B}\right)}{qB^3} \tag{2.21}$$

valid for $\vec{j} = 0$. Otherwise, ∇B needs to be replaced by a κ-based curvature term.
In an actual toroidal tokamak fusion device, these drifts pose a problem. Due to the q-dependency and the resulting charge separation (ions moving upwards in a counter-clockwise system) as well as the associated drift velocities exceeding 1 km/s, strong $\vec{E} \times \vec{B}$ currents are actuated, moving the plasma radially outwards in a pure toroidal magnetic field created by poloidal coils. An additional toroidal current is required to add a poloidal component to $\vec{B}$: Subsequently, the magnetic field lines wind around the toroidal axis - thereby spanning the flux surfaces - so that the upwards movement of the ions causes inward[1] movement in one half of the torus and outward movement in the other. These parts cancel each other, averaging out the drift effects.

[1] Inward and outward are always to be understood with respect to the minor radius.

Polarization drift: Caused by an electric field inhomogeneous in time, with

$$\vec{v}_{pol} = \frac{m\dot{\vec{E}}}{qB^2} \tag{2.22}$$

The polarization drift is perpendicular to a force which stems from a $\dot{\vec{E}}$-caused acceleration of the $\vec{E} \times \vec{B}$-drift - thus an acceleration parallel to this drift. Imagining a constantly increasing electric field, the gyroradii cease to be closed, leading to an additional drift component in the direction of the electric field gradient. This is different from the $\vec{E} \times \vec{B}$ drift where the only possible net drift is intrinsically orthogonal to $\vec{E}$.
The polarization drift, since it is charge-specific, such as the diamagnetic drift and the ∇B and curvature drifts, leads to charge separation, causing $\vec{E} \times \vec{B}$ drift. The current it brings about depends only on the (effective) mass. Its designation is derived from two facts: Firstly, the analogy to the polarization current in the Maxwell equations, another current density proportional to $\dot{\vec{E}}$. Secondly, the difference between $\vec{v}_{pol,i}$ and $\vec{v}_{pol,e}$ due to the different particle masses causes actual polarization.

2.3 The Braginskii equations

At this point, it is essential to introduce the equations describing the plasma dynamics within the drift wave system which is to be examined. A more complete alternative to the classic equations of magnetohydrodynamics, also stemming from the Boltzmann equation, is employed: The two-fluid equations. These render a good approximation of physical reality if the change of the magnetic and electric fields over one gyroperiod is small, requiring $\omega_g B \gg \partial_t B$ and $B \gg r_g |\nabla B|$. Then, averaging over the gyrating motion becomes possible, yielding the motion of the gyrocenter. Under these circumstances, the Braginskii equations

$$d_t n + n\nabla \cdot \vec{v} = 0 \tag{2.23}$$

$$mn d_t \vec{v} = -\nabla p - \nabla \cdot P + qn\left(\vec{E} + \vec{v} \times \vec{B}\right) + \vec{R} \tag{2.24}$$

hold true when a quasi-Maxwellian distribution is presumed to achieve hierarchy closure of the moments. These first two [68] Braginskii equations [35] resemble closely the ordinary magnetohydrodynamic equations derived from fundamental moments of the Boltzmann transport equation (where a marks the particle species, and $f_a(t, \vec{x}, \vec{v})$ marks the particle density in the 6D phase space volume element $d\vec{x}d\vec{v}$)

$$\frac{\partial f_a}{\partial t} + \frac{\partial}{\partial \vec{x}}\left(\vec{v} f_a\right) + \frac{\partial}{\partial \vec{v}}\left(\frac{\vec{F}_a}{m_a} f_a\right) = \left.\frac{\partial f}{\partial t}\right|_{collisions} \tag{2.25}$$

but are valid for both particle species separately, ions and electrons alike. The temperature equations have been omitted since the equation system analyzed in this work deals with cold ions (the limit where $T_i \ll T_e$, but not necessarily $T_i = 0$) and isothermal conditions (thus, no electron temperature fluctuations are present). Apart from the field parameters $\vec{E}$ and $\vec{B}$, all variables are species-dependent. q, p, P and $\vec{R}$ mark the charges, pressures, stresses and friction forces the ions and electrons experience, while $d_t = \partial_t + \vec{v} \cdot \nabla$ is the convective time derivative.
Both equations are easily understood. (2.23) is the well-known continuity equation, while (2.24) lists the various forces which are capable of accelerating the ions and electrons: Pressure gradients, stress tensors, Lorentz forces and resistivities.
However, both equations include extremely disparate time scales. In order to be able to simulate several hundred eddy turnover times and reach a turbulent steady state (after approximately $t = 10^{-4} - 10^{-3}$ s), the fast cyclotron time scales have to be discarded, requiring a drift-reduced version of the Braginskii equations [16].

2.3.1 Derivation

The entire two-fluid plasma dynamics can be attained by processing the Braginskii equations. While a full derivation is given in [68], a synopsis with focus on the three equations necessary for this work - Ohm's Law, the vorticity equation and the continuity equation - shall be presented here.

For an ideal gas, $p = nT$, the only term remaining in $\nabla \cdot P$ is a correction due to a finite gyroradius effect, yielding

$$\nabla \cdot P = mn\vec{v}_{dia} \cdot \nabla \vec{v} \tag{2.26}$$

where $\vec{v}_{dia}$ marks the diamagnetic drift [69] $\vec{v}_{dia} = \frac{\nabla p \times \vec{B}}{qnB^2}$ derived above. Introducing a subscript s with $s = i$ for ions and $s = e$ for electrons, the friction forces are determined by the parallel current as

$$\vec{R}_s = \frac{-q_s n_e j_\parallel \hat{\vec{B}}}{\sigma} \tag{2.27}$$

Taking (2.24) $\times \vec{B}$ turns the force equation into one containing the different drift velocities

$$\vec{v} = \frac{\vec{E} \times \vec{B}}{B^2} + \frac{\nabla p \times \vec{B}}{qnB^2} + \frac{m d_t \vec{v}}{qB^2} + \dots \tag{2.28}$$

$$= \vec{v}_{ExB} + \vec{v}_{dia} + \vec{v}_{pol} + \dots \tag{2.29}$$

where the ... denote further higher-order terms.

Solving (2.28) for $\vec{v}_{pol,i}$ iteratively (again using $\times\vec{B}$) in lowest order yields

$$\vec{v}_{pol,i} = \left(\partial_t + \vec{v}_E \cdot \nabla\right) \frac{m_i}{q_i B^3} \left(\vec{E}_\perp - \frac{\nabla_\perp p_i}{q_i n_i}\right) \tag{2.30}$$

Due to the difference in mass, the polarization drift of the electrons is negligible in comparison with the ions'. Thus, inclusion of the parallel velocity components which are accelerated or decelerated by the parallel resistivity yields

$$\vec{v}_i = \vec{v}_{ExB,i} + \vec{v}_{dia,i} + \vec{v}_{pol,i} + \vec{v}_{\|\vec{B},i} \tag{2.31}$$

$$\vec{v}_e = \vec{v}_{ExB,e} + \vec{v}_{dia,e} + \vec{v}_{\|\vec{B},e} \tag{2.32}$$

In a quasi-neutral plasma, the difference between the two continuity equations for electrons and ions, (2.23), turns out to be

$$\nabla \cdot n\vec{v}_{pol,i} + \nabla \cdot q_i n \frac{\vec{v}_{\|\vec{B},i} - \vec{v}_{\|\vec{B},e}}{\sigma_\| q_e} + \nabla \cdot n\left(\vec{v}_{dia,i} - \vec{v}_{dia,e}\right) = 0 \tag{2.33}$$

In the term for the diamagnetic drift velocity, only a sign change occurs. The polarization drift for the electrons is negligible. Finally, $q_i n \left(\vec{v}_{\|\vec{B},i} - \vec{v}_{\|\vec{B},e}\right)$ can be replaced with $\vec{j}_\|$.

The component of (2.24) parallel to the magnetic field provides an equation for $\vec{j}_\|$ (neglecting a small initial term in the electron part), the core of Ohm's law [68]

$$\frac{j_\|}{\sigma_\|} = -\nabla_\| \left(\phi - \frac{p_e}{q_i n}\right) \tag{2.34}$$

Due to the parallel nature of the equation, it is no longer necessary to write it out in vectorial form.
For small magnetic field fluctuations, $\vec{E}_\perp = -\nabla_\perp \phi$ holds true and (2.33) becomes the vorticity equation

$$\nabla \cdot n\left(\partial_t + \vec{v}_E \cdot \nabla\right) q_i B^3 \left(\nabla_\perp \phi + \frac{\nabla_\perp p_i}{q_i n_i}\right) - \nabla \cdot q_i n \frac{\vec{j}_\|}{\sigma_\| q_e} - \nabla \vec{B} \times \frac{\nabla\left(p_i + p_e\right)}{q_i B^2} = 0 \tag{2.35}$$

Here, $\vec{v}_{pol,i}$ has been replaced via (2.30) and the proper diamagnetic drift velocity has been inserted.
Now, the electron continuity equation is found by simply inserting the different velocity components into (2.24)

$$\partial_t n + \vec{v}_{ExB} \cdot \nabla n + n \nabla \cdot \left(\vec{v}_{ExB} + \vec{v}_{dia,e} + \vec{v}_{\|\vec{B}}\right) - \frac{\nabla \cdot \vec{j}_\|}{\sigma_\|} = 0 \tag{2.36}$$

2.4 A short theory of turbulence

As fusion plasmas are usually highly nonlinear, some basics in turbulence theory are required to understand the following parts of this work.
Turbulence always starts with an initial distortion within a given distribution, e.g. that of the density. It is thus imperative to determine whether this distortion leads to a growing instability or to a (damped) oscillation around the homogeneous initial state.

2.4.1 Primary and secondary instabilities

The Rayleigh-Taylor instability is one of the most common examples of a primary density instability, infamous for its often-associated formation of a vortex ring in the atmosphere: A mushroom cloud. Rayleigh-Taylor instability occurs at the boundary layer between a denser fluid (or gas) above and a lighter fluid below [70]. In a system which - in the simplest case - is governed by

$$\partial_t \rho = -\vec{v} \cdot \nabla \rho \tag{2.37}$$

$$\rho d_t \vec{v} = -\nabla p + \rho \vec{g} \tag{2.38}$$

In a plasma, density could be replaced by the pressure, while the curvature has an effect similar to gravity.
Linearization around the steady state followed by Fourier transformation yields

$$\lambda \rho_1 + \vec{v}_1 \cdot \nabla \rho_0 = 0 \tag{2.39}$$

$$\lambda \rho_0 \vec{v}_1 = -i\vec{k} p_1 + \rho_1 \vec{g} \tag{2.40}$$

where a subset 1 marks fluctuations on top of the background values which are labeled with the subset 0.
For horizontal $\vec{k} \perp \vec{g}$ with $|k| = const.$, the nontrivial pressure term vanishes. Solving the equation system yields for the eigenvalue λ:

$$\lambda = \sqrt{-\frac{\vec{g} \cdot \nabla \rho_0}{\rho_0}} \tag{2.41}$$

If the density gradient and the external force - e.g. gravity or curvature - are aligned antiparallelly with respect to each other, λ is non-imaginary and (instable) growth ensues. In a tokamak, where curvature and density gradient show this behavior on the outer low field side of the device, an ideal ballooning mode results, growing according to

$$\lambda \approx \sqrt{\frac{2\kappa \cdot \nabla p}{\rho}} = \sqrt{\frac{2\,|\nabla p|}{\rho R}} \tag{2.42}$$

Once the amplitude of the perturbation becomes sufficiently large, secondary instabilities follow. The resulting structures are far too intricate to be analyzed analytically and usually have to be tackled numerically.
The most famous example is the Kelvin-Helmholtz instability describing the formation of turbulent vortices from sinusoidal distortions (basically a secondary distortion orthogonal to the primary one) occurring at boundary layers with high relative differences in velocity - such as with the counter-rotating cloud bands in Jupiter's atmosphere, wind blowing over the surface of an ocean, or, more generally, the boundary layer of any (Rayleigh-Taylor) instability between two fluids. Including surface tension, a certain threshold velocity difference has to be surpassed for the onset of turbulence to be reached.
At the same time, these secondary instabilities - ultimately synonymous to the homogeneous chaos of full-blown turbulence as seen in Figure 2.1 - serve to restrict further growth of the primary instability.

2.4.2 Turbulence cascades

For high enough velocities, laminar flows turn turbulent. This regime is marked by high Reynolds numbers, where Re is defined as the ratio between the inertial and viscous forces (for the largest vortices), or

$$Re = \frac{\rho v L}{\mu} \tag{2.43}$$

with ρ, v, L and μ marking the density, mean velocity, characteristic length and viscosity respectively[2]. The denser, faster and less viscous a fluid is, the more turbulent it becomes.

The simplest case to analyze is that of homogeneous isotropic turbulence. Observation leads to the insight that turbulent vortices tend to successively tear each other apart into eddies of roughly half their original size, until viscosity dissipates their energy at the smallest scales. Or, as L. Richardson [17] put it:

> Big whorls have little whorls that feed on their velocity.
> And little whorls have lesser whorls and so on to viscosity.

This is known as the concept of turbulence cascades. Within the entire initial range, following the stirring of large vortices, e.g. by instabilities, at low wavenumbers k, and right up to the non-ideality-caused dissipation range at high k where $Re \approx 1$, the energy spectrum of the three-dimensional turbulent eddies fulfills an astonishingly simple relation, Kolmogorov's 5/3-law [71]

$$E(k) \propto k^{-5/3} \tag{2.44}$$

[2]Generally, the only viable parameters to be determined are mean values.

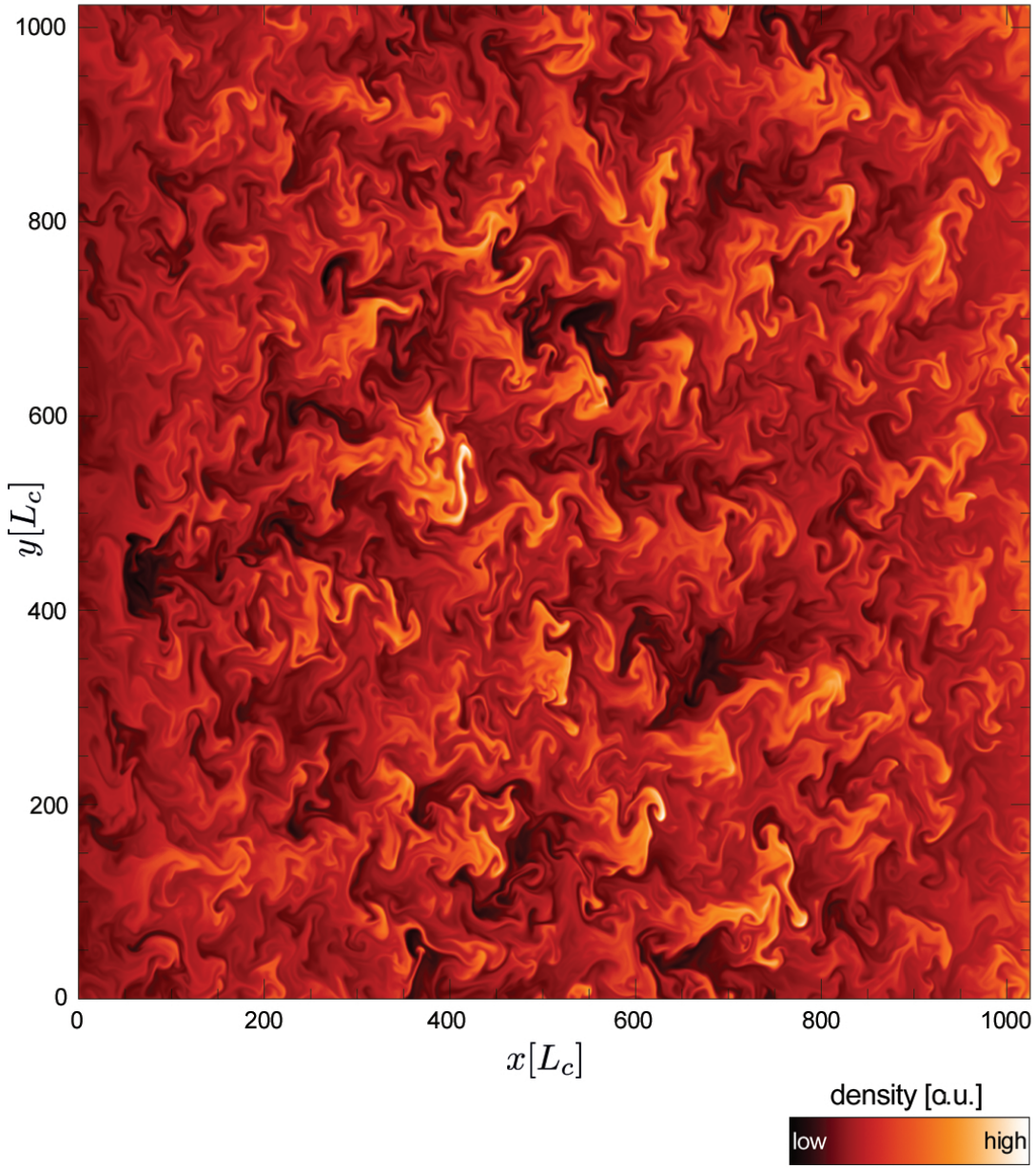

Figure 2.1: A typical density corrugation pattern of full-blown (ballooning) turbulence, drawing its energy from a density gradient (directed to the left), is plotted in the radial-poloidal x-y-plane for numerical parameters $n_{x,y} = 1024$ and $L_{x,y} = 25$ (defined in Chapter 3). Bright colors mark downhill-moving eddies of increased density, while uphill-moving negative density blobs appear darkened. As will be the case with many more graphs, the results are plotted with respect to the numerical grid span width L_c as it is defined in Subsection 3.1.1. Unless stated otherwise, only qualitative differences in the plotted variables - e.g., heightened or lowered density - will be relevant.

so that

$$Re(k) \propto \frac{v(k)}{k} \propto \frac{\sqrt{kE(k)}}{k} \propto k^{-4/3} \tag{2.45}$$

where the dissipation range coincides well with $Re(k_{dissipation}) \approx 1$.

The basic idea behind Kolmogorov's 5/3-law is that the energy flux remains constant over all k up to dissipation, since the energy does not accumulate on any level [72]. Thus,

$$const. = P(k) \tag{2.46}$$

As a rough estimate, it is assumed that vortices of $L \approx 1/k$ need approximately one revolution to hand on their energy to those with $L/2$, thus

$$\tau(k) \approx \frac{L}{v(k)} \propto \frac{1}{kv(k)} \tag{2.47}$$

where the energy in these vortices between L and $L/2$ correlates to a spherical shell spanned between k and $2k$ in k-space:

$$E(k...2k) \approx \int_{k}^{2k} E(k)dk \propto kE(k) \tag{2.48}$$

With

$$v(k) \approx \sqrt{2\frac{E(k...2k)}{\rho}} \propto \sqrt{kE(k)} \tag{2.49}$$

the energy flux can finally be determined to be

$$const. = P(k) \propto \frac{E(k...2k)}{\tau(k)} \propto \frac{kE(k)}{\frac{1}{kv(k)}} \propto k^{5/2}E(k)^{3/2} \tag{2.50}$$

yielding Kolmogorov's famous 5/3-law.

This holds true even for two-dimensional turbulence, however only for small k, and with the caveat that the energy cascade is now an inverse cascade, leading to ever larger vortices [70]. For smaller scales, a direct cascade of the equally conserved enstrophy $S = \omega^2/2$ ensues, where ω marks the vorticity. Only through separation of the energy and enstrophy cascades can both a constant energy flux and a constant enstrophy flux be upheld.

Chapter 3

Numerical analysis

Numerical computations have become an indispensable tool in theoretical fusion plasma research, due to the nonlinearities and the multitude of disparate scales involved. In this work, more than 1,000 runs have been performed, using 8-256 processors for approximately 1-100 hours each. In total, around five million CPU hours have been spent[1].
Despite these impressive numbers, common sense dictates that today's supercomputers are not yet powerful enough to describe the entire plasma for any significant time span, thus the equation system is solved only in a small section of the system. Periodic boundary conditions are implemented, allowing the results to be somewhat generalized to the entire device - albeit with some limitations, including the artificial omission of waves with wavelengths larger than the size of the boundary box and the inability to qualitatively describe different regions of the plasma in the same simulation.

Four numerical approaches are commonly employed: Magnetohydrodynamic, two-fluid, gyrofluid and gyrokinetic ansätze [73]. These systems depict increasingly more behavioral characteristics of the plasma down the line, but they also require more computational resources, as the latter two have to include the information stored in the helical particle trajectories. Two-fluid codes yield more particle-species-dependent effects than pure MHD fluid codes, while at the same time enabling large-scale long-time calculations exceeding the capabilities of gyrofluid or gyrokinetic codes. Under the conditions of this work, the loss of features - when the two-fluid approach is compared to gyrokinetic codes - is not substantial, as much of the additional physics does not apply in a sheared-slab drift wave-only system (see [48]), and since the few notable exceptions of collisionless effects such as Landau damping[2] and particle trapping are negligible in a collisional[3] approach such as the one applied here [16].
Thus, in this work, a two-fluid code named NLET [74] is being utilized. NLET is used

[1] Due to the slow asymptotic approach towards a steady state solution for certain parameter requirements, the most massive runs have peaked at more than 25,000 CPU hours each, accumulating 20 TB of raw data in the process.

[2] Generally, Landau damping plays no role in a zonal flow dominated plasma, as its effects are minimal on $n = 0$-modes with $k_{\|} = 0$.

[3] Fluid codes are by definition collisional.

on a modified, numerical set of the Braginskii equations introduced in Section 2.3, the Hasegawa-Wakatani equations: These form a sheared-slab collisional drift wave subset, discarding temperature fluctuations, magnetic geometry effects and curvature drifts.

Accordingly, this basic equation system is discussed in Section 3.1. A reformatting of the basic variables in (2.34), (2.35) and (2.36) into computational variables is performed. Three parameters are defined, α_d - signifying the drift wave velocity α_d, as will be seen in (4.4) -, ϵ_n - the ratio between the underlying density gradient and the system size - and s, describing the shearing of the magnetic fieldlines. Two different length scales (as well as time and transport scales) can be derived from these, combining to form a single dimensionless parameter (see [63]) which will be instrumental in the studies presented in Chapters 4, 5 and 6, allowing a dimensionless one-parameter form of the Braginskii equations to be derived.
A more detailed analysis and physical interpretation of all three reduced Braginskii equations is given in Section 3.2, motivating Ohm's law, the vorticity equation and the electron continuity equation in both their full and reduced form. Subsequently, the equations are combined to form the Hasegawa-Wakatani equations describing a sheared-slab collisional drift wave system.

3.1 The Hasegawa-Wakatani equations

The drift wave system examined in this work is a turbulent, non-linear one, simplified by presuming a slab (albeit sheared) resistive drift wave system based on the Hasegawa-Wakatani equations with a background density gradient, cold ions ($T_i \ll T_e$) and no parallel velocity. Three of the six main Braginskii two-fluid equations, from which the Hasegawa-Wakatani equations are derived - the heat transport equations for ions and electrons as well as the parallel velocity equation do not apply since temperature fluctuations are dismissed and since $v_\parallel = 0$ is presumed[4] - are of importance for this system: Ohm's law (2.34), the vorticity equation (2.35) and finally the electron continuity equation (2.36).
The system is examined in 3D, since even in the slab regime, and with a basically 2D turbulence inverse cascade picture as examined in this work, the magnetic field-induced asymmetry effectuates crucial characteristics (such as the anomalous transport) to require a full 3D approach [63].
Generally, in the context of this work, the radial direction denotes the direction opposite to the background gradient and the parallel direction is aligned with the magnetic field while the remaining poloidal direction stands perpendicular to both.

3.1.1 Time and length scales

In order to be able to perform numerical computations with (2.34), (2.35) and (2.36), it is necessary to replace all quantities with their dimensionless counterparts. A subscript p

[4]Without curvature, there is no compression on a poloidal revolution of the flow, and balancing by a parallel return flow becomes unnecessary, leading to $v_\parallel = 0$.

denotes physical units while from now on dimensionless units are presented subscript-free. It is important to note that all dimensionless units refer to the fluctuations on top of the flux-surface-average (denoted with a subscript 0), not the background values themselves. Bearing in mind the specific requirements of this work, all definitions are chosen as close as possible to [63, 68, 74]:

$$n \equiv n_p \lambda / n_{e,0} \tag{3.1}$$
$$\phi \equiv \phi_p c t_0 / B L_0^2 \tag{3.2}$$
$$J_\parallel \equiv j_{\parallel,p} L_z \eta_\parallel c t_0 / B L_0^2 \tag{3.3}$$
$$v_{dia,e} \equiv T_{e,0} / eBL_n \tag{3.4}$$
$$p_e = p_i = p = n \tag{3.5}$$

with the time and length scales given as

$$t_0 \equiv \sqrt{\frac{RL_n}{2}} \frac{1}{c_s} \tag{3.6}$$
$$L_0 \equiv 2\pi q \sqrt{\frac{n_{e,0} e^2 \eta_\parallel \rho_s R}{m \omega_{g,i}}} \sqrt[4]{\frac{2R}{L_n}} \tag{3.7}$$
$$L_z \equiv 2\pi q R \tag{3.8}$$
$$L_s \equiv \frac{1}{2\pi s} \tag{3.9}$$
$$\rho_s \equiv \sqrt{\frac{T_{e,0}}{m_i}} \frac{1}{\omega_{g,i}} = \sqrt{\frac{T_{e,0}}{m_i}} \frac{m}{eB} \tag{3.10}$$

where L_0 is denoted in code units as L_x and L_y respectively, and L_s is simply the shear length scale.
A radial-poloidal length scale often used in Figures such as Figure 2.1 is the numerical grid span width L_c, one unit of which simply denotes the smallest still computationally resolved distance between two points in space:

$$L_c = \frac{L_{x,y}}{n_{x,y}} L_0 \approx 1/16 - 1/8 L_0 \tag{3.11}$$

for typical resolutions $n_{x,y} \approx 128 - 512$ and domain sizes $L_{x,y} \approx 8 - 64$.

Now, the physical parameters are chosen as follows:

$$\alpha_d \equiv \frac{v_{dia,e} t_0}{L_0} \tag{3.12}$$
$$\epsilon_n \equiv \frac{2L_n}{R} \tag{3.13}$$
$$\tag{3.14}$$

thus allowing for a simpler relation for the electron-temperature ion gyroradius

$$\rho_s = \alpha_d \sqrt{\epsilon_n} \tag{3.15}$$

which is presented here in units of L_0, relying only on the two parameters α_d and ϵ_n. This marks the first orthogonal length scale.
Here, α_d marks the drift wave velocity (this will be seen in (4.4)[5]), ϵ_n is a measure of the ratio between the gradient and system sizes (leading to larger drift wave vortices for larger values of ϵ_n).
Adding magnetic shear to the drift wave velocity and the relative gradient strength, a new shear-based orthogonal length scale can be defined - in units of L_0 - as[6]

$$L_\perp = \frac{\alpha_d^{1/3}}{s^{2/3}} \tag{3.16}$$

This is the second orthogonal length scale.

Combining (3.15) and (3.16), a new dimensionless parameter $\hat{\rho}_s$ can be defined as the ratio of ρ_s and $L_\perp$ [63]

$$\hat{\rho}_s = \frac{\rho_s}{L_\perp} \tag{3.17}$$

$\hat{\rho}_s$ will subsequently prove to be crucial for this work, as $\hat{\rho}_s$ is discovered in Chapter 4 to be the single parameter determining the turbulent transport (as well as all other physical characteristics) of a sheared collisional drift wave system[7], reducing the dimension of the parameter space to one.
(3.17) expressed through α_d, ϵ_n and s, is simply

$$\hat{\rho}_s = \epsilon_n^{1/2} \left(\alpha_d s\right)^{2/3} \tag{3.18}$$

It is important to point out that all these relations have been checked through numerical tests as well - thus theory and numerics are in agreement.

Two length scales imply two time scales as well. Thus, time in units of t_0 is normalized to

[5] (4.4) in the units used here equals $\omega = \alpha_d k_y$, thus leading to $\vec{v}_{ph} = \omega/k = \alpha_d \hat{y}$.

[6] Using the Braginskii [35] definition $L_\perp = \left(\frac{\pi q R}{s}\right)^{2/3} \left(\frac{n_0 \eta_\parallel T_e}{2e\sqrt{m_i} L_n}\right)^{1/3} \frac{m_e}{m_i B}$, this form of $L_\perp$ can be expanded to yield $L_\perp = \sqrt{\frac{R}{L_n}} \frac{2m_e\sqrt{T_e}}{B m_i} \left(\frac{R L_n}{2 T_{e,0} m_i}\right)^{1/6} \left(\frac{n_0 \eta_\parallel}{2e}\right)^{1/3} = \sqrt{R} L_n \rho_s^{2/3} \left(\frac{2\pi q}{s}\right)^{2/3} \left(\frac{\sqrt{2} c_s t_0 n_0 e^2 \eta_\parallel}{m_i \omega_{ci}}\right)^{1/3}$ and thus the desired $L_\perp = \left(\frac{\rho_s c_s t_0}{L_\nabla}\right)^{1/3} \left(\frac{L_0}{s}\right)^{2/3} = \left(\alpha L_0\right)^{1/3} \left(\frac{L_0}{s}\right)^{2/3}$.

[7] The only exceptions stemming from minor domain size-determined quantization effects and the radial positioning of resonant surfaces [16].

$$t_{L_\perp} = \frac{L_\perp}{v_{dia,e}} = \frac{1}{s^{2/3}\alpha_d^{2/3}} \tag{3.19}$$

$$t_{\rho_s} = \frac{\rho_s}{v_{dia,e}} = \epsilon_n^{1/2} \tag{3.20}$$

causing the transport units to become

$$D_{L_\perp} = \frac{L_\perp^2}{t_{L_\perp}} = \left(\frac{\alpha_d^{2/3}}{s^{4/3}}\right)\frac{L_0}{t_{L_\perp}} \tag{3.21}$$

$$D_{\rho_s} = \frac{\rho_s^2}{t_{\rho_s}} = \left(\alpha_d^2\epsilon_n\right)\frac{L_0}{t_{\rho_s}} \tag{3.22}$$

yielding the respective translations from L_0, t_0 and D_0[8].

3.1.2 The two-fluid equations

Now, (2.34), (2.35) and (2.36) can be transformed into dimensionless equations, while discarding all curvature-dependent $\nabla\cdot\vec{v}$ terms (this applies to the diamagnetic drift velocity terms in the vorticity equation and $n\nabla\cdot(\vec{v}_{ExB}+\vec{v}_{dia,e})$ in the continuity equation) as well as the parallel velocity term $n\nabla\cdot v_{\parallel\vec{B}}$ in the continuity equation:

Ohm's Law without curvature, parallel velocity or hot ion terms becomes

$$-\nabla_\parallel\left(\phi-\alpha_d n\right) = J_\parallel \tag{3.23}$$

instead of $\frac{j_\parallel}{\sigma_\parallel} = -\nabla_\parallel\left(\phi-\frac{p_e}{en}\right)$.

The vorticity equation turns into

$$\nabla_\perp\cdot d_t\nabla_\perp\phi = \nabla_\parallel J_\parallel \tag{3.24}$$

replacing $\nabla\cdot n\left(\partial_t+\vec{v}_E\cdot\nabla\right)q_iB^3\left(\nabla_\perp\phi+\frac{\nabla_\perp p_i}{q_in_i}\right)-\nabla\vec{B}\times\frac{\nabla(p_i+p_e)}{q_iB^2} = \nabla\cdot q_in\frac{\vec{j}_\parallel}{\sigma_\parallel q_e}$.

And the continuity equation now reads as

$$d_tn+\partial_y\phi-\alpha_d\epsilon_n\nabla_\parallel J_\parallel = 0 \tag{3.25}$$

standing in for $\partial_tn+\vec{v}_{ExB}\cdot\nabla n+n\nabla\cdot\left(\vec{v}_{ExB}+\vec{v}_{dia,e}+\vec{v}_{\parallel\vec{B}}\right)-\frac{\nabla\cdot\vec{j}_\parallel}{\sigma_\parallel} = 0$.

It is important to note that these equations are invariant under all sign inversion transformations of x and z as well as n and ϕ - with the notable exception of y.

[8] E.g., $t_{\rho_s} = \epsilon_n t_0$ can be used to find t in units of ρ_s, or $\rho_s = \alpha_d\sqrt{\epsilon_n}(L_{x,y}/n_{x,y})n_0$ for the direct transformation between the new length scales and the code units.

3.2 The reduced equations

Although the three main equations have now almost been simplified to the form utilized in this work, it may be helpful to compare with the full equations [35] in a curved system with hot ions and parallel velocity terms. Thus, a more detailed analysis as well as physical interpretation of (3.23), (3.24) and (3.25) will be performed to reach additional insights into their implications.

3.2.1 Ohm's Law

Within the computational Braginskii equations, Ohm's Law, or the law of electromotive force, has the following form:

$$(2\pi)^2\alpha_m\left[\underbrace{\frac{\partial\Psi}{\partial t}}_{(1)}+\underbrace{\alpha_d\frac{\partial\Psi}{\partial y}\left(\frac{L_\nabla}{L_{p_e}}+0.71\frac{L_\nabla}{L_{T_e}}\right)}_{(2)}\right]-\underbrace{\mu\frac{\partial dJ}{\partial dt}}_{(3)}-\underbrace{\nabla_\parallel h}_{(4)}=\underbrace{J_\parallel}_{(5)} \tag{3.26}$$

where α_m marks the Alfvén alpha parameter of waves caused by ion inertia and magnetic field tension. As before, all variables denote fluctuations, not mean values.
A current (5) can be influenced by a number of drives where (1) marks magnetic field fluctuations caused by fluctuations in the magnetic flux Ψ and (2) takes into consideration spatial deflections of magnetic field lines leading to a change in either electron pressure or temperature - or both.
Either Ψ-term depends on weak magnetic pressure, meaning the beta parameter

$$\beta = p/p_{mag} = nkT/(B^2/2\mu_0) \tag{3.27}$$

the ratio between thermal and magnetic pressure within the plasma, must fulfill $\beta \gg 0$. Since $\alpha_m \propto \beta q^2$ (where q marks the safety factor), strong magnetic pressure implies rigid field lines and thus that the terms (1) and (2) can be omitted (preventing the emergence of Alfvén waves, which cannot exist without field line fluctuations). For most drift waves regimes - including the system analyzed in this thesis - rigid field lines ($p_{mag} \gg p$) can be presumed, so that only the terms (3), (4) and (5) remain.
Furthermore, the electrons are defined to possess no inertia ($m_e \to 0$), a good approximation for the relevant drift wave time scales. Thus, with $\mu \propto m_e/m_i \to 0$ term (3) vanishes and only $-\nabla_\parallel h = J_\parallel$ remains. There, $h = \phi - \alpha_d p_e = \phi - \alpha_d n_e$ (the latter being valid only in the absence of temperature fluctuations) describes the nonadiabaticity of the electrons - which is nothing but the deviation from a Boltzmann distribution $e^{-(v_{th}^2+q\phi)/T}$.

In total this yields the same result as in (3.24):

$$-\nabla_\parallel\left(\phi - \alpha_d n_e\right) = J_\parallel \tag{3.28}$$

Since $J_\parallel = \nabla_\perp \Psi$ marks the resistivity responsible for diffusion of the current density $J_\parallel$, $-\nabla_\parallel h = J_\parallel$ implies that the magnetic flux diffuses orthogonally, and proportionally to the parallel derivative of the nonadiabaticity. In the adiabatic approximation, however, the ions react instantaneously - now behaving exactly like the electrons -, preventing any fluctuation currents from developing between the two differently charged particles.
It should be noted here that it is generally considered to be more favorable to argue via currents (where only divergent currents are of relevance) since these are easier to calculate while force balances cannot be applied in many cases since their only function is to hold the plasma in place. Also, it is not the forces but the velocities which are of primary interest - and these can much more easily be gained through the time development of the potential, and thus the currents.

3.2.2 The vorticity equation

The full vorticity equation governs charge neutrality, describing the difference between the continuity equations of ions and electrons. It takes the following form:

$$\underbrace{\nabla_\perp \cdot \frac{d}{dt} \nabla_\perp \left(\phi + \tau \alpha_d p_i\right)}_{(1)} + \underbrace{\hat{C}\left(p + G\right)}_{(2)} - \underbrace{\nabla_\parallel J_\parallel}_{(3)} = 0 \tag{3.29}$$

The curvature term in (2) can be discarded in a slab system. Term (1), which contains the divergences of the polarization and diamagnetic drift currents, can be motivated by a glance at the divergence of the respective current. In case of the polarization drift (the motivation for the diamagnetic drift follows accordingly, but it can be discarded here since cold ions imply $\tau = T_i/T_e = 0$):

$$\begin{aligned} \nabla \cdot \vec{j} = \nabla \left(n q v_{pol,drift}\right) = -\nabla \left(n q \frac{m}{q} (\frac{d}{dt} \vec{v}_{ExB}) \times \frac{\hat{b}}{B} \right) = \frac{nm}{B^2} \left(\nabla \times \frac{d}{dt} \vec{v}_{ExB} \right) \cdot \hat{b} \\ = -\frac{nm}{B} \left(\nabla \times \frac{d}{dt} \left(\frac{\hat{b}}{B} \times \nabla \phi \right) \right) \cdot \hat{b} = -\frac{nm}{B^2} \nabla_\perp \cdot \frac{d}{dt} \nabla_\perp \phi \end{aligned} \tag{3.30}$$

Since this work concerns itself with slab drift wave systems instead of a toroidal or otherwisely curved geometry, the curvature term (2) containing $\hat{C} \equiv B(\vec{\nabla} \times \vec{b}/B) \cdot \vec{\nabla}$ can be removed. Due to

$$\begin{aligned} \nabla_\perp \cdot d/dt \nabla_\perp \phi = \nabla_\perp \cdot \left(\partial_t + \vec{v}_E \cdot \nabla\right) \nabla_\perp \phi = \nabla_\perp \cdot \left(\partial_t \nabla_\perp \phi + \{\phi, \nabla_\perp \phi\}\right) \\ = \nabla_\perp \cdot \left(\partial_t \nabla_\perp \phi + \partial_x \phi \cdot \partial_y \nabla_\perp \phi - \partial_y \phi \cdot \partial_x \nabla_\perp \phi\right) = d/dt \nabla_\perp^2 \phi \end{aligned} \tag{3.31}$$

the resulting equation agrees with (3.24):

$$d_t \Delta_\perp \phi = \nabla_\parallel J_\parallel \tag{3.32}$$

Physically, the time derivative of the orthogonal potential diffusion compensates for a parallel change in current.

Combining the results from Ohm's law (3.28) and the vorticity equation (3.32) yields

$$d_t \Delta_\perp \phi = -\partial_\parallel^2 (\phi - \alpha_d n) \tag{3.33}$$

This is the first of two very basic relations between plasma density and potential. Here, the right hand side term can be identified as the parallel diffusion of the nonadiabaticity (defined by the difference in behavior between n and ϕ - only in ideal adiabaticity can the potential immediately follow the density) leading to a direct link between the parallel diffusion of the nonadiabaticity and the time derivative of the perpendicular diffusion of the potential.
Accordingly, no change in the perpendicular movement can occur in a completely adiabatic system.

3.2.3 The electron continuity equation

Of special importance to the collision-dominated tokamak edge, the full electron continuity equation contains several additional terms next to the simple $\partial\rho/\partial t + \nabla \cdot \vec{j} = 0$ relation:

$$\underbrace{\frac{dn}{dt}}_{(1)} + \underbrace{\frac{L_\nabla}{L_n}\frac{\partial \phi}{\partial y}}_{(2)} - \left[\underbrace{\epsilon_n \hat{C}\left(\phi - \alpha_d p_e\right)}_{(3)} - \underbrace{\epsilon_v \nabla_\parallel v_\parallel}_{(4)} + \underbrace{\alpha_d \epsilon_n \left(1+\tau\right) \nabla_\parallel J_\parallel}_{(5)} \right] = 0 \tag{3.34}$$

where the characteristic gradient length scales $L_{system} = L_\nabla$ and L_n, denoting the scale on which a $1/e$-decrease in the density gradient occurs, are introduced. Usually, $L_\nabla / L_n \equiv 1$ is chosen.
Term (1) marks the convective derivative of the particle density $\partial n/\partial t + (\vec{v}\cdot\nabla)n$. While the curvature term (3) is easily removed, term (2) cannot be discarded so easily. It contains the crucial toroidal derivative of the potential (which actually consists mostly of the poloidal derivative, due to the usage of a parallelly compressed coordinate system to account for the differences in propagation velocities). However, replacing the fluctuation density n with the total density $n_{tot} = n + n_0(1-x)$ deletes term (2) entirely, as can be seen by

$$\begin{aligned}(\vec{v}\cdot\nabla) n_{tot} &= \phi, n_{tot} = \partial_x \phi \partial_y n_{tot} - \partial_x n_{tot} \partial_y \phi \\ &= (\vec{v}\cdot\nabla) n - (-n_0 \partial_y \phi) = (\vec{v}\cdot\nabla) n + n_0 \partial_y \phi\end{aligned} \tag{3.35}$$

In the absence of a parallel electron velocity, term (4) vanishes as well.
For cold ions ($\tau = 0$), all that is left is $d_t n - \alpha_d \epsilon_n \nabla_\parallel J_\parallel = 0$, or, in combination with (3.28)

$$d_t n + \alpha_d \epsilon_n \partial_\parallel^2 (\phi - \alpha_d n) = 0 \tag{3.36}$$

obtaining (3.25). Physically, the convective time derivative of the total density can thus be associated with the parallel diffusion of the nonadiabaticity.

3.3 The resulting drift wave system

In total, (3.28), (3.32) and (3.36) can be combined to yield the simple linearized Hasegawa-Wakatani equation system, expressed through the single dimensionless parameter $\hat{\rho}_s$:

$$\partial_t \Delta_\perp \phi + \partial_\parallel^2 (\phi - n) = 0 \tag{3.37}$$

$$\partial_t n + \partial_y \phi = \hat{\rho}_s^2 \partial_t \Delta_\perp \phi \tag{3.38}$$

where $\partial_\parallel = \partial_z - 2\pi x \partial_y$ and $\Delta_\perp = \frac{\partial^2}{\partial x^2} + \frac{\partial^2}{\partial y^2}$, describing a 3D sheared-slab collisional drift wave system.

This equation system is simple enough to be analyzed analytically as well as numerically, while retaining sufficiently complexity to exhibit the nonlinear drift wave instability crucial to zonal flow formation.

Chapter 4

Drift waves

Drift waves are poloidally propagating wave phenomena in magnetized plasmas, feeding on density gradients through density convection by $\vec{E} \times \vec{B}$-drifts.
As a small initial perturbation of the particle density results in charge separation - presuming nonadiabaticity, which causes the electrons to adapt much faster to the changes in the electric potential than the ions - an electrostatic potential develops, leading to $\vec{E} \times \vec{B}$-flows in the radial direction (directed inwards on one side of the perturbation and outwards on the other, as visualized in Figure 4.1). For a background density which decreases radially outwards, this distortion manifests itself as an apparent increase of density at the location of outward movement and a decrease where the $\vec{E} \times \vec{B}$-flows are directed inwards, resulting in a propagation of the density pattern in the poloidal direction: A drift wave develops.

Due to its analytical and numerical accessibility, the drift wave is *the* paradigmatic microturbulent mode in a magnetized plasma: While there are numerous curvature driven instabilities which dominate the majority of the volume in devices with realistic geometries, for a sheared-slab system without a temperature gradient no ITG[1] modes and curvature driven modes can develop - making this the unchallenged domain of the drift wave.
Of all naturally occurring regimes, the high-gradient plasma edge in a tokamak or stellarator is the most common domain of the drift wave. Generally, a non-turbulent drift wave can always be recognized due to its distinctive[2] fishbone-like shape which stems from a group velocity aligned parallelly to the phase velocity in the poloidal direction, and antiparallelly in the radial direction.

In Section 4.1, the development of drift waves is examined in detail, with an explanation of both the parallel and the perpendicular dynamics.
Section 4.2 starts with the simpler subset of adiabatic drift waves, where there is no differ-

[1] ITG modes are driven by an additional ion temperature gradient (which behaves roughly the same as the density gradient) and caused by parallel sound waves which in turn are created by drift waves [75] - however, both the ion temperature equation and the $v_{\parallel}$-equation are turned off in this work, thus preventing ITG modes from developing.

[2] Confusion with ballooning modes [76] can be avoided by noting that there are no wandering droplets in a turbulent, drift-wave dominated plasma.

ence in adaptation speed between ions and electrons, leading to a concurrent development of both the potential and the density. The group and phase velocities of adiabatic drift waves are derived, leading to a quantitative derivation of the trademark fishbone shape. The full equation system of nonadiabatic collisional drift waves is then discussed, including a calculation of the more complicated $\hat{\rho}_s$-based nonadiabatic drift wave dispersion relation and the resulting group and phase velocities, now also exhibiting a term in the toroidal direction. Finally, the drift wave growth rate is determined, culminating in a detailed analysis of drift wave instability in units of $\hat{\rho}_s$.

Shear has a significant influence on the development of drift waves, since it determines the locations of resonant surfaces which reflect drift waves, amplifying them in the process. This effect is examined in Section 4.3 for different wavenumbers, including its consequences for drift wave scattering. Subsequently, the requirements for drift waves to turn nonlinear are outlined. Particular emphasis is put on several numerical issues which have occurred in the course of this work: Hyperviscosities, border and domain effects and distortions caused by the Nyquist and Alfvén frequencies, among others.

Finally, Section 4.4 deals with $\hat{\rho}_s$, the single dimensionless parameter determining the complete behavior of the drift wave system. $\hat{\rho}_s$ is found to depict the ratio between two length scales (which will prove essential in Chapter 6) - one of them dominant for small values of $\hat{\rho}_s$, the other for larger ones. The theoretical predictions for their relationship based on a mixing length estimate are verified to an excellent degree by numerical studies, including very good agreement with density flux scans, leading to one transport plateau for each length scale and a transitional threshold in between, which is found to correspond very well with the zonal flow transition examined in Section 5.4.

Further drift-wave related analyses - including a discussion of the associated spectra - have been transferred to Chapter 6 due to their immediate implications for a number of crucial zonal flow characteristics.

4.1 Basic concept

Drift wave development[3] in a magnetized plasma requires some degree of non-adiabaticity to achieve charge separation, a density gradient (synonymous to a pressure gradient for isothermal plasmas) as an effective energy source and the existence of an $\vec{E} \times \vec{B}$-drift. As with all waves or instabilities, an initial distortion of a background field is required as a starting point. In the case of drift waves, this field is the scalar background density n_0. Now, a small distortion n of the density is presumed - a local change in density around the radial-poloidal-toroidal point of origin (x_0, y_0, z_0), f.e. in the shape of a steep Gauss curve.

Certain anisotropic ansätze would not be viable for drift wave generation, for example solely radial potential. In that case, no radial $\vec{E} \times \vec{B}$ drift and thus no movement orthogonal to the density gradient is possible, preventing the extraction of free energy. Thus, this derivation assumes at least some electric potential perpendicular to the radial direction is present.

[3] A more detailed discussion than in Section 4.1 is given in many literature reviews, e.g. in [30].

For the sake of simplicity, the magnetic field is assumed to be homogeneous, while both ion temperature and parallel velocity are negligible in this system.

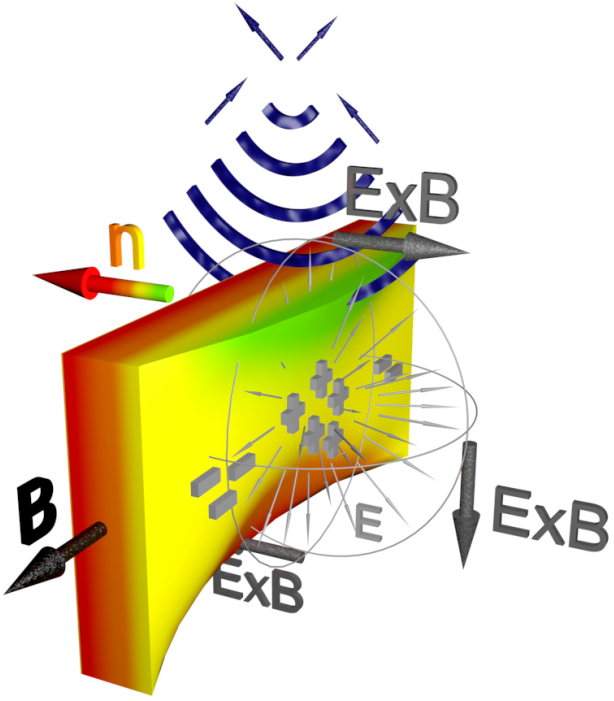

Figure 4.1: Drift wave development requires an initial density distortion. Under non-adiabatic conditions, the electrons (marked by grey minuses) outpace the ions (marked by grey pluses), especially in the direction of the magnetic field $\vec{B}$, leading to charge separation and a spherical electric field $\vec{E}$, which yields circular $\vec{E} \times \vec{B}$-drift vortices around $\vec{B}$. On the axis perpendicular to the density gradient (where red marks high density, and green marks low density) as well as the magnetic field, the $\vec{E} \times \vec{B}$-drift moves the density distortion into areas with higher density (at the top) and lower density (at the bottom) respectively, feeding on the gradient and subsequently leading to a relative increase and reduction of density - an effect which is visualized by the green bulge at the top and the reddish neck below. The distortion thus appears slightly shifted perpendicular to ∇n and $\vec{B}$, as indicated by the dark blue rings: A drift wave propagating with the diamagnetic drift velocity - hence the name - in the poloidal direction ensues. Here, the lower set of blue arrows mark the drift wave phase velocity $\vec{v}_{ph}$, while the upper arrows indicate the drift wave group velocity $\vec{v}_{gr}$. During the entire process, quasi-neutrality is guaranteed by the perpendicular ion polarization drift while the parallel electron dynamics couple the fluctuating n and ϕ together to ensure the structural integrity of the drift wave.

4.1.1 Parallel and perpendicular dynamics

The simpler part of the analysis concerns itself with the dynamics parallel to the magnetic field, where the magnetic field implies no restrictions on particle movement.
In the case of a positive distortion, the smaller inertia of the electrons ($m_e/m_i < 1800$ for all ions) allows them to react more quickly to the change in density than the ions are capable of, making them accelerate away from the initial fluctuation much faster - until the initial force on the electrons is canceled by the rising electrostatic potential between the two separately charged particles. The ensuing electron oscillation occurs at the plasma frequency of the electrons, reaching the GHz range in a typical tokamak's edge.
However, a number of complications arise through the coupling of the dynamics parallel to the magnetic field to the perpendicular dynamics [77].

An electrostatic potential is not only created by a parallel charge separation, but also by an inertia-induced charge separation orthogonal to the magnetic field. This potential grows until it balances the density fluctuation, nullifying the effective force exerted on the electrons. The electric field yields a $\vec{E} \times \vec{B}$-drift in a direction orthogonal to both the magnetic field (assumed to be aligned in the toroidal direction) and $\vec{E}(x, y, z)$, and thus - in a right-handed coordinate system - a clockwise drift around the center of the fluctuation. According to the derivation of the $\vec{E} \times \vec{B}$-drift in Section 2.2, this holds true for particles of any mass, charge or velocity.
Quasi-neutrality is upheld: Considering slow changes to the electric field - slow in comparison with the ion and electron gyro frequencies -, there is a small correction to this picture due to the polarization drift. Since the ions move in circles around the distortion maximum while the electric field changes at the same time, they start to spiral outwards for increasing field amplitudes and inwards for decreasing field amplitudes. Due to higher ion inertia, the effect on electrons is much smaller in comparison. Therefore, this polarization drift effect is able to compensate for all changes in the electric field caused by the parallel dynamics, shorting them out and keeping the system quasi-neutral: The divergence of the perpendicular current (to which the polarization drift amounts) matches that of the parallel current.
The last ingredient in this picture - crucial for drift wave growth and propagation - is a density gradient orthogonal to the magnetic field lines, aligned in the negative radial direction. This ensures self-sustainability of the drift wave turbulence [78]. Since the aforementioned balance between the parallel and perpendicular dynamics implies plasma transport in the radial direction, with the sign depending on the local sign of ϕ', this plasma transport correlates to movement into outer regions of decreased density for $y > y_0$ and, vice versa, into more inward-lying regions of increased density for $y < y_0$. This movement correlates with a perceived increase (or decrease) of density relative to the new surroundings, and thus an actual increase (or decrease) of the initial positive distortion for $y > y_0$ (or $y < y_0$): The distortion appears to shift slightly in the positive poloidal direction. Since the process repeats itself over and over again, the entire structure thus propagates in the positive poloidal direction.

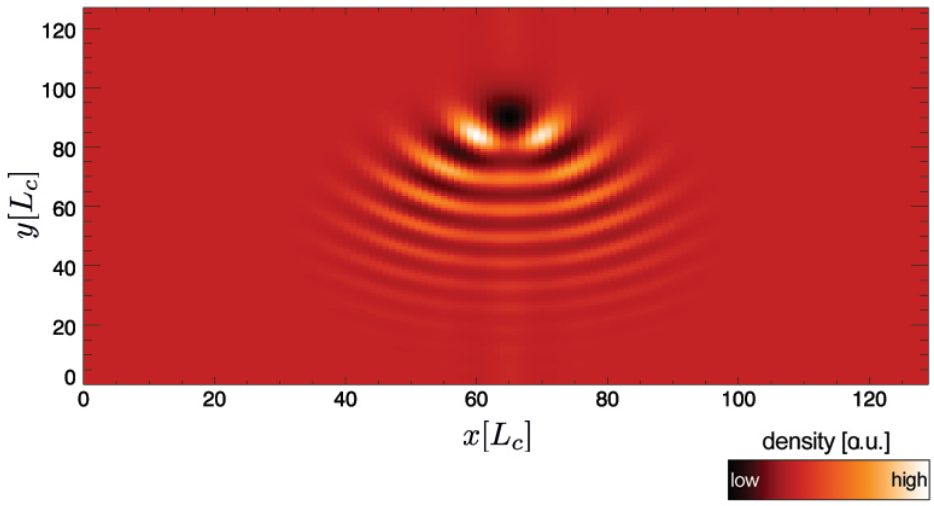

Figure 4.2: The fishbone shape of a simple linear shearless adiabatic drift wave system at an early time t is shown here in the radial-poloidal density picture. As is required for adiabaticity, the potential behaves in exactly the same way as the density.

Another way to understand this perceived increase and decrease of density is to look at the effect a density gradient has on a localized $\vec{E} \times \vec{B}$ vortex which necessarily surrounds every local maximum or minimum in potential. More fluid is pulled down the density gradient than up, leading to a positive density fluctuation on the down-gradient half-circle of the $\vec{E} \times \vec{B}$ vortex where $\vec{v}_E$ and ∇n are antiparallel and vice versa a decreased density on the other half - the density fluctuation is thus phase-shifted (by $\pi/2$ for sinusoidal oscillations, as will be seen in (4.25)) in comparison with the electrostatic potential. The exact phase relation between the density and potential perturbations is essential in determining growth or damping of a drift wave, with a shift of $\pi/2$ between the two being the most unstable case if n leads ϕ, while becoming the most stable for ϕ leading n.

For adiabatic drift waves, density and potential coincide and no phase shift occurs, leading to zero growth or damping (in the case of infinite conductivity). For nonadiabatic drift waves, the electron response to any density perturbation is not immediate any more. The resulting phase shift between n and ϕ causes the density perturbation to be further ahead, phase shifted so that its maximum comes close to the point where the main part of the $\vec{E} \times \vec{B}$-vortex crosses the line of propagation orthogonal to $\vec{B}$ and ∇n: The maximum of the $\vec{E} \times \vec{B}$ particle flux divergence. Maximal drift wave growth ensues.

It is not unlimited, however. As will be shown in Chapter 5, the zonal flows fed by the drift waves themselves shear them apart into ever smaller eddies [30]. Over time, this forced turbulence cascade leads the drift wave turbulence to such small wavenumbers that growth is inhibited by damping effects, or the eddies are dissolved by dissipation. But even without zonal flows, a certain stationary level of nonlinear saturation cannot be exceeded.

4.2 Drift wave dispersion

In order to understand drift waves in more detail, it can be helpful to look at a simplified system of shearless ($\partial_\parallel = \partial_z$) and adiabatic ($\omega k_\perp^2 \ll k_\parallel^2$) drift waves[4]. After a Fourier transformation of (3.37) and (3.38), only

$$\phi = n \tag{4.1}$$

$$-i\omega n + ik_y\phi = i\hat{\rho}_s^2\omega k_\perp^2\phi \tag{4.2}$$

remains, where $k_\perp = \sqrt{k_x^2 + k_y^2}$. Thus, the drift wave frequency is derived as

$$\omega = \frac{k_y}{1 + \hat{\rho}_s^2 k_\perp^2} \tag{4.3}$$

with the dominant term for small $k_\perp$ being

$$\omega = k_y \tag{4.4}$$

leading to a drift in the electron diamagnetic drift direction (perpendicular to both the magnetic field and the density gradient) with $\vec{v}_{dia,physical} = \alpha_{d,numerical}$.

4.2.1 Adiabatic group and phase velocities

Now it is a straightforward exercise to calculate the adiabatic group and phase velocities in these units (including dispersion in the radial direction due to the Laplacian in (4.2)):

$$v_{gr,x} = \frac{\partial\omega}{\partial k_x} = \frac{-2k_x k_y\hat{\rho}_s^2}{\left[1 + \hat{\rho}_s^2(k_x^2 + k_y^2)\right]^2}\,(+hot) \tag{4.5}$$

$$v_{gr,y} = \frac{\partial\omega}{\partial k_y} = \frac{1}{1 + \hat{\rho}_s^2(k_x^2 + k_y^2)} - \frac{2k_y^2\hat{\rho}_s^2}{\left[1 + \hat{\rho}_s^2(k_x^2 + k_y^2)\right]^2}\,(+hot) \tag{4.6}$$

$$v_{ph,x} = \frac{\omega k_x}{k^2} = \frac{k_x k_y}{\left[1 + \hat{\rho}_s^2(k_x^2 + k_y^2)\right](k_x^2 + k_y^2)} \tag{4.7}$$

$$v_{ph,y} = \frac{\omega k_y}{k^2} = \frac{k_y^2}{\left[1 + \hat{\rho}_s^2(k_x^2 + k_y^2)\right](k_x^2 + k_y^2)} \tag{4.8}$$

Generally, $v_{gr,x} > 0$ corresponds with $k_x < 0$ and vice versa. No z-dependency remains.

[4] Shearlessness follows directly from perfect adiabaticity $\omega k_\perp^2 = 0$ since the remaining $\partial_\parallel$-term is thereby rendered irrelevant.

In the linear regime, drift waves are marked by their recognizable fishbone shape (see Figure 4.2), developing since thermal expansion of the initial blob which is moving in the negative poloidal direction leads to a separation of modes depending on their $Im(\omega)$.
For a real density distortion, the complex conjugate is required to eliminate the imaginary part - accordingly, both positive and negative wavenumbers k must exist. Thus, $k_x > 0$ must be true on one side (the one in the positive radial direction), corresponding with $v_{gr,x} < 0$, and $k_x < 0$ on the other, corresponding with $v_{gr,x} > 0$, as confirmed by the group and phase velocities in (4.5)-(4.8). It is also clarified that $\vec{v}_{gr,x} \uparrow\downarrow \vec{v}_{ph,x}$ as well as $\vec{v}_{gr,y} \Uparrow \vec{v}_{ph,y}$. Recalling that the group velocity points in the direction of movement of the wave packet while the phase velocity stands orthogonal on the wavefronts, the fishbone shape can be pieced together[5].

4.2.2 Non-adiabatic drift waves

Now, the full equation system from (3.37) and (3.38) shall be analyzed:

$$\partial_t \Delta_\perp \phi + \partial_\parallel^2 (\phi - n) = 0 \tag{4.9}$$

$$\partial_t n + \partial_y \phi = \hat{\rho}_s^2 \partial_t \Delta_\perp \phi \tag{4.10}$$

A Fourier transformation yields

$$i\omega k_\perp^2 \phi - k_\parallel^2 (\phi - n) = 0 \tag{4.11}$$

$$-i\omega n + ik_y \phi = i\omega k_\perp^2 \hat{\rho}_s^2 \phi \tag{4.12}$$

With $\phi = \omega n / \left(k_y - \hat{\rho}_s^2 k_\perp^2\right)$ this translates into

$$\omega_{1,2} = \left(\hat{\rho}_s^2 k_\parallel^2 k_\perp^2 + k_\parallel^2 \pm \sqrt{k_\parallel^4 \left(1 + \hat{\rho}_s^2 k_\perp^2\right)^2 - 4ik_y k_\parallel^2 k_\perp^2} \right) / \left(2ik_\perp^2\right) \tag{4.13}$$

or, after simplification and omission of the wrong, shrinking solution

$$\omega = \frac{2k_y}{\left(1 + \hat{\rho}_s^2 k_\perp^2\right)} \left[1 + \sqrt{1 - \frac{4ik_\perp^2 k_y}{\left(1 + \hat{\rho}_s^2 k_\perp^2\right)^2 k_\parallel^2}} \right]^{-1} \tag{4.14}$$

For $k_\parallel \to \infty$ this falls back to the well-known adiabatic relation.

$$\omega = \frac{k_y}{1 + \hat{\rho}_s^2 k_\perp^2} \tag{4.15}$$

[5] The only alternative solution with $k_x > 0$ on the one side and $k_x < 0$ yields a singularity - or time reversal.

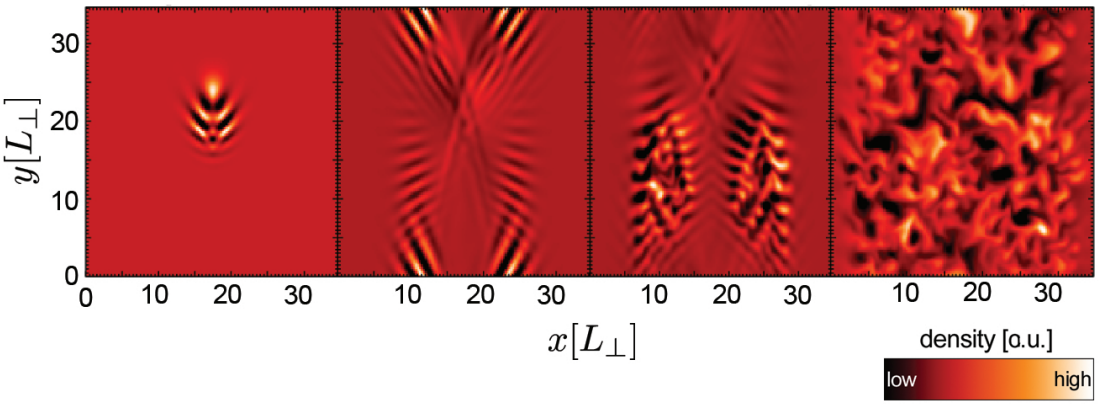

Figure 4.3: In this figure, four stages in the development of a nonlinear nonadiabatic drift wave system on top of a radial density gradient are depicted. Density in the radial-poloidal plane is plotted, with the length scales being normalized to $L_\perp$. Initially, a density distortion with a Gaussian seed has been placed in the center. According to the nonadiabatic versions of (4.5) and (4.6), the trademark fishbone wave pattern emerges - as seen in the first figure - and the drift wave amplitude begins to grow. Continuous boundary conditions lead to the drift wave ultimately interacting with itself (in reality, this happens with other embryonic drift waves) as shown in figure two. At these intersections, the amplitudes of the drift waves are the first to become sufficiently large to turn over into the nonlinear regime, exhibiting Kevin-Helmholtz instabilities (third figure). The turbulence spreads and saturates, eventually filling the entire domain (fourth figure).

A detailed overview over the group velocity in the nonadiabatic case (with shear) can be found in Figure 4.4. In a linear picture of the radial-poloidal plane (as depicted in the first part of Figure 4.3), no major qualitative differences have to be taken into account when comparing the nonadiabatic solutions with the adiabatic case shown in Figure 4.2, with the nonadiabatic group velocities remaining close to the adiabatic solutions shown in (4.5) and (4.6). However, contrary to pure adiabaticity - where propagation in the z-direction exists only in the presence of numerical hyperviscosity terms - standing[6] waves in the z-direction with a non-zero group velocity $v_{gr,z}$ exist.

The phase and group velocities in the z-direction in this system can then be calculated as

[6]The standing waves are due to the periodic boundary conditions.

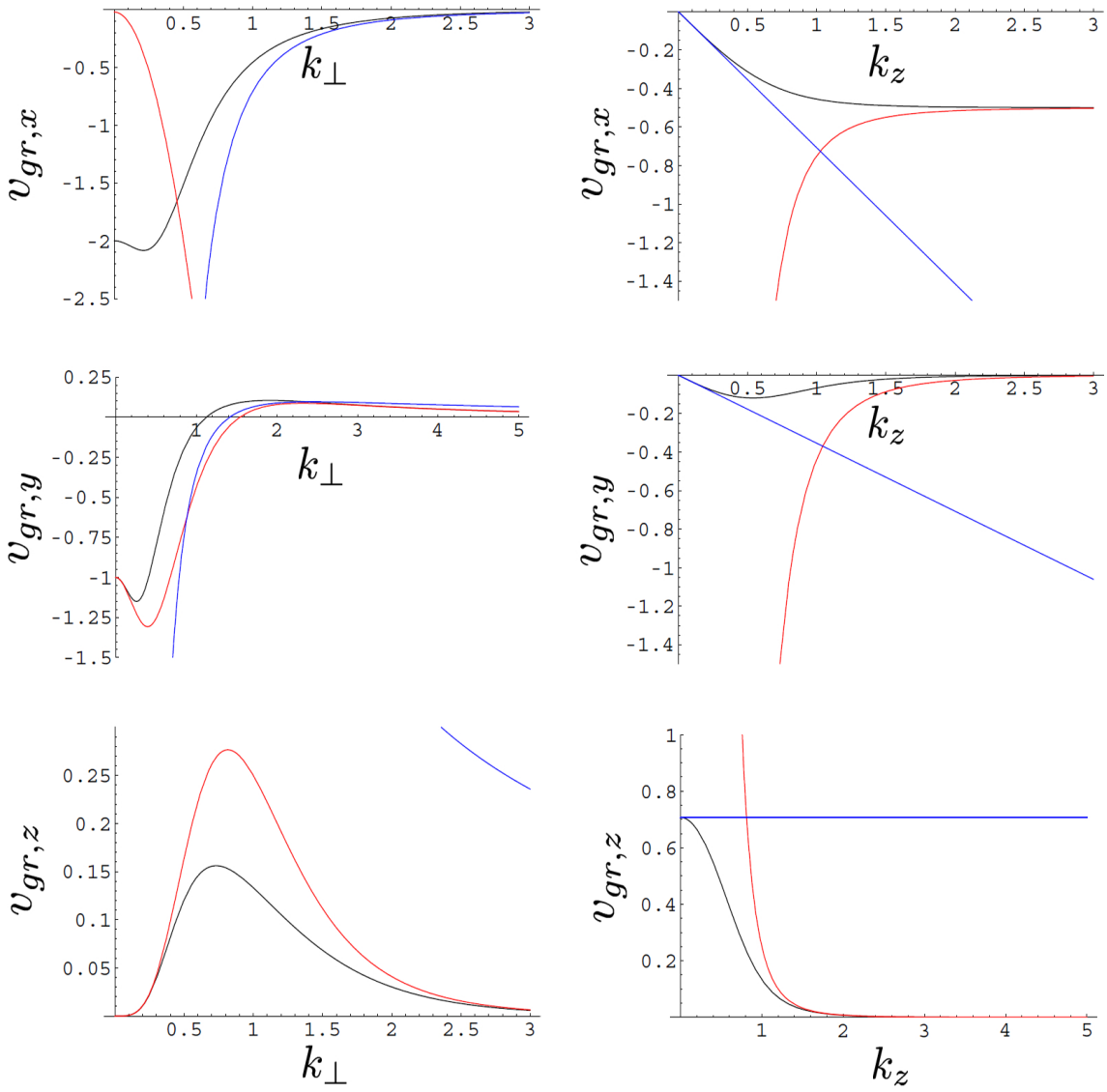

Figure 4.4: The exact analytical solutions for the group velocity components in the radial, poloidal and toroidal directions (x, y and z) are plotted in black against $k_\perp$ and k_z in dimensionless numerical units. While the red lines stand for an approximation in the high-$\hat{\rho}_s$- and high-k_z-regimes, the opposite extreme is marked in blue. In most cases, at least one of these regimes offers a decent approximation at either low or high values of $k_\perp$ and k_z, however, it becomes clear that only the full solution suffices when dealing with in-between values.

$$v_{ph,z} = \frac{1}{k_z\left(1+\sqrt{1-ik_z^{-2}}\right)} \tag{4.16}$$

$$v_{gr,z} = \frac{2k_y}{\left(1+\hat{\rho}_s^2k_\perp^2\right)}\left[1+\sqrt{1-\frac{4ik_\perp^2k_y}{\left(1+\hat{\rho}_s^2k_\perp^2\right)^2k_\parallel^2}}\right]^{-2}\cdot\frac{1}{2\sqrt{1-\frac{4ik_\perp^2k_y}{\left(1+\hat{\rho}_s^2k_\perp^2\right)^2k_\parallel^2}}}\cdot\frac{8ik_\perp^2k_y}{\left(1+\hat{\rho}_s^2k_\perp^2\right)^2}\cdot\frac{1}{k_z^3} \tag{4.17}$$

which, for large values of k_z, implies

$$v_{gr,z} \propto k_z^{-3} \tag{4.18}$$

4.2.3 Calculation of growth rate and stability

Taylor expansion up to the first order in $4ik_\perp^2k_y/\left(\left(1+\hat{\rho}_s^2k_\perp^2\right)^2k_\parallel^2\right)$ to eliminate the square root in (4.14) while only retaining the imaginary part leads to an approximate equation for the nonadiabatic drift wave growth rate which holds true unless $k_\perp$ or k_y become very large or $k_\parallel$ becomes very small.
In most practical cases, these limits hold true and the drift wave growth rate for small $4k_\perp^3 \ll k_\parallel^2$ will be very close to

$$\gamma \approx \frac{k_\parallel^2}{k_\perp^2}\left(1+\hat{\rho}_s^2k_\perp^2\right)\left[1+\left(\left(1+\hat{\rho}_s^2k_\perp^2\right)^2\frac{k_\parallel^2}{k_yk_\perp^2}\right)^2\right]^{-1} \tag{4.19}$$

so that with $k_\perp\hat{\rho}_s \lesssim 1$

$$\gamma \approx \frac{k_\perp^2k_y^2}{k_\parallel^2} \tag{4.20}$$

This result also allows the point of maximal growth (where $\gamma' = 0$ and $\gamma'' < 0$) to be determined. It is crucial to note that this maximum occurs at $k_x = 0$ (which is easy to understand, recalling the symmetry in the x-direction - as well as for z, n and p), but at $k_y \neq 0$ and $k_z \neq 0$:

$$k_x|\gamma_{max} = 0 \tag{4.21}$$

$$k_\perp|\gamma_{max} = k_y|\gamma_{max} = \hat{\rho}_s^{-1} \tag{4.22}$$

$$k_\parallel|\gamma_{max} \approx k_y|\gamma_{max} = \frac{1}{\sqrt{2\sqrt{2+\sqrt{5}}\hat{\rho}_s^{3/2}}} \approx 0.493\hat{\rho}_s^{-3/2} \tag{4.23}$$

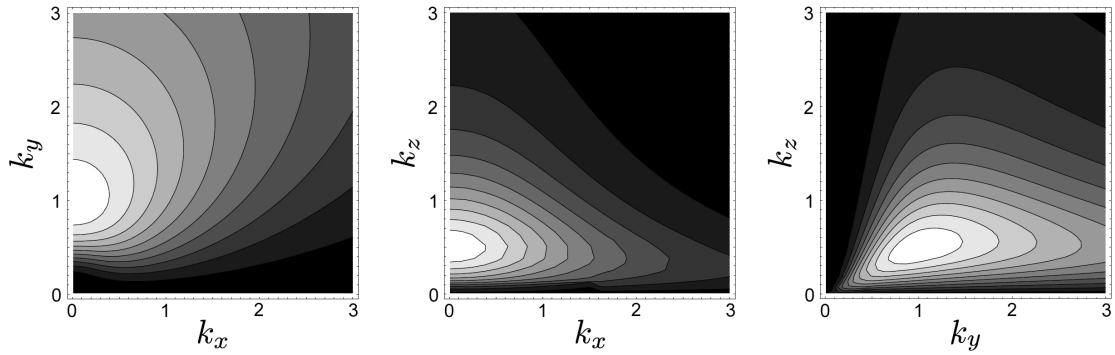

Figure 4.5: Analytical results for the drift wave growth rate around its maximal value (for $\hat{\rho}_s = 1$) are plotted in the k_x-k_y-, k_x-k_z- and k_y-k_z-planes. Increased brightness correlates with higher values of (4.24). The maximum occurs at the dimensionless values $k_x = 0$, $k_y = 1$ and $k_z \approx 0.493$.

Drift wave growth rates around this maximum are presented in Figure 4.5.

Here, a straightforward calculation yields the exact value of the maximal drift wave growth rate:

$$\gamma_{max} = \sqrt{\frac{5\sqrt{5}-11}{8}}\hat{\rho}_s^{-1} = \frac{1}{\hat{\rho}_s\sqrt{22+10\sqrt{5}}} \approx 0.150\hat{\rho}_s^{-1} \tag{4.24}$$

Thus the drift wave growth rate decreases as $\hat{\rho}_s$ increases. This is crucial for the high-$\hat{\rho}_s$-zonal flow-regime, where a reduced drift wave growth rate translates into a less strongly nonlinear system (as seen in Chapter 5).

A detailed comparison of the approximate solution for the drift wave growth rate presented in (4.19) with a straightforward, yet lengthy calculation of the exact results performed in Mathematica shows that the approximate results in (4.20) hold true very well for all $\hat{\rho}_s$ as long as $k_\parallel > k_\perp$. For $\hat{\rho}_s = 1$ and $k_\parallel = 10 \cdot k_\perp$, the error is merely 0.004%, for $k_\parallel = 2 \cdot k_\perp$ it is 1.5%. It grows to 20% for wavenumber parity, yielding increasingly imprecise results beyond. Reducing $\hat{\rho}_s$ to $\hat{\rho}_s = 0.2$ increases the error bars up to 0.05% for $k_\parallel = 10 \cdot k_\perp$ and 17% for $k_\parallel = 2 \cdot k_\perp$. For most practical case, however, $k_\parallel > 2 \cdot k_\perp$ holds true and (4.20) remains a good approximation.

A simple way of visualizing drift wave growth can be reached by drawing an analogy between a sinusoidal, growing density perturbation (the drift wave) and a one-dimensional driven harmonic oscillator. With a phase shift ϕ for the driving term and an artificial spring constant k, this becomes $F(\xi) \propto e^{i\phi}\dot{\xi} - k\xi$ so that the time derivative of the total energy yields

$$\dot{E} \propto |\dot{\xi}|^2 \cos\phi \tag{4.25}$$

reinforcing the result stated in Subsection 4.1.1. The energy input is maximal for a phase shift of $\phi = 0$ between $\dot{\xi}$ and the driving term, or $\phi = \pi/2$ between the elongation ξ itself (analogous to the density) and the driving term (provided by the electric potential).

Beyond pure drift wave effects, flow-shear-stabilization of resistive drift waves in toroidal geometries, even enhanced by a finite conductivity, leads to difficulties generating turbulence from linear instability under these regimes. In the presence of the adiabatically stabilizing effect of magnetic shear [79, 80], linear instability can only be achieved when the drift waves are able to couple to another mode - requiring nonadiabaticity. Purely adiabatic collisional drift waves in a sheared-slab configuration always remain linearly damped unless initialized nonlinearly [81].

4.3 Shear and instability

So-called resonant surfaces are capable of reflecting drift waves in a plasma.
With magnetic shear, translational symmetry is upheld in the y- and z-directions (and thus on each flux surface), but no more in the x-direction, since the parallel derivative is now

$$\partial_\parallel = \partial_z - s(x - x_0)\partial_y \tag{4.26}$$

instead of

$$\partial_\parallel = \partial_z \tag{4.27}$$

as it was before.
Thus, for shear $s \neq 0$ (which also serves to limit the maximum eddy size by its ability to tear them apart), $k_y = const.$, $k_z = const.$ and $\omega = \omega(k_x, k_y, k_z, x) = const.$ are constants of motions as known from classical and quantum mechanics. $k_x = k_x(x) \neq const.$, however, is not. Fourier-transformed and applied to drift waves, (4.26) becomes

$$\partial_\parallel = 2\pi i m - \frac{2\pi i n x}{L_s} \tag{4.28}$$

For every combination of m and n there is a radial value for which $\partial_\parallel = 0$. This is the basic definition of a resonant surface [20] (thus always causing one with $m = 1$ to occur in the center of the numerical domain for default parameters) - and accordingly, the distance between the two most basic resonant surfaces scales with L_y.

Drift waves heading towards a resonant surface are reflected upon impact[7], with some tunneling being possible as well. Such resonant surfaces develop in every sheared slab [82] system unless the z-direction is expanded into infinity, which enables the deskewing of field lines and thus sharp k_x within a twisted coordinate system.
The mode numbers can only be changed by the nonlinear interaction of two or more (nonadiabatic) drift waves, yielding $m_3 = m_1 + m_2$ as well as more complicated interaction. Otherwise, a drift wave's mode numbers remain constant.

The general spacing of resonant surfaces is influenced by the ratio L_s/L_p between the shear length L_s and the periodicity length, which marks the overall largest length fitting into the system. Increasing L_z prevents the drift waves from retaining their memory until they have traveled a full periodicity length, thus decreasing the influence of resonant surfaces by a factor proportional to L_s/L_p.
Due to the memory retention exhibited by the drift waves, global resonant surfaces bring along a self-mapping problem: In their vicinity, a drift wave will be able to interact with itself after merely one cycle in the z-direction has passed, well below its correlation length along the fieldline. This tends to lead to an overestimation of the flows to the disadvantage of the turbulent transport levels [83]. Unfortunately, increasing L_z to arbitrarily high values is not a viable option as this has been found to reduce zonal flow generation through artificial admission of nonphysical parallel wavelengths [84].
$L_z = 2\pi L_s$ is commonly chosen as an approximate in-between value[8] (and, again, in this work), in compliance with realistic tokamak parameters [83].

4.3.1 Resonant reflections

Recalling (4.14) and

$$\dot{k} = -\nabla\omega \tag{4.29}$$

(since $\partial_t k = \partial_x k \partial_t x = v_{gr,x}\partial_x k = -\partial_k \omega \partial_x k = -\nabla\omega$ is a general relation which holds true for every wave as seen in [11]), it is possible to construct a relation between ω, $k_\parallel$ and $k_\perp$, explaining why drift waves are reflected at resonant surfaces.
As seen in (4.26), $k_\parallel = 0$ holds true at the resonant surface by definition. Thus, $k_\parallel$ has to decrease while closing in on a resonant surface. The square root term in (4.14) can be Taylor-approximated by $\sqrt{1-x} = 1 + x/2 - x^2/8$ (with $x = 4i\alpha_d k_\perp^2 k_y / \left((1+\alpha_d k_\perp^2)k_\parallel^2\right)$ being used), of which only $1 - x^2/8$ contributes to the real part of ω. It increases for $k_\parallel$, appearing to lead to decreasing values of ω. Since ω remains constant though, the radial wavenumber k_x within $k_\perp$ has to decrease to compensate for the decrease in $k_\parallel$. But since

[7] Due to this interaction with the drift waves and the thus changed behavior of the turbulent modes, resonant surfaces may be marked by small spikes in the Reynolds stress picture.

[8] The self-mapping issue can be abated further by prescribing non-quadratic radial-poloidal domains with e.g. $L_y = 4L_x$ or $L_y = 8L_x$ [84] together with phaseshifting the main resonant surface away from the radial center.

$v_{gr,x} \to 0$ for $k_x \to 0$, the radial drift wave group velocity not only decreases, but actually reaches zero and - instead of turning imaginary - reverses its sign[9], thus confirming that drift waves exhibit reflections at resonant surfaces.

Resonant surfaces are also crucial for drift wave growth. Far away from their sphere of influence, $k_\parallel$ becomes very large, leading to $\gamma_{DW} \approx 0$ - instead of the strong values of γ_{DW} experienced in their vicinity[10].
Still, little linear drift wave growth is possible as long as shear is present - even after reflection or penetration, the drift wave growth dies down again to its initial strength (not including any additional damping effects). The only actual growth that can then be achieved is through spatial comigration of drift wave eigenmodes, even if the single eigenmodes decrease in amplitude. This no-growth statement does not hold true in the shearless case, where k_x stays constant and the amplitude grows.
When damping effects are considered, high k modes are especially vulnerable. And since the drift waves exhibit a quasi-Kolmogorov development as described in Section 2.4, diffusion to the highest wavenumber takes place and damping becomes relevant. This is also a necessary reaction to the drive at small k, since large-scale modes profit strongly from the resonant backscattering effect. On a first glance, it is not quite clear which process claims responsible for this scattering to small wavelengths. The direct drift wave - drift wave interaction is very weak, especially so for low k and adiabaticity, as it then only stems from the Laplacian in (4.10). However, another possibility for the scattering to small wavelengths will be discussed in Chapter 5.

Adiabaticity thus cannot lead directly to drift wave turbulence. As seen in (4.1), or more precisely, $n = \phi - \langle\phi\rangle$ (with $\langle\phi\rangle$ being the flux surface averaged mean of the potential, implying that adiabaticity only applies to a flux surface), both the left hand side and the right hand side must remain constant over time due to (3.36) turning into $\partial_t n = 0$. This deprives the density of any chance of accessing the free energy stored in the density gradient. No adiabatic drift wave turbulence can thus develop.

4.3.2 Onset of turbulence

As shown in Subsection 4.3.1, the resistive drift waves are linearly stabilized by the magnetic shear [79], even more so with increasing collisionality [82]. This picture breaks down, however, in the nonlinear drift wave regime, when the nonlinear drift instability is reached. Although the resonant surfaces cannot provoke an enduring growth of the reflecting drift waves, it endows them with a short window of opportunity (around their closest approach and thus highest amplitude, determined by integrating over the entire approach towards the resonant surfaces) where the likelihood of nonlinear interactions is drastically increased. Collisions between different wave packets lead to merely a small percentage of the amplitude being reflected, but due to extremely high rates of amplification,

[9] Also, a glance at the group velocity shows that there can be no place with $k_x \neq 0$ for $v_{gr,x} = 0$.

[10] For the drift waves, the resonant surfaces are thus akin to what the Nile river has been since the dawn of man: Daunting, crocodile-infested waters - lined with the only fertile stretches of land far and wide.

only around 0.01% of the amplitude is required to undergo this turbulent backscattering process to achieve overall amplification, and even less so in case of weak shear. The amplification factor is highest for small $k_{||}$ and thus especially so near resonant surfaces.

Therefore, due to the high growth rates exhibited near resonant surfaces, drift waves are likely turning turbulent there first, once they interact nonlinearly with each other on a sustainable level. After a certain amplitude threshold is overcome[11], enough backscattering occurs to keep up the chain reaction, ultimately filling the entire domain with strong turbulence. An initial overshoot is subsequently reduced by saturating nonlinear terms, preventing infinite amplification.

4.3.3 Numerical considerations

In the nonlinear case, it suddenly becomes a pressing issue to prevent certain values from growing artificially.
Since in this work most phenomena are examined for their long-term stability, hyperviscosities turn into an particularly big problem, especially so in the z-direction. A disproportionate reduction of the gyroradius in comparison to the system size, ϵ_n is harmful, since all gyroradii effects as well as all nonlinear drift wave - drift wave interactions cease for $\epsilon_n \to 0$, as seen in (3.37). The addition of a special hyperviscosity / hyperdiffusivity parameter of 4th order (dubbed ν_4) to the density equation guarantees the long-term consistency of the numerical run for reasonable values of ϵ_n. It functions as an artificial diffusion term designed to disproportionally affect high-frequency modes, dissipating their free energy before they cross the resolution limit, preventing structure aliasing. This hyperviscosity parameter affects a variable a via $\dot{a} = -\partial_{x^2}(|v_x|\partial_{x^2}a)$, being proportional to $|v_x|$ since higher $|v_x|$ are more likely (and more quickly) to be involved in the creation of small structures.
ν_4 needs to be fine-tuned rather accurately in order to smooth out the density structures while not tampering with the correct results (such an occasion can often be identified easily when structures move $\propto t^{1/4}$). Once this is achieved, the hyperviscosity term proves to be very effective in preventing parallel unsmoothness, which could otherwise happen even at very high resolutions, canceling the $v\nabla$-terms occurring at the smallest scales.

Also, a parameter μ_{grid} has been utilized to prevent small-scale high-$k_\perp$ modes from exiting the system at the maximum frequency and re-entering it with extremely large wavelengths on the other side by damping them prematurely. The associated Nyquist frequency [85] is generally defined to be 50% of the sampling frequency

$$f_{ny} = 0.5 \cdot f_{sampling} \tag{4.30}$$

which in this case is given by the system resolution. The maximal occurring frequency should thus lie below f_{ny} in order to fulfill the Nyquist criterion and prevent high-k-reentry.

[11] The proportion of quadratic terms versus linear terms scales up proportional to the amplitude.

While essential during nonlinearity, both μ_{grid} and ν_4 are unnecessary in the initial linear phase (or even harmful, if too low or too high values are chosen), making it imperative for them to be balanced carefully and to be reevaluated for changes in other parameters.
Due to their similarities, decreasing μ_{grid} is a practical alternative to increasing the hyperviscosity term.

Another big issue in almost any numerical work are border effects, which can become very prominent by yielding vortices of the same size as the simulation box. Reducing the relative eddy size by keeping ϵ_n constant while increasing L_x as well as L_y solves that issue, while of course requiring higher n_x and n_y - at least if the same relative resolution is desired - thus proving costly to computational resources. Alternatively, if not all physical effects are required for a certain analysis (necessitating control runs, though), n_x and n_y may remain the same. The advantage of this reduction in resolution is a better chance to meet the Courant-Friedrichs-Lewy criterion [86] which requires the time step to be

$$\Delta t \leq \frac{\Delta x}{u} \tag{4.31}$$

with u being the maximal velocity occurring within the equation system as well as Δx representing the mesh width.
Even (radially constant) zonal flows can occur as purely domain effects, when artificial drift waves enter the domain at its borders, slowly increasing the total momentum of the flow. However, this can be prevented by holding the outermost areas constant - and even it this effect occurs, it is merely a constant addition of flow and thus, due to Galilei invariance, of no danger to the relative results.

A more serious problem can arise due to Alfvén waves [87], magnetohydrodynamic waves which exist in the interplay between the tension of the magnetic field lines and the inertia of the ions (and electrons), their simplest incarnation being a magnetosonic wave propagating perpendicular to the magnetic field. In numerically analyzed Hasegawa-Wakatani equations as examined in this work, theses waves only appear within artificial numerical parameters. If their velocity comes close to the drift wave phase velocity, however, the ensuing interaction between Alfvén and drift waves changes many of the system's parameters drastically, rendering it more difficult to achieve zonal flows. Thus Alfvén transit time needs to remain lower than the highest occurring turbulence frequency. According to the Alfvénic dispersion relation, which - without curvature and parallel velocity, and discarding a hot ion term $\propto k_\perp^2 \rho_s^2$ - comes down to

$$\omega^2 = \frac{1}{(2\pi^2)\alpha_m} k_\parallel^2 \tag{4.32}$$

the Alfvén velocity is defined as

$$v_{Alfven} = \sqrt{\frac{1}{(2\pi)^2 \alpha_m}} \tag{4.33}$$

where the full Alfvén parameter is defined as a ratio between the particle pressure and the magnetic field,

$$\alpha_m = q^2 R \frac{8\pi \left(p_{e,0} + p_{i,0}\right)}{B^2} \frac{1}{L_n} \tag{4.34}$$

Setting the Alfvén frequency equal to the highest possible frequency yields a relation between $\alpha_m^{-0.5}$ and the inverse product of number of calculation boxes and the time step: Thus smaller time steps require smaller values of α_m. Equally, lower $L_{x,y}$ or higher $n_{x,y}$ lead to increased resolution and maximum frequency, and α_m (or the surrogate parameter $\alpha_{m_{add}}$) must be reduced to increase the Alfvén velocity accordingly.

It is important to note that no Alfvén waves exist in a perfectly adiabatic drift wave system: The electrons adapt instantaneously to the electric potential, thus no magnetic field line curvature distortions form and no Alfvén waves develop.

4.4 A single dimensionless parameter

One of the most important properties of a fusion plasma is the strength of the turbulent transport, as it is crucial to confinement. In order to derive a useful transport expression, the free parameters governing the basic equations (4.9) and (4.10) have to be analyzed. As introduced in (3.18)

$$\hat{\rho}_s = \frac{\rho_s}{L_\perp} = \epsilon_n^{1/2} \left(\alpha_d s\right)^{2/3} \tag{4.35}$$

is the only parameter that can influence which development this sheared-slab drift wave system may take - apart from quantization effects for insufficient domain sizes and the secondary influence of the radial positioning of resonant surfaces, as mentioned before.
As defined in Section 3.1, $\hat{\rho}_s$ is a dimensionless parameter, being the ratio of two length scales orthogonal to the magnetic field, the ion sound Larmor radius ρ_s and the resistivity length scale $L_\perp$ - the scale of maximal drift wave growth where the drift wave relaxation (equilibrium return) frequency equals the diamagnetic frequency (in which (4.9) and (4.10) have been written originally). $\hat{\rho}_s < 1$ thus marks the regime where the gyroradius is smaller than the scale where the drift time equals the relaxation time, rendering $t_{relax} > t_{drift}$. In physical units, these two length scales are defined as

$$\rho_s = \frac{m_i}{eB}\sqrt{\frac{T_e}{m_i}} \tag{4.36}$$

$$L_\perp = \frac{m_e}{m_i B}\left(\frac{\pi q R}{s}\right)^{2/3}\left(\frac{n_0 \eta_\parallel T_e}{2q\sqrt{m_i}L_n}\right)^{1/3} \tag{4.37}$$

where, as usual, m_e and m_i mark the electron and ion mass, T_e the electron temperature, e and q the electron and ion charge, B the magnetic field and s the shear. n_0 is the background density, $L_n = -n\frac{dx}{dn}$ stands for the density gradient and $\eta_\parallel$ is the parallel resistivity.

Now it is obvious that there must be a parameter range for which the ion gyroradius ρ_s is dominant ($\hat{\rho}_s > 1$) and one where the resistivity length scale is more important ($\hat{\rho}_s < 1$), with a dividing line drawn somewhere between two distinct orthogonal length scales[12] - later to be associated with a transition between two different transport regimes.

As discussed in Section 4.3, parallel drift wave trapping by the shear s becomes significant for high values of $\hat{\rho}_s$, reducing drift wave amplitudes considerably, with larger $k_\parallel$ implying a decreased growth rate. Similarly, higher values of $\hat{\rho}_s$ correspond to reduced collisionality and thus increased suppression of the nonlinear instability.

4.4.1 Alfvénic influence

Since Alfvénic-like fluctuations have been shown to be influential in experimental drift wave zonal flow systems [88], it is conceivable that a third, Alfvén-based scale exerts influence on both the drift wave structure and the resulting flows by interaction with the turbulent drift wave eddies [87] when Alfvén waves are introduced in addition to the simple $\hat{\rho}_s$-dominated system as described in (3.37) and (3.38). Implementing a finite value of α_m for instable drift waves (thus entering the finite-beta-regime) yields a third time scale, constructed from the Alfvén velocity and the shear length to give

$$t_{Alfven} = 2\pi\sqrt{\alpha_m}L_s \tag{4.38}$$

yielding a third length scale when compared with the drift wave velocity:

$$L_{Alfven} = 2\pi\sqrt{\alpha_m}\alpha_d L_s \tag{4.39}$$

It can be shown, however, that this third scale is without actual implications for the drift waves discussed in this work. The most important scale-determined system parameter, the turbulent transport, remains uninfluenced by a change in α_m, in this work ususally chosen to lie between $\alpha_m = 4e\text{-}5$ and $\alpha_m = 6.4e\text{-}4$, the highest levels of α_m which are

[12] These two length scales correlate with two diffusion processes - one for high $\hat{\rho}_s$ that can (among others) be associated with a gyroring diffusion and an anomal transport process for low $\hat{\rho}_s$.

compatible with the other numerical parameters if Alfvén waves are not desired (further lowering of the value increases the risk of numerical irregularities, as discussed in Subsection 4.3.3). Increasing α_m does indeed influence Alfvén wave generation as expected, but it neither influences the development of zonal flows - including their asymmetry discussed in Chapter 6 - nor the turbulent transport (or any other major drift wave parameters). In fact, steady state turbulent transport remains virtually untouched, with mean values of the radial density flux

$$\langle nv_x \rangle = -\langle n\partial\phi/\partial y \rangle \tag{4.40}$$

deviating by less than 1% over several orders of magnitudes of α_m, as presented in units of $L_\perp$ in Table 4.1 where *) denotes an artificial $\alpha_{m_{add}}$-parameter being present for numerical stability.

Table 4.1: α_m-dependency

α_m	0.00000*	0.00004	0.001	0.0004	0.001	0.004
$< nv_x >_{L_\perp}$	0.0688	0.0696	0.00691	0.0692	0.0691	0.0695

Thus, a potential third scale is of no significance for the drift wave development, especially so in the most relevant $\hat{\rho}_s = 0.1 - 1.0$-regime.

4.4.2 Mixing length estimate

In order to compare the transport levels in both scales, a mixing length estimate is utilized, based on a theory originally conceived by Ludwig Prandtl and developed within the geophysical community [89], which has only recently been applied to cases of plasma turbulence [90]. The mixing length is the approximate distance that a turbulent eddy is capable of moving while retaining its original properties (e.g. its density). Once it absorbs the properties of its new surroundings, the mixing length is exceeded - it is thus analogous to the thermodynamic mean free path. Consequently, the turbulent particle flux $\vec{\Gamma} = \langle n_1 \vec{v} \rangle$ (the mean value of the density fluctuations times their total velocity) can be written as

$$\vec{\Gamma} = -D\nabla n \tag{4.41}$$

where the experimental results for the diffusion coefficient D vastly exceed classical and even neoclassical estimates including gyro effects. Neoclassical transport is mostly caused by particles trapped on banana orbits which are an effect of magnetic mirroring. Since the banana orbit width in a tokamak turns out to be $q\sqrt{R/r}$ larger than the gyroradius, $D_{neoclassical} \approx 100 D_{classical}$. But still, a major discrepancy remains: $D_{turbulent} \approx 10 D_{neoclassical}$.

The mixing length argument-based diffusion coefficient D has a unit of $[distance^2/time]$ and is usually written as the ratio between the growth rate γ and the square of the (orthogonal) wavenumber $k_\perp^2$,

$$D = \frac{\gamma}{k_\perp^2} \tag{4.42}$$

There is one caveat, however. Although the sheared system is to be analyzed, its eigensystem cannot easily reproduce the development of the zonal flow states examined in Chapter 5 or be used directly in a mixing length estimate due to its non-orthogonality, which is caused by the shear-induced time evolution asymmetry. There is no feasible decomposition for this non-orthogonal, nearly collinear eigensystem, so developing single eigenvectors on their own is rendered impossible. Strictly speaking, there are no growing eigenmodes for $s \neq 0$. Thus the linear properties of these states are still best characterized by the eigenvalue of the unsheared system. Consequently, the general growth rate of modes in the shearless, nonadiabatic case - a simplified version of (4.19) derived from (4.9) and (4.10), but without the $x\partial_y$-term, marking a linearized wave packet for fixed $\vec{k}$ - applies, being approximated by a growth rate[13]

$$\gamma \approx \frac{k_\perp^4}{k_\parallel^2} \tag{4.43}$$

4.4.3 Two distinct transport regimes

Recalling that (4.9) and (4.10) describe the equation system in units of $L_\perp$ (and thus also (4.43)), it is possible to determine the mixing length estimate-based diffusive transport for both scales, in units of $L_\perp$ as well as in units of ρ_s. The according diffusion coefficients are defined as

$$D_{L_\perp} = \frac{\gamma_{L_\perp}}{k_{L_\perp}^2} \tag{4.44}$$

$$D_{\rho_s} = \frac{\gamma_{\rho_s}}{k_{\rho_s}^2} \tag{4.45}$$

Now, (4.43) is inserted with the additional condition $k_\parallel = 1$ (since $k_\parallel$ is of no concern for the perpendicular behavior). Focussing at the modes determined by $k_\perp = L_\perp^{-1}$ in the $L_\perp$-dominated low-$\hat{\rho}_s$ regime yields in units of $L_\perp$ and ρ_s respectively

$$D_{L_\perp}|_{k_\perp \widehat{=} L_\perp^{-1}} = \frac{\gamma_{L_\perp}}{k_{L_\perp}^2}|_{k_\perp \widehat{=} 1} \propto \hat{\rho}_s^0 \tag{4.46}$$

$$D_{\rho_s}|_{k_\perp \widehat{=} L_\perp^{-1}} = \frac{\gamma_{\rho_s}}{k_{\rho_s}^2}|_{k_\perp \widehat{=} L_\perp^{-1}} \propto \hat{\rho}_s^2 \tag{4.47}$$

[13] This ansatz is only valid when the wave packet is restricted along the magnetic fieldlines, restricting lower values of $k_\parallel$ according to $\lambda/(2\pi) \approx 1/k_\parallel < k_x/(sk_y)$.

since $k_\perp \mathrel{\widehat{=}} L_\perp^{-1}$ is simply 1 in units of $L_\perp$ while being $\hat{\rho}_s$ in units of ρ_s.
Similarly, the condition $k_\perp = \rho_s^{-1}$ dominating in the ρ_s-dominated high-$\hat{\rho}_s$ zonal flow regime yields in units of $L_\perp$ and ρ_s respectively

$$D_{L_\perp}|_{k_\perp \mathrel{\widehat{=}} \rho_s^{-1}} = \frac{\gamma_{L_\perp}}{k_{L_\perp}^2}|_{k_\perp \mathrel{\widehat{=}} \rho_s^{-1}} \propto \hat{\rho}_s^{-2} \tag{4.48}$$

$$D_{\rho_s}|_{k_\perp \mathrel{\widehat{=}} \rho_s^{-1}} = \frac{\gamma_{\rho_s}}{k_{\rho_s}^2}|_{k_\perp \mathrel{\widehat{=}} 1} \propto \hat{\rho}_s^{0} \tag{4.49}$$

Here, the drift wave growth rate (4.19) for a fixed $k_\perp$ decreases with increasing values of $\hat{\rho}_s$, reducing the steady state turbulence levels with it. Additionally, as can be deduced from (2.23) and (2.24), $\hat{\rho}_s$ interferes with unconstrained $\vec{E}\times\vec{B}$-convection, hampering the nonlinear drift wave mechanism, with only weak nonlinearities remaining on top a linear stability.

Now, with (4.46)-(4.49), a simple equation relating between the two unit scales results:

$$\frac{D_{L_\perp}}{D_{\rho_s}} = \hat{\rho}_s^{-2} \tag{4.50}$$

or, checking this result by an analysis of the units occurring the density flux (which differs only by a constant since the density gradient in $\Gamma = \langle n v_x \rangle = -D\nabla n$ is seen as constant)

$$\begin{aligned} & \langle n_{L_\perp} {L_\perp}^{-3} v_{x_{L_\perp}} L_\perp / t \rangle = \langle n_{\rho_s} {\rho_s}^{-3} v_{x_{\rho_s}} \rho_s / t \rangle \\ \Rightarrow \quad & \langle n v_x \rangle_{L_\perp} \frac{1}{L_\perp^2 t} = \langle n v_x \rangle_{\rho_s} \frac{1}{\rho_s^2 t} \\ \Rightarrow \quad & \frac{\langle n v_x \rangle_{L_\perp}}{\langle n v_x \rangle_{\rho_s}} = \hat{\rho}_s^{-2} \end{aligned} \tag{4.51}$$

where the same unrescaled time scale was employed in both density fluxes and the same flux-surface average was taken since this correlates with the approach used in determining the numerical density fluxes.

This result presented in (4.50) has been verified thoroughly by numerous numerical parameter scans over $\hat{\rho}_s$ for a broad variety of support parameters, with resolutions of up to 512x512x128 points in the x, y and z directions, up to $L_x = L_y = 64$ (roughly equal to 50 units of $L_\perp$, which would be equivalent to approximately 8 zonal flow oscillations) and $L_z = 4$ and run times reached far beyond the stationary steady state limit.

As visualized in Figure 4.6 and reproduced in Tables A.1 and A.2, the computational values of the flux surface-averaged density fluxes $\langle n v_x \rangle$ are in agreement with the above calculated units of the diffusion coefficients - the numerical values of both being connected as seen in (4.41). This can be seen by comparing the analytical expectation of the $D_{L_\perp}$-units,

$$D_{L_\perp}|_{\hat{\rho}_s \to 0} \to const. \tag{4.52}$$

for the low-$\hat{\rho}_s$-regime with the numerical evidence for the density flux

$$\langle n v_x \rangle_{L_\perp}|_{\hat{\rho}_s \to 0} \propto \hat{\rho}_s^{-0.004 \pm 0.02} \tag{4.53}$$

offering extremely satisfactory accordance with the theoretical result, while in the high-$\hat{\rho}_s$-regime

$$D_{\rho_s}|_{\hat{\rho}_s \to \infty} \to const. \tag{4.54}$$

is confirmed - albeit with slightly less precision - to be correct as well:

$$\langle n v_x \rangle_{\rho_s}|_{\hat{\rho}_s \to \infty} \propto \hat{\rho}_s^{0.06 \pm 0.20} \tag{4.55}$$

The higher imprecision of the high-$\hat{\rho}_s$-results is caused by convergence issues in that regime: As can also be seen in Figure 4.6, where the numerical measurements are presented, the otherwise fully converged parameters of $n_{x,y} = 64$ and $L_{x,y} = 8$ (all values for $\hat{\rho}_s < 0.4$, and then the lightest colors for $\hat{\rho}_s \geq 0.4$) have to be doubled and quadrupled (plotted as the medium-colored data points for $n_{x,y} = 256$ and $L_{x,y} = 16$ or $L_{x,y} = 32$ at $\hat{\rho}_s \geq 0.4$) or even octuplicated each (marked by the strongest colors for $n_{x,y} = 512$ and $L_{x,y} = 64$ at $\hat{\rho}_s \geq 0.4$) in order to achieve near-convergement. Doubling the radial-poloidal domain size $L_{x,y}$ - necessary for approximately every 1.4-fold increase in $\hat{\rho}_s$ - without also increasing the numerical resolution $n_{x,y}$ leads to artificial artifacts rather easily, yielding the approximate requirement $n_{x,y}/L_{x,y} \geq 8$ in order to attain a sufficient resolution. Doubling $n_{x,y}$ however quadruples the necessary computational power. In addition to the already slowly evolving steady state for high values of $\hat{\rho}_s$ exhibiting a $\hat{\rho}_s^4$-proportionality (compare (6.4)), doubling $\hat{\rho}_s$ within the high-$\hat{\rho}_s$-regime thus provokes an extreme surge of the computational costs.

Ultimately, while for medium values of $\hat{\rho}_s$, $n_{x,y} \geq 64$ with $n_{x,y}/L_{x,y} \geq 8$ necessary[14] and $n_z \geq 32$ with $L_z \geq 1$ are found to be sufficiently converged, $n_{x,y} = 128$ with $L_{x,y} = 8$ are chosen for $\hat{\rho}_s < 0.4$ and $n_{x,y} = 256$ with $L_{x,y} = 16$ or $L_{x,y} = 32$ as well as $n_{x,y} = 512$ with $L_{x,y} = 64$ beyond (allowing four full zonal flow wavelengths to fit within the domain). A smooth transition at the point of parameter change is verified.
Under these conditions, excellent convergence within the numerical system is achieved for both low and medium values of $\hat{\rho}_s$ while the corresponding picture beyond $\hat{\rho}_s \approx 0.4$ depends strongly on the chosen domain size. For $L_{x,y} = 8$, marked in yellow and cyan, convergence

[14] Otherwise, reducing the resolution in order to bump the time step (as the Courant criterion is easier to uphold) together with an increased $\alpha_{m_{add}}$ would be the easiest option to facilitate such high-$\hat{\rho}_s$-runs.

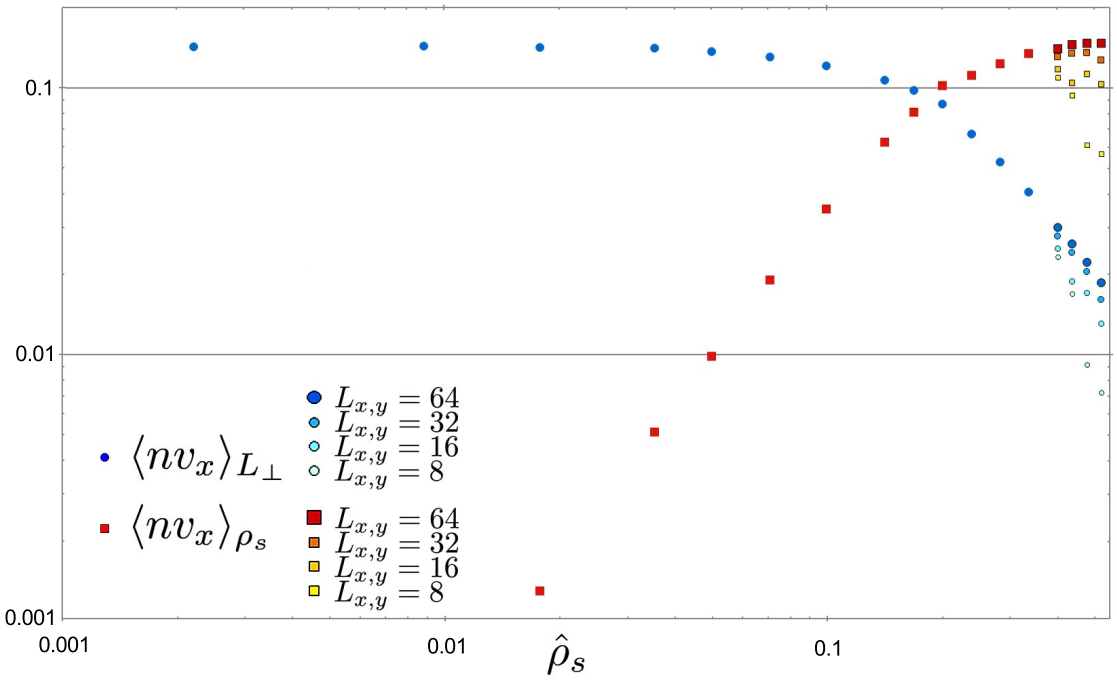

Figure 4.6: In this graph, density flux is plotted versus the dimensionless parameter $\hat{\rho}_s$, according to the values presented in Tables A.1 and A.2. The averaged computational data for the density flux $\langle nv_x \rangle$ in units of the radial length scale $L_\perp$ (marked in blue) converges for low levels of $\hat{\rho}_s$ and decreases $\propto \hat{\rho}_s^{-2}$ for higher values of $\hat{\rho}_s$, while the density flux in units of the second orthogonal length scale ρ_s (marked in red) exhibits the opposite behavior, with a plateau for high $\hat{\rho}_s$ following an increase $\propto \hat{\rho}_s^2$ for low values of $\hat{\rho}_s$. Thus, the transport values in units of ρ_s converge to a constant for high $\hat{\rho}_s$ while those in units of $L_\perp$ converge for low $\hat{\rho}_s$. The transitional region with respect to the two convergence regimes positions itself around $\hat{\rho}_{s,transition} \approx 0.15 - 0.20$ (determined more precisely to be $\hat{\rho}_{s,transition} = 0.185$). The reddish density flux values in units of $L_\perp$ are therefore plotted increased by a factor of $1/(\hat{\rho}_{s,transition})^2 \approx 29$ in order to be shown in the same graph (and in order to visualize the transition between the two transport regimes), since by definition they reach a similar level as those in units of ρ_s only for $\hat{\rho}_s = 1$. For $\hat{\rho}_s > 0.4$, lighter colors denote less converged data points for $L_{x,y} = 8$, $L_{x,y} = 16$ and $L_{x,y} = 32$, respectively, while red and blue mark the converged results for $L_{x,y} = 64$, illustrating the convergence issues occurring solely in the high-$\hat{\rho}_s$-regime.

fails. For $L_{x,y} = 16$ and especially $L_{x,y} = 32$, depicted in different shades of orange and turquois, near-convergence is reached, however, as verified in even more demanding test runs, only $L_{x,y} = 64$ is truly converged.

Empirically, the following approximate convergence relation concerning the density flux in units of ρ_s for different values $L_{x,y}$ and $\hat{\rho}_s$ (in dimensionless numerical units) has been established

$$\langle nv_x \rangle_{\rho_s,measured} = \langle nv_x \rangle_{\rho_s,converged} - \frac{0.0086 \cdot \exp\left(-\left(L_{x,y}/8\right)^{0.75}\right)}{1 + 0.1 \cdot \exp\left(-\left(8 + 160/L_{x,y}\right)\left(\hat{\rho}_s - 0.5\right)\right)} \quad (4.56)$$

The respective numerically converged results approximate the theoretical expectations very well, yielding the results shown in (4.53) and (4.55).

All results have been thoroughly checked by parameter screenings for the background velocity $V0$, the resolution and scale parameters $n_{x,y,z}$ and $L_{x,y,z}$ and the hyperviscosity-related parameters ν_4 and μ_{grid} as well as the Alfvénic $\alpha_{m_{add}}$ - leading to the reference parameters $V0 = 0.01$, $\nu_4 = 5.e\text{-}6$, $\mu_{grid} = 0.09$ and $\alpha_{m_{add}} = 4.e\text{-}5$, while $n_{x,y,z}$ and $L_{x,y,z}$ were forced to adapt to growing $\hat{\rho}_s$.

Typical error bars for all these runs are around 1% for lower values of $\hat{\rho}_s$, due to certain persistent fluctuations.
In the zonal flow regime, they soon become higher (up to 5% for $\hat{\rho}_s \approx 0.5$) as these runs have spent less time around the final steady state exhibiting fully developed zonal flows (transport is increased when flow rearrangement takes place, distorting the measurements), and have experienced a more pronounced initial transport overshoot during zonal flow formation as well as being less suited for the construction of long-term averages due to low-frequency fluctuations.
Still, 5% is a decent result, achieved through long-running simulations as well as numerous verifications. Error bars have been reduced so far that they are not even visible within Figure 4.6 since they are smaller than the squares marking the respective data values.

Despite those initial problems, these numerical parameter scans constitute a considerable success. Two distinctly different behaviors within two distinctly different transport scales have been discovered and presented in [91], being consistent with the theoretically expected dominance and leveling-out of ρ_s for high values of $\hat{\rho}_s$ and of $L_\perp$ for small $\hat{\rho}_s$.
These findings differ from previous expectations [92], where the nonlinear instability was thought to cut off for higher values of $\hat{\rho}_s$ - as appears plausible when only looking at the decrease in drift wave-units $D_{L_\perp}$ with rising $\hat{\rho}_s$. But due to a switching of the turbulence scale length from a drift wave-based unit $L_\perp$ to ρ_s for sufficiently large values of $\hat{\rho}_s$, D_{ρ_s} has actually been found to converge to a constant instead of decreasing to zero.

Interestingly, the transition between these two regimes occurs empirically at $\hat{\rho}_s \approx 0.15 - 0.20$, which, as will be seen in Chapter 5, coincides very well with the onset of zonal flow formation at the beginning of the ρ_s-regime, requiring $\hat{\rho}_s \gtrsim 0.15 - 0.20$.

Now, the mean values over several simulation batches each are presented. The density fluxes (in dimensionless numerical units) in the late-time stable state, depending on $\hat{\rho}_s$, and in the units of $L_\perp$, are measured to be as seen in Table A.1.

This offers very good qualitative agreement not only with the theoretically expected decline and experimental transport coefficients as discussed in [63][15], but also with some of the first sheared drift wave turbulence examinations performed in 3D [63] (albeit those being limited to $\hat{\rho}_s \approx 0.05 - 0.16$), while the previously unexplored density flux in units of ρ_s is found to be as shown in Table A.2.
So although $-n\partial\phi/\partial y|_{L_\perp}$ exceeds $-n\partial\phi/\partial y|_{\rho_s}$ only beyond $\hat{\rho}_s = 1$, the transition between both transport plateaus occurs considerably earlier, at $\hat{\rho}_s \approx 0.15 - 0.20$.

All of these results have been derived by varying ϵ_n. Comparing them with those based on varying α_d or s yields very good agreement, as can be seen exemplarily in Table 4.2, (with all values being measured in units of $L_\perp$), reinforcing that $\hat{\rho}_s$ is indeed the only necessary parameter to describe the system.

Table 4.2: Comparison of ϵ_n, α_d and s

$\hat{\rho}_s$	0.201	0.402
$\langle nv_x \rangle_{\epsilon_n}$	0.0898	0.0235
$\langle nv_x \rangle_{\alpha_d}$	0.0893	0.0246
$\langle nv_x \rangle_s$	0.0921	0.0249

As expected theoretically by recalling the definition of ρ_s in (3.15), higher values of ρ_s (correlating with higher values of ϵ_n) imply increasingly larger drift wave eddies in comparison with L_x. In numerical simulations, this can already be seen with the naked eye, but it has also been confirmed by an analysis of the peaks and cutoffs of the Fourier-transformed drift wave density (see Figures 6.4 and 6.7) - and indeed, for a full set of parameters in zonal flow-exhibiting drift wave turbulence, drift wave eddies scale almost perfectly with ρ_s while not at all with $L_\perp$.
The same holds true for the drift wave scale itself, as measurements of the maximal frequency in the spectrum show.

[15] There is a quantitative, systematical difference in the precise transport values, however. This originates most likely in a different hyperviscosity term utilized in [63], together with a smaller resolution and smaller domain size, which may not have been sufficient to yield fully converged results.

Chapter 5

Zonal flows

This chapter deals with the plasma flow phenomena collectively known as zonal flows. There are also atmospheric zonal flows, large east-west storm bands both on Earth (jet streams being a prominent example) and on gas giants (such as Jupiter's band structure), which are important for their respective body's climate and will be discussed in more detail in Chapter 7, but for now it is all about $\vec{E} \times \vec{B}$ plasma flows, currently being a topic of major research, both theoretically and experimentally.

Zonal flows, which occur ubiquitously in drift wave turbulence, are thought to be an important component in the search for an explanation of the so-called H-mode, a special plasma state leading to higher energy confinement. Explanations usually stress the flows' eddy-shearing properties with high flow shear leading to a tearing apart of radially moving turbulent structures, ultimately reducing turbulent transport (and thus radial heat flux), thereby increasing energy confinement time. This is of major importance for economical operation scenarios of future commercial fusion reactors, whether they might be tokamak or stellarator-based.

In Section 5.1, the fundamental ideas behind zonal flows are introduced.

Since this work seeks to analyze drift wave based zonal flows, Section 5.2 deals with the self-interaction properties of turbulent drift wave vortices, introducing the concept of Reynolds stresses. These stresses are capable of feeding (or destroying) the zonal flows, providing the all-important link between drift waves and flows. Furthermore, turbulent transport [25] and drift wave propagation under the influence of a shear flow are derived, explaining a vital asymmetry in drift wave-related flow behavior between the negative and positive flow regimes.

Consequently, Section 5.3 concerns itself with the change in zonal flow strength due to drift wave self-focusing, introducing a drift wave action invariant. The main goal of this section is to determine the conditions under which growth of zonal flows occurs. Finally, the subsequent retroaction of the flow on the drift waves is discussed.

With the complex zonal flow drift wave interactions examined, Section 5.4 explains the parameter studies undertaken within this drift wave zonal flow regime, motivating the significance of the single dimensionless parameter $\hat{\rho}_s$, including two regimes separated by

a $\hat{\rho}_s$-threshold: The zonal flow regime for high values of $\hat{\rho}_s$ - where the first examples of Hasegawa-Wakatani-based zonal flows are realized for $\hat{\rho}_s \gtrsim 0.15 - 0.20$ - as well as a purely turbulent regime for values below. An analytical model for the zonal flow regime transition is reached through a balance of a $\hat{\rho}_s$-dependent resonance gradient derived via a mixing length argument and the shear flow gradient, leading to either one of the two possible Reynolds stress asymmetries, with the high-$\hat{\rho}_s$ Reynolds stress being in favor of zonal flow generation.
These findings, together with Chapter 4 - especially so the two transport scales described in Section 4.4 - will form the basis for the bifurcation-related zonal flow parameter studies undertaken in Chapter 6.

5.1 Basic concept

Zonal flows are linearly stable poloidal $\vec{E} \times \vec{B}$-flows, denoting poloidal and toroidal mode numbers equaling zero. They are introduced comprehensively in [11]. Zonal flows require radial potential gradient flux surface averages (as in Figure 5.1), meaning that between any given flux-surface (any poloidal-toroidal plane spanned by $\vec{j}$ and $\vec{B}$), there needs to be a mean electric field oriented in the x-direction. Usually, zonal flows appear radially nested, with alternating positive - those in the electron diamagnetic drift direction - and negative flows.
Zonal flows ultimately gain their energy from gradients [93], mediated via turbulence - or more specifically, in the case of the system analyzed in this work, via drift wave turbulence. Turbulence and flows balance each other, although their relationship seems to be more complex than the often-cited predator-prey-model implies [54].
It is important to note that while zonal flows only occur naturally within nonadiabatic surroundings (since adiabatic drift waves cannot grow to achieve nonlinearity on their own), it is possible to create purely adiabatic zonal flows by prescribing extremely high initial perturbations. The resulting zonal flows exhibit very high frequencies and symmetric patterns [11].

There is a second, more common set of zonal flows, non-stationary modes which periodically change their direction. These geodesic acoustic modes couple to sound waves and follow the curvature of the magnetic field lines until their compression in the inner high-field region of e.g. a tokamak forces them to revert their direction, leading to oscillatory behavior. In toroidal geometry, and omitting the essential parallel balance flows, zonal flows only become possible when geodesic acoustic modes go full circle.
Since this work focuses itself on slab geometries, geodesic acoustic modes [27] will not be examined in any more detail. More information about the state of research on geodesic acoustic modes can instead be found in [94].

Zonal flows can most easily be identified by performing a radial (x-direction) Fourier transformation of v_y, localizing the highest-amplitude wavenumber.

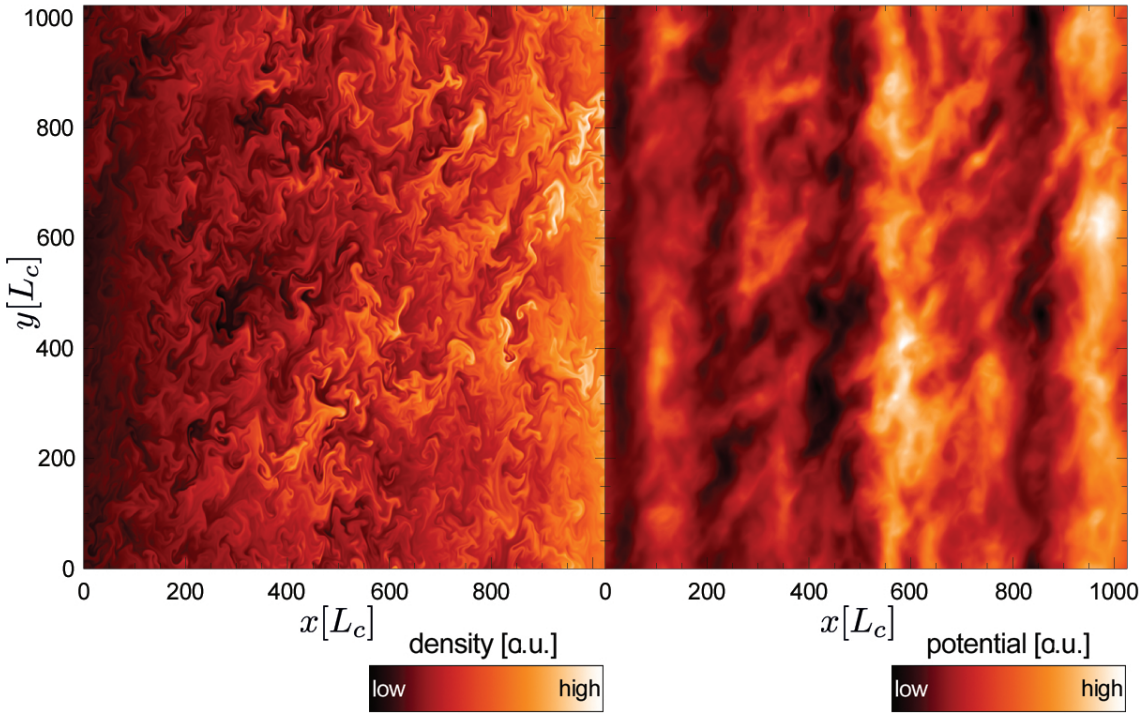

Figure 5.1: Density corrugations and electrostatic potential are plotted in extremely high resolution in the radial-poloidal x-y-plane for weak emerging zonal flows. While the poloidal flows are easily recognizable in the potential on the right hand side, their effects on the density on the left hand side are rather subtle - shearing has just begun.

5.2 Drift wave self-interaction

Drift waves appear as localized wave packets, superpositions of waves within an usually Gaussian range of wavenumbers k. For nonzero gyroradii, different drift wave wavenumbers interact with each other nonlinearly, leading to a number of crucial phenomena.

5.2.1 Reynolds stresses

Reynolds stresses are what feeds the zonal flows [38]. The Reynolds stress tensor is mathematically derived by averaging over the Navier-Stokes equations in a turbulent fluid, taking account of the fluctuations in the fluid momentum. It is defined as

$$\partial_t \langle v_y(x) \rangle = -\partial_x \langle \tilde{v}_x \tilde{v}_y \rangle_{y,z} \tag{5.1}$$

where $\langle \rangle_{y,z}$ denotes averaging over y and z, a magnetic surface [70].
Now, $\langle \tilde{v}_x \tilde{v}_y \rangle_{y,z}$ marks the y-z-averaged flux of turbulent y-momentum in x-direction and vice versa (it has to be symmetric due to its nonexistent rotation) - and thus the x-y-component Π_{xy} of the Reynolds stress Π, since

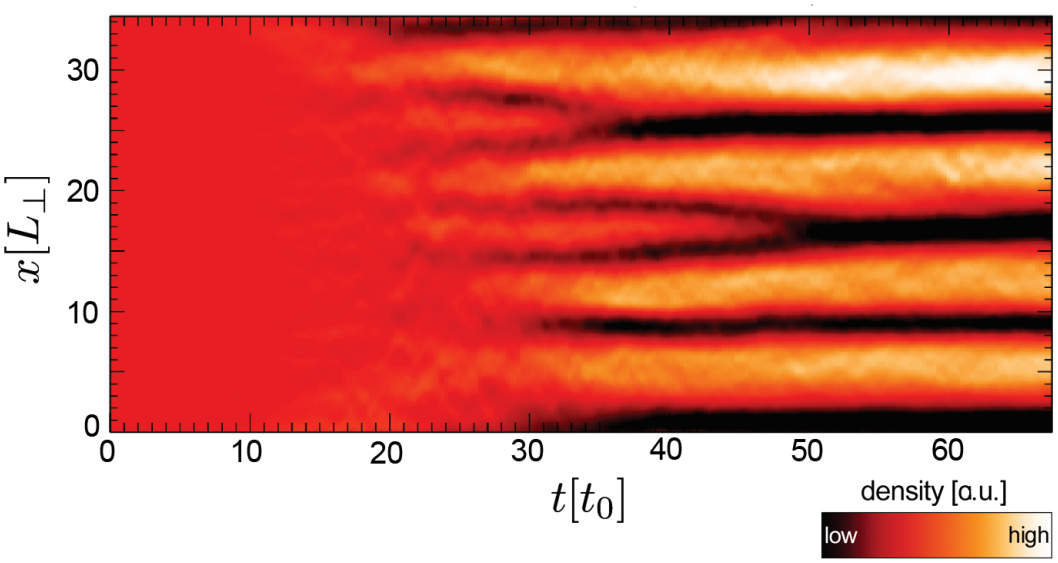

Figure 5.2: Development of a typical zonal flow for $\hat{\rho}_s$ over time (in units of t_0), pictured versus radius in units of $L_\perp$: In the beginning, while the initial drift wave amplitude start to grow from low levels, no poloidal shear flow activity can be seen. Later, the drift waves turn nonlinear and develop into full-blown turbulence, yielding chaotic flows through local Reynolds stresses. These flows finally align into the heavily structured large-scale flows commonly referred to as zonal flows. In the case of ITG modes[75], these satisfy a constant intrinsically determined wavelength condition.

$$\Pi_{xy} = \langle (-\partial_y \phi)\, (\partial_x \phi) \rangle \tag{5.2}$$

where $-\partial_y \phi$ and $\partial_x \phi$ can be identified with the x- and y-components of the $\vec{E} \times \vec{B}$-velocities, with the finite flux surface average of $\left(\vec{E} \times \vec{B}\right)_{poloidal}$ signifying the zonal flow velocity

$$v_{ZF} = v_y(x) \equiv \langle \partial_x \phi \rangle_{y,z} \tag{5.3}$$

Of course, Galilean invariance is upheld. For large-scale flows (large when compared to the turbulence length scale), this implies that the Reynolds stress may only depend on the shearing rate leading to a derivative of the poloidal flow as in

$$\partial_t v_y(x) = -\partial_x \Pi_{xy}(v_y') = -\Pi'_{xy}(v_y') v_y'' \tag{5.4}$$

being influenced by its own second radial derivative as well as the radial derivative of the Reynolds stress.

In order to interpret Reynolds stresses graphically, it is useful to consider a number of simple cases. Imagine f.e. y-momentum moving in the x-direction, weakening on its way radially outward. According to (5.1), the right hand side is positive, and $\langle v_y \rangle$ must thus increase over time - implying that wave components which start to drift later are stronger. Equivalently, a reduction of v_x in x-direction implies compensation by an increase in $\langle v_y \rangle$ (via $\partial_t \langle v_y \rangle > 0$), because density continuity could otherwise not be upheld. In the eddy-picture, shear flow is enhanced by vortex peeling [78], yielding nonlinear instability by breaking up the eddies and feeding their v-components into the respective flows.

Consequently, the momentum conveyed by the turbulent Reynolds stress plummets into the zonal flows, fueling them (since the Reynolds stresses are aligned parallelly to the flow shear) with accumulated drift wave energy, allowing the flow amplitudes to ultimately exceed the drift wave amplitudes by far. As will be seen in Subsection 5.2.2, the flows act much like the resonant surfaces discussed in Section 4.3, reflecting the drift wave velocity component orthogonal to the zonal flow direction and absorbing the parallel component (only yielding nonzero mean values for anisotropies within the turbulence), equivalent to a large-scale ocean wave driven by the wind. This conveying of momentum and energy from drift waves into the zonal flows leads to their increasing self-focusing - without it, only mean $\vec{E} \times \vec{B}$-, but no zonal flows could exist - a growth which only stops once it becomes balanced by nonlinear and collisional flow damping.

5.2.2 Drift wave propagation and self-focusing

Drift waves propagate radially according to (4.5), or more precisely

$$v_{gr,x,cold} = \frac{\partial \omega}{\partial k_x} = \frac{-2k_x k_y \rho_s^2}{\left[1 + \rho_s^2 (k_x^2 + k_y^2)\right]^2} \, (+hot) \tag{5.5}$$

But because of the introduction of zonal flows into the picture, the radial wavenumber $k_r = k_x$ now becomes shear-flow-dependent (it is important to note that k_y remains unchanged due to translational invariance in the poloidal direction) as seen in [47]

$$k_x = k_{x_0} - \frac{\partial v_y}{\partial x} t |k_y| \tag{5.6}$$

where v_y marks the poloidal shear flow[1].

In the limit where $\left(k_x^2 + k_y^2\right) \hat{\rho}_s^2 \ll 1$ this yields a radial group velocity of

$$v_{gr,x} \approx -2k_{x_0} k_y \hat{\rho}_s^2 + 2v_y' t k_y^2 \hat{\rho}_s^2 \tag{5.7}$$

[1] Additional effects arise if this assumption breaks down. However, such a scenario would be dominated by physically irrelevant short wavelength flows.

By changing the radial drift wave wavenumber k_x (with k_y remaining constant), zonal flows act like force fields. Since $\dot{v}_{gr,x} \propto +v_y'$ there is a sign change at the positive flows (those in the electron diamagnetic drift direction) from plus to minus not only of the flow shear v_y', but also of the time derivative of the radial group velocity.
As seen in Figure 5.3, this has grave implications, as it implies drift wave propagation in the positive radial direction for positive flow shear and vice versa propagation in the negative radial direction for negative flow shear. Thus, zonal flow maxima attract drift waves while zonal flow minima repulse them. Since this work is concerned with turbulent systems, this result is equivalent to claiming that negative flows (those in the ion diamagnetic drift direction) repulse the turbulence, comparable to the resonant surfaces covered in Chapter 4.
Modes with insufficient k_{x_0} cannot even penetrate these flow minima, but remain trapped in an oscillating motion around the flow maxima. Drift waves thus can get stuck in the zonal flows if only their $v_{gr,x}$ is small enough.

There is an obvious caveat in the basic picture. Drift waves originating at the negative flows are driven through an area of high flow shear around the zero crossing of v_y. There, according to (5.6), $|k_x|$ increases strongly. But now, the extra term in the denominator in (5.7) becomes non-negligible and the limit $\left(k_x^2 + k_y^2\right)\hat{\rho}_s^2 \ll 1$ breaks down, yielding instead the following orthogonal relation for high enough $|k_x|$:

$$v_{gr,x} \approx -\frac{2k_{x_0}k_y}{\hat{\rho}_s^2\left(k_x^2+k_y^2\right)^2} + \frac{2v_y' t k_y^2}{\hat{\rho}_s^2\left(k_x^2+k_y^2\right)^2} \tag{5.8}$$

so that $|v_{gr,x}| \to 0$, resulting in the drift waves becoming stuck in steep zonal flow gradients.

This results in two essential insights: Firstly, negative zonal flows (those opposite to the electron diamagnetic drift direction) repulse the drift wave turbulence, while positive zonal flows serve as attractors, leading to a self-focusing behavior of drift waves. Secondly, very high flow shear is able to slow down the drift waves to the point of immobilization, preventing them from reaching the zonal flow maxima.

5.3 Drift wave impact on zonal flows

The implications of these concepts for zonal flows are profound. As discussed in the previous section, drift wave propagation is intrinsically linked to Reynolds stresses $\langle \tilde{v}_x \tilde{v}_y \rangle_{y,z}$, exercising a significant influence on the zonal flows themselves.
A measure for the increase of zonal flow strength due to drift wave self-focusing is the intensity of the drift wave action invariant $N(\vec{x}, \vec{k})$ [95, 11], a conserved quantity of the drift wave - drift wave interaction which, for drift waves, equals

$$N_k = \left(1+k^2\right)^2 |\phi_k|^2 \tag{5.9}$$

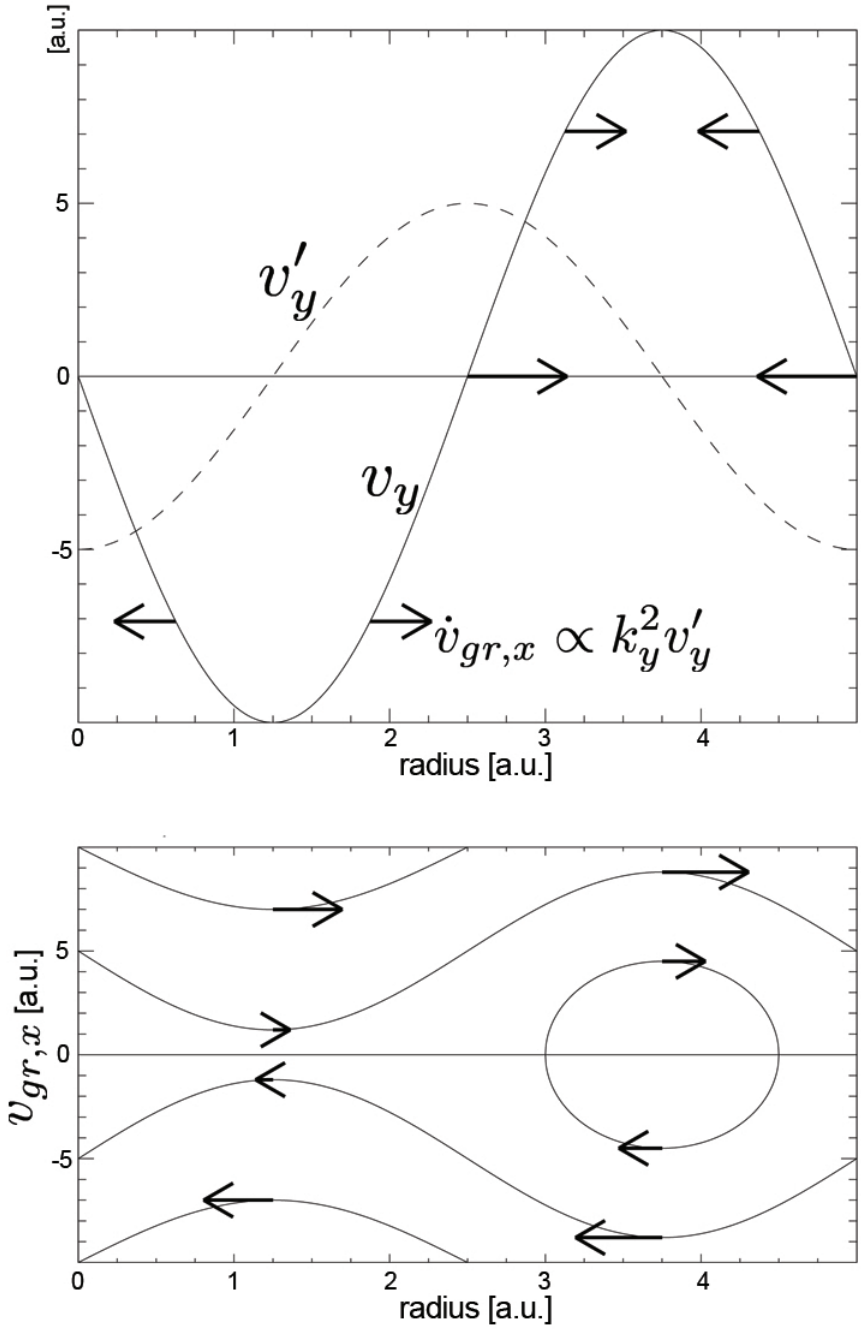

Figure 5.3: At the top, a sinusoidal shear flow v_y (with $v'_y = \partial_t v_y$) is plotted versus radius. Taking the derivative of (5.7) yields $\dot{v}_{gr,x} \approx 2v'_y k_y^2 \hat{\rho}_s^2 \propto k_y^2 v'_y$, marked by arrows. Thus, the drift wave group velocity is found to be repulsed by the negative flows ($v_y < 0$) and attracted by the positive ones. The second part contains the drift wave phase space plot, with radial position aligned along the x-axis and group velocity along the y-axis.

the time derivative of which can generally be defined as

$$\partial_t N_{\vec{k}} = -\nabla_{\vec{x}} \left(N_{\vec{k}} \cdot \vec{v}_{gr,\vec{k}} \right) - \nabla_{\vec{k}} \left(N_{\vec{k}}(x) \cdot \dot{\vec{k}}(\vec{x}, \vec{k}) \right) \tag{5.10}$$

yielding the amplitude of drift wave attraction or repulsion, with the only assumption going into (5.10) that it can be described as a wave packet. The first term on the right marks the convergence of a wave packet due to $\vec{v}_{gr}$ while the second term needs to be introduced due to the k-changing effect of shear flows, shearing apart wave packets. It describes the divergence of a flux in the direction of the $\vec{k}$-wavenumber, which enables it to influence radial wavenumbers of wave packets - while Reynolds stresses merely influence the flow.

It can be shown [20] that

$$\dot{\vec{k}} = -\vec{\nabla}_x \vec{v} \cdot \vec{k}_0 = -\vec{\nabla}_x \omega \left(\vec{k}, \vec{x} \right) \tag{5.11}$$

a result which can be compared to the Fourier-transformed force equation in quantum mechanics, where the negative gradient of the energy (specified by the frequency) corresponds to the underlying force, a change in momentum. For drift waves as well as in quantum mechanics, a force field changes the frequency of a wave, with the only condition necessary for $E(\vec{k})/\omega(\vec{k}) = N_k/2 = const.$ being semi-adiabatic behavior so that the shearing occurs slowly in comparison with the drift wave oscillation. (5.11) thus leads to

$$\partial_t N_{\vec{k}} = -\nabla_{\vec{x}} \left(N_{\vec{k}} \cdot \vec{v}_{gr,\vec{k}} \right) + \nabla_{\vec{k}} \left(N_{\vec{k}}(x) \cdot \vec{\nabla}_x (\vec{v}(\vec{x}) \cdot \vec{k}) \right) \tag{5.12}$$

$$= -\nabla_{\vec{x}} \left(N_{\vec{k}} \cdot \vec{v}_{gr,\vec{k}} \right) + k_y \left(\partial_x v_y \right) \left(\partial_{k_x} N \right) \tag{5.13}$$

where the second equivalence is only valid for drift waves with strictly poloidal zonal flows for which

$$-\vec{\nabla}_x \omega \left(\vec{k}, \vec{x} \right) = -\hat{\vec{x}} \partial_x \vec{v}_y \cdot \vec{k}_y \tag{5.14}$$

with $\hat{\vec{x}}$ marking the unit vector in x-direction.

Now it is imperative to check which initial density distribution is capable of leading to a self-focusing solution. Since the drift wave frequency needs to decrease during the self-focusing process for it to put energy into the development of zonal flows, and since this frequency depends on the wavenumber k via the dispersion relation $\omega = \omega(\vec{k})$, the initial wave packet determines the properties of any drift wave self-focusing.
In the adiabatic case, (4.3) holds true, leading to $v_{gr,x} = -2k_x k_y/(1+k^2)^2$ [11] and thus

$$\langle v_x v_y \rangle = -\int N_k (1+k^2)^{-2} k_x k_y d^3k = \frac{1}{2}\int N_k v_{gr,x} d^3k \tag{5.15}$$

Utilizing the Reynolds stress relation as well as the first term of the drift wave action invariant (5.10) (the second gets eliminated due to the divergence in k-space),

$$\partial_t v_y = -\partial_x \langle v_x v_y \rangle = -\frac{1}{2}\int \partial_x N_k v_{gr,x} d^3k = \frac{1}{2}\int\int \partial_t N_k d^3k dy \tag{5.16}$$

leads to a simple relation between the change in zonal flows and the change of the integrated wavenumber density $\int\int (N_k - N_{k0})\, d^3k dy$ (where $k_0 = k, t = 0$)

$$v_y = v_{y0} + 2\int\int (N_k - N_{k0})\, d^3k dy \tag{5.17}$$

So the zonal flow velocity changes exactly alike the integrated wavenumber density.

5.3.1 Conditions for growth

The implications of these findings are not to be underestimated. With a common starting point being no zonal flows whatsoever ($v_y = 0$) and an initial localized distortion in N, this distortion tends to spread out while at the same time decreasing in peak strength. Subtracting the initial state from the final one yields a v_y-dip in the center and an increase in v_y further out. For periodic distortions in N, small periodic v_y-distortions with the same wavelength develop: Zonal flows.

Perturbation theory is applied to (5.13) in order to determine v_y in more detail:

$$\partial_t N_k = -v_{gr,x}\partial_x N_k + k_y v_y' \partial_{k_x} N_{k0} \tag{5.18}$$

A Fourier transformation yields

$$(-i\omega(k) + iqv_{gr,x})\, N_k = iqk_y v_y \partial_{k_x} N_{k0} \tag{5.19}$$

and thus

$$N_k = \frac{qk_y}{qv_{gr,x} - \omega}\partial_{k_x} N_{k0} v_y \tag{5.20}$$

where $q \neq k$ since q is the wavenumber in x-direction of the N_k-distortions and k marks the wavenumber in y-direction the drift waves

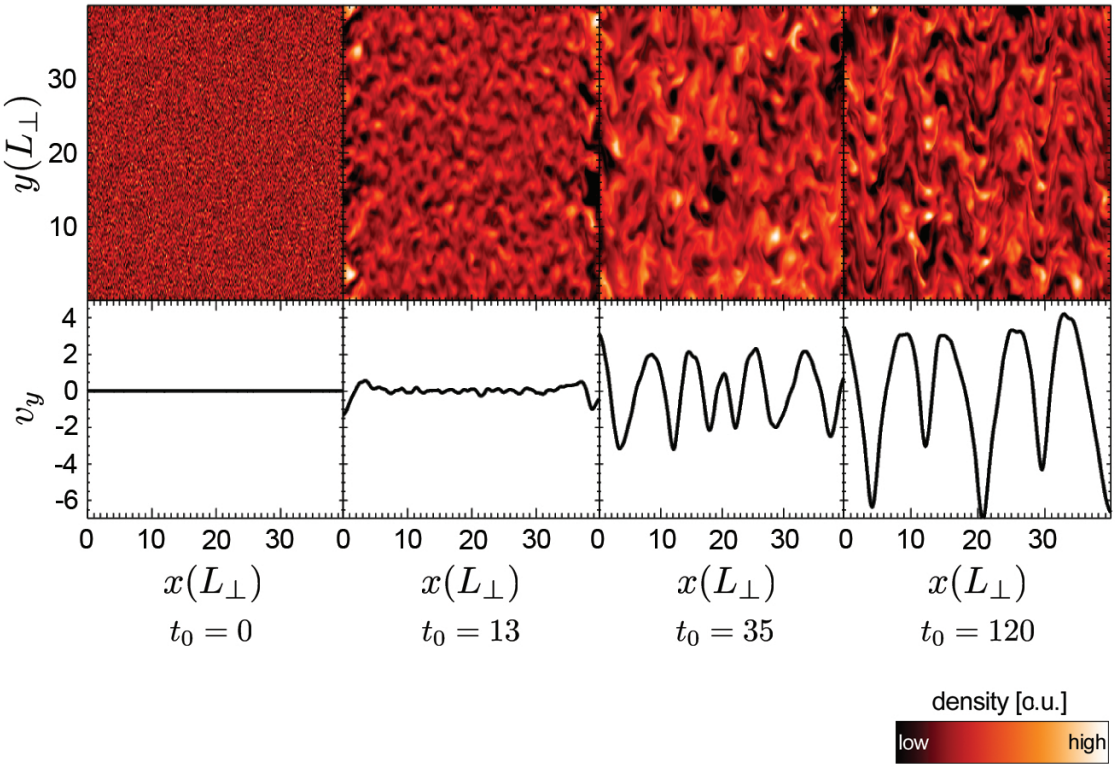

Figure 5.4: The density picture in the radial-poloidal plane is depicted in the upper row (in units of $L_\perp$), with the corresponding shear flows v_y plotted below. Initial small-scale seed fluctuations at t_0 turn into full-blown drift wave turbulence ($t_0 = 13$), with a zonal flow pattern emerging ($t_0 = 35$) and finally saturating ($t_0 = 120$).

With $v_y = 2 \int \int N_k d^3k dy$ from (5.17), this leads to

$$v_y = 2 \int \int \frac{q k_y}{v_{gr,x} q - \omega} \partial_{k_x} N_{k0} d^3k dy v_y \tag{5.21}$$

Around $v_{gr,x} = \omega/q$, a resonance occurs, meaning that drift waves drifting at approximately this velocity have the largest influence on zonal flow growth.

Taylor expansion to first order, followed by partial integration replacing the drift wave $\omega(k)$ with the k-independent zonal flow Ω^2, retains only the second term and thus

$$v_y = -\frac{2q}{\Omega^2} \int \int k_y v_{gr,x} \partial_{k_x} N_{k0} d^3k dy v_y = -\chi \frac{2q}{\Omega^2} v_y \tag{5.22}$$

[2]For this, $q k_y/(v_{gr,x} q - \omega) \approx -q k_y/\Omega(1 + v_{gr,x} q/\Omega)$.

For $\chi < 0$, ω becomes real, leading to oscillatory behavior of v_y. For $\chi > 0$, however, ω becomes imaginary and zonal flow growth becomes possible.

But is $\chi > 0$? With

$$v_{gr,x} = -2k_x k_y / \left(1 + k^2\right)^2 \tag{5.23}$$

the integrand in χ becomes

$$-2k_x k_y^2 / (1 + k^2)^2 \partial_{k_x} N_{k0} \tag{5.24}$$

Assuming symmetric initial N_{k0}, a positive peak in N_{k0} yields positive $\partial_{k_x} N_{k_x}$-values for $k_x < 0$ and negative ones for $k_x > 0$. Multiplying this with $-k_x$ provides an entirely positive function with two peaks, thus yielding $\chi > 0$ - while an initial dip in N_{k0} leads to $\chi < 0$.
Accordingly, initial positive distortions in N_{k0} are capable of leading to zonal flow growth.

Inserting $v_{gr,x}$ into (5.22) yields the zonal flow wavenumbers [20], while a rough long-term estimate based on the ansatz $D_t \int \int N_k = 0$ for a drift wave 'quantum' with $c_s = v_{gr,x}$ (drift waves at $T = 0$ are monochromatic) produces a theoretical zonal flow wavelength expectation of

$$\lambda \approx 2qk_y \sqrt{\int \int N_{k0} d^3k dy} = 2qk_y \sqrt{Ek_y/\Omega} \tag{5.25}$$

In reality, for drift waves the exact zonal flow wavelength has been found to depend on the past history of the system[3], down to the gyroradius scale (since flows with smaller wavelengths grow faster) if high-frequency high-amplitude random noise is prescribed. Any large-scale artificial initial flow pattern will stay at the same λ and grow into a saw-tooth pattern with a rectangular shearing rate function, as seen in Figure 5.5. However, if no dominant history is present, the zonal flows will behave similarly to the ITG case, with the same zonal flow λ emerging despite different initial n-distributions.
These resulting flow patterns (albeit not the only stable ones) will be of the order of the turbulent scale length ρ_s whenever zonal flows are formed from initial random noise, since larger flows are excited less strongly due to the radial derivative operator seen in (5.4) (smaller flows are prevented due to Larmor radius effects).

Zonal flow amplitude, on the other hand, is determined by the nonlinear saturation process in combination with the amount of flow generated through Reynolds stresses in a given time frame. Since the drift wave system's nonlinear interaction is concentrated in the vorticity

[3]For ITG modes on the other hand, the zonal flow wavelength is prescribed naturally [75]: The same zonal flow pattern will always emerge no matter the initial n- or N-distribution.

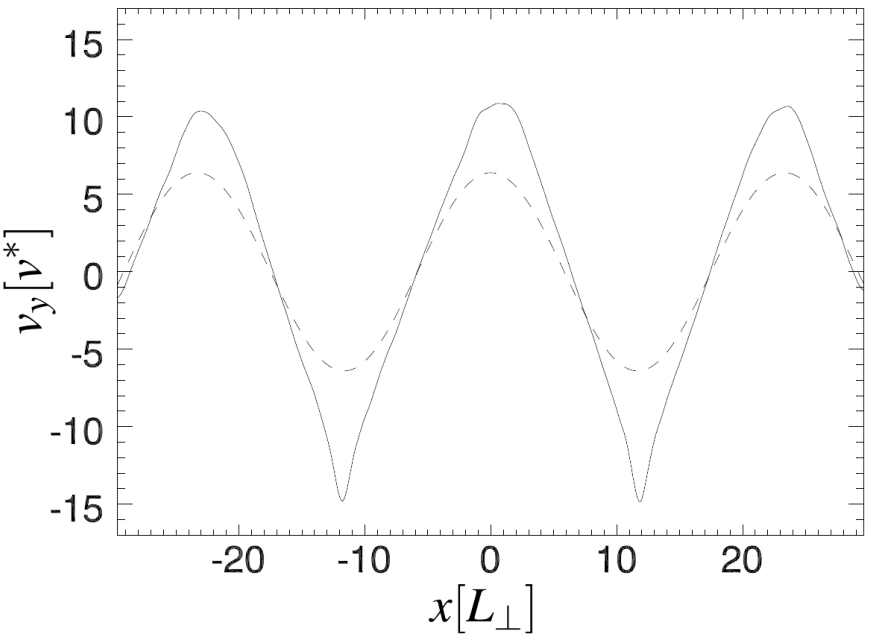

Figure 5.5: An artificially prescribed poloidal flow is plotted versus radius. The initial flow pattern is marked by the dotted line, while the continuous line signifies the final steady state. As can easily be seen, the artificial flow wavelength remains stable. Flow shear grows until a maximum value is reached, with an asymmetry in behavior when the positive and negative flow peaks are compared. The latter features will be explained in more detail in Chapter 6.

equation, which increases proportionally to the level of nonadiabaticity (a variable that is capped at moderate values in this work), only moderate zonal flow amplitudes can be reached. In addition, due to the inherently medium-to-high wavenumbers of the associated nonadiabatic sheared drift wave modes, some of the interaction is concentrated in drift wave - drift wave events, tearing apart the eddies rather than fueling the flows.
More specifically, the zonal flow shearing rate can be equated with the turbulent drift wave growth rate since the radial derivative of any velocity is nothing but a frequency. According to the Waltz criterion (described in [11], among others), for every drift wave mode with its growth rate γ there exists a shearing rate against which the drift wave growth rate cannot prevail, resulting in a dampening of the drift waves. This basically comes down to a condition for the flow shear level necessary for suppression of all drift wave turbulence, which of course concurs with the maximal flow shear possible since the existence of drift wave turbulence is required for shear flow growth mediated by Reynolds stresses[4].

[4]Of course, this is merely an order-of-magnitude-argument. Shear flows may even exceed this apparent boundary through secondary effects when the drift wave mode characteristics are changed significantly, e.g. for extremely small drift wave k_y and high $k_\parallel$. On the other hand, if the drift wave k_x becomes too high in comparison with k_y and the gyroradius, only negative Reynolds stresses can be caused by the turbulence, transferring energy from the flows into the drift waves, exceeding both shear flow and resonant

Here, the final positive and negative flow shearing rate plateaus following from the saw-tooth-shaped large-scale flows presented in Figure 5.5 correspond to zero Reynolds stress. The flow pattern is stable for $\Pi'_{xy} > 0$ at the location of the maxima and $-\Pi'_{xy} > 0$ around the minima - as discussed in Subsection 5.4.3 - while it can be excited from an initial noise distribution for $\Pi'_{xy}(v_y = 0) < 0$.

5.3.2 Zonal flow feedback

It has been shown in Chapter 4 that the direct drift wave - drift wave interaction is too weak (even more so for adiabatic drift waves) to actuate scattering to high wavenumbers. As another source for this process, zonal flows have been proposed. Accepting the paradigm of a predator-prey model, the zonal flows are fueled by drift waves via Reynolds stresses (which in turn are required to lose energy), while at the same time shearing the drift wave eddies apart [23], serving as predators to their prey [52].
However, recalling that reflection at resonant surfaces serves as the main source of drift wave growth, and since zonal flows provide a similar amplification through reflection, some doubt is cast concerning this picture. Furthermore, the drift wave modes trapped - fiber optics-like - within the positive flows have been verified numerically to exhibit overproportionally high amplitudes, as shall be seen in Chapter 6, especially so in Figure 6.1, resembling trapped prey thriving in close proximity to its predator as well as reproducing strongly in the high-shear regions in between.
Further evidence gained via NLET also suggests that the predator-prey model falls short of its expectations in reality, with the observed behavior being more complex. Neither does drift wave turbulence under all circumstances fuel the zonal flows, nor does a rise of zonal flows necessitate a drop in drift wave turbulence intensity: More often than not, the fluctuations in the level of the prey are not caused by the predator.
If anything, a predator bifurcation arises, with one type (the negative flows) expelling the prey, and the other (the positive flows) harboring it.

5.4 Zonal flow regime

5.4.1 Numerical parameters

The zonal flow studies presented in this work have been carried out only after external distortion factors could be excluded. Most importantly, the issues discussed at the end of Chapter 4 - (artificial) hyperviscosities, the Courant effect and Alfvén waves - as well as parallel velocity effects had to be prevented.
Artificial background flows posed an additional problem. These could not be eliminated completely, as they were instrumental in preventing small-scale artificial fluctuations, but they needed to be reduced to such an extent that they did not influence the actual flows. A viable balance has been reached where these flows are not only constant in the radial

surface potential effects discussed in Subsection 5.4.3. This can already occur far below the actual shear flow maximum threshold.

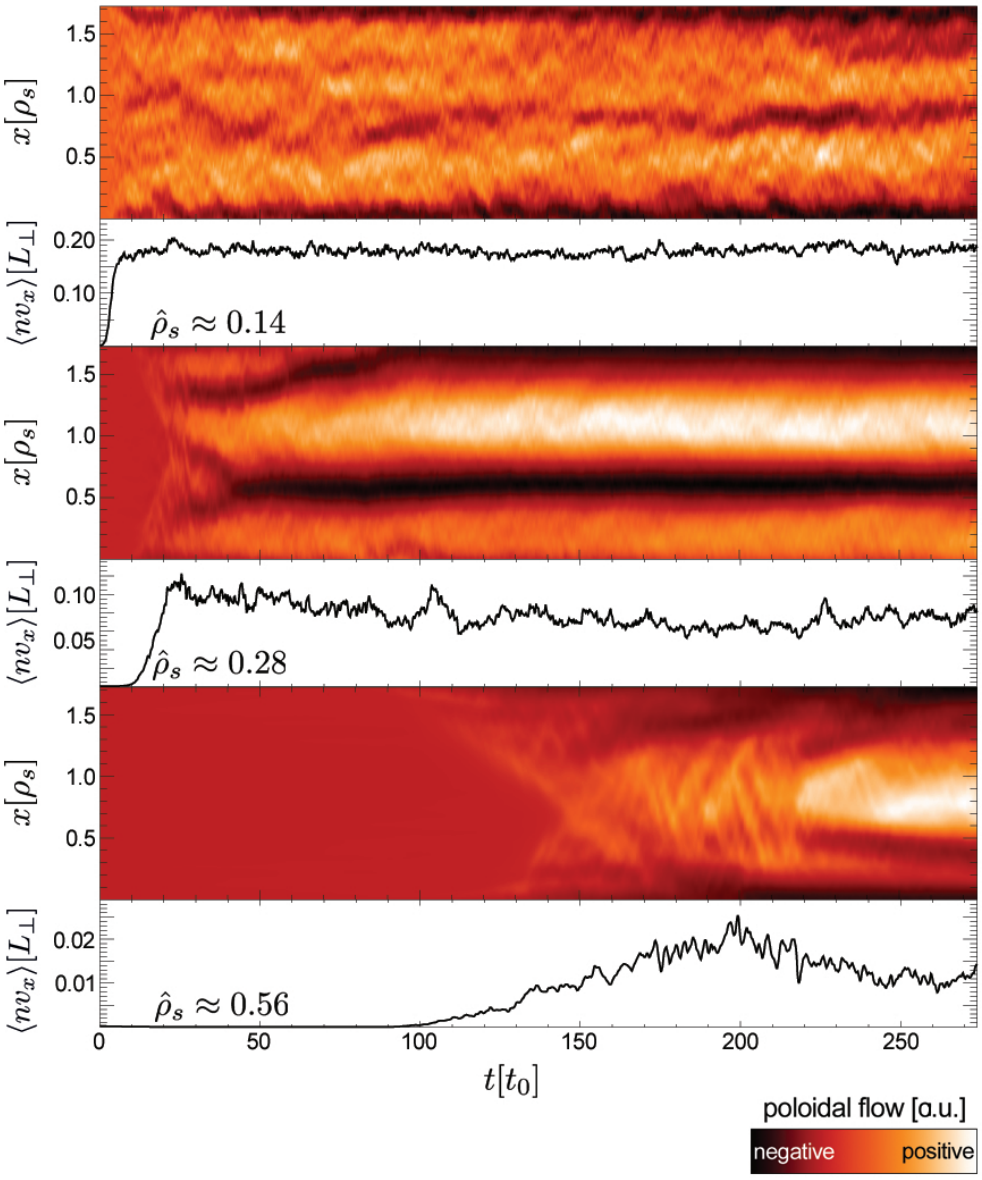

Figure 5.6: For three different values of $\hat{\rho}_s$, poloidal flow is plotted versus radius (in units of ρ_s) and time (normalized to t_0), together with the concurrent density flux averaged over the entire domain. Exponential growth occurs after the onset of drift wave turbulence at around $t_{0,onset} \approx (\hat{\rho}_s/0.14)^{3.5}$. Nonlinear saturation kicks in after $t_0 \approx 2t_{0,onset}$, accompanied by an initial overshoot in the density flux during the chaotic flow phase. Density levels finally settle down into a stable, barely irregular state after full zonal flows emerge at around $t_0 \approx 3t_{0,onset}$ (with mere transitional flows achievable for $\hat{\rho}_s \approx 0.14$). Flow development advances according to the $\hat{\rho}_s^{3.5}$-proportionality (see (6.3)), with a $\hat{\rho}_s^{-2.0}$-proportionality for the density flux amplitude in the zonal flow regime as shown in (4.49).

direction (and thus without direct influence on the drift wave turbulence) but also smaller than the physical flows by around two orders of magnitude, yielding excellent convergence. Border effects proved devastating at first, but they were finally suppressed by implementing two small stripes at the rims where density was held constant for the entire duration of the run, preventing the accumulation of artificial drift waves enhancing the flows. Optimizing this procedure, only the outer 2-5% on each side had to be discarded from the final results.

While all of these issues had to be handled, retaining tightly tweaked parameters proved crucial in order to prevent disproportionate resource consumption levels. Typical computation times for high-$\hat{\rho}_s$-runs with resolutions of $n_{x,y} \geq 256$ and $n_z \geq 64$[5] leveled out to around 24 hours on 128 to 256 processors. All of the consistency and convergence scans performed - where parallel velocities, artificial (hyper)viscosities, system sizes, resolutions and the likes were tested thoroughly - had in between the parameters (all in the dimensionless units derived in Chapter 3) shown in Table 5.1, close to their respective computational sweet spot, being physically sound[6], yet not too time-consuming.

Table 5.1: Numerical run parameters

radial-poloidal resolution	$n_x = n_y = 64 - 512$
toroidal resolution	$n_z = 16 - 128$
radial-poloidal system size	$L_x = L_y = 3 - 64$
toroidal system size	$L_z = 0.5 - 8$
grid step	$1.9 \cdot 10^{-3} - 3.1 \cdot 10^{-2}$
time step	$2.1 \cdot 10^{-5} - 3.4 \cdot 10^{-2}$
run time	$8.8 \cdot 10^{1} - 1.2 \cdot 10^{3}$

After assuring that physical accuracy could be provided, and sufficiently large domains could be described, the effect of the three main parameters in (3.37) and (3.38), the drift wave velocity α_d, the length scale parameter ϵ_n and the shear s, was examined. One of the most important findings during these runs was that that the dimensionless parameter $\hat{\rho}_s$ from (3.18) in (4.9) and (4.10), replacing α_d, ϵ_n and s in (3.37) and (3.38), could indeed be verified empirically to be the only parameter determining the evolution of the zonal flows - as it had been shown for the transport levels as well.

5.4.2 Regime transition

Zonal flows do not occur for all values of $\hat{\rho}_s$. While in theory there is no reason why zonal flows should not exist for very high $\hat{\rho}_s$, in reality this is hardly achievable due to their slow development in this regime, and, even more pressing, the need for higher resolutions (as discussed in Chapter 4). Thus, the already long-scale simulations quickly become

[5] The characteristics in the z-direction have been found to have little impact on the zonal flow structure, yielding a potential for economization which is utilized in Chapter 6.

[6] E.g., λ_{ZF} has been invariant under these resolutions with a maximum mean value departure of 3%.

uneconomical to carry out beyond $\hat{\rho}_s > 0.5 - 0.8$ (as will also been in (6.3)).

For small $\hat{\rho}_s$ however, the picture is different: As can be seen in Figure 5.6, no zonal flows occur until a relatively sharp boundary at around $\hat{\rho}_s \approx 0.15 - 0.20$ is reached. This limit coincides very well with transition between the two transport regimes dominated by the ρ_s and $L_\perp$ length scales respectively (see Section 4.4). The regime where $\hat{\rho}_s \gtrsim 0.15 - 0.20$ - the only regime where stationary, regular zonal flows develop deterministically - correlates with ρ_s being the dominant length scale.
This behavior can be motivated by noting that higher $\hat{\rho}_s$ causes more adiabatic[7] behavior with next to no shift between n and ϕ in (4.9) and (4.10) remaining, and thus with the effective $k_\parallel$ of the relevant drift wave modes increasing (while increasing $k_\perp$ yields more nonadiabatic behavior instead). But increasingly adiabatic circumstances correlate with decreased nonlinearity, implying a rather weakly nonlinear system - such as it occurs within the well-structured zonal flow regime. Of course, a certain level of nonadiabaticity is still required for zonal flows to develop in the first place, implying that zonal flows progressively abate for high $\hat{\rho}_s$ - albeit for values far beyond $\hat{\rho}_s \approx 0.5 - 0.8$. However, this is insufficient to explain the rather sharp transition occurring around $\hat{\rho}_s \approx 0.15 - 0.20$.

Zonal flow amplification (as discussed in Subsection 5.3.1) of high-$\hat{\rho}_s$-flows appears to follow straightforwardly from the forces on drift waves discussed in (5.7) in combination with the flow response in (5.17) mediated by Reynolds stresses (5.1). It is the fundamentally different behavior of the low-$\hat{\rho}_s$-case with no flows which seems to have to be explained.

5.4.3 A balance of gradients

A more precise explanation of this transition is indeed possible (and is presented in [91]). After some deliberation, the most important puzzle piece has been found in the resonant surfaces, or, more generally, in resonances. As discussed in Section 4.3, resonances are defined as the radial position where $k_\parallel = 0$ - around which drift wave growth is maximized. Now, even finite-sized drift wave eddies feel a localized resonance, become reflected and experience growth for a certain amount of time. Every resonant surface can be associated with an approximate resonant surface potential based on a mixing length argument such as the one used in Subsection 4.4.2, with the typical drift wave eddy mixing length signifying the distance over which the resonant surface potential exerts a measureable effect on the drift waves, resulting in a frequency gradient length of the resonances. But the distance between two resonant surfaces depends on the gyroradius, increasing linearly with ρ_s (and thus with $\hat{\rho}_s$). A similar increase due to higher ρ_s occurs for the mixing length distance - thus reducing the resonant surface gradient as $\hat{\rho}_s$ grows.
Seeding drift waves at the location of the resonant surfaces causes symmetrical propagation away from the point of initialization, bringing about Reynolds stresses[8] (with different signs on both sides). However, this picture becomes asymmetric once a shear flow is added

[7] Adiabatic behavior also correlates with a decreased likelihood of Kelvin-Helmholtz instabilities which are far more common for low-$\hat{\rho}_s$-drift waves or ballooning modes.

[8] These stresses are directly linked with the radial group velocity. The existence of $v_{gr,x}$ implies the

on top, effectuating an additional potential superposed on the resonant surface potential.

Two cases are possible. In the first one, the shear flow gradient remains smaller than the resonant surface gradient $\partial_x r_{ml}$ based on the radial resonance mixing length distance potential r_{ml}. The normal fishbone shape is distorted due to deceleration down the flow gradient (as they are drawn in the direction of the gradient) on the one side and acceleration on the other, but it remains qualitatively the same. The downhill modes experiencing deceleration while drifting away from the resonant surface spend more time in the vicinity of the resonance than the others, growing stronger in return (as seen on the left hand side of the top left graph in Figure 5.7[9], where the flow gradient is positive). Since the stronger-growing modes thus correlate with the ones moving downhill, and since they cause Reynolds stresses which weaken the shear flow translating the propagation asymmetry into a Reynolds stress asymmetry, no zonal flows can grow in this system. This case correlates with low values of $\hat{\rho}_s$, since low $\hat{\rho}_s$ implies high resonant surface gradients.
Increasing the shear flow or reducing the resonant surface gradient (so that the former triumphs over the latter) yields the second case, which behaves differently. Little fishbone propagation pattern similarity remains. Instead, the entire dynamics are dominated by the flow shear. Deceleration of the downhill modes leads to a standstill and subsequent reverse so that all modes (no matter how strongly they grow) end up moving in the direction of the gradient, causing Reynolds stresses which strengthen the flows, leading to dominant zonal flows. This cause correlates with low resonant surface gradients, and thus with high values of $\hat{\rho}_s$.

Empirically, the transition between these two regimes where both gradients are set equally strong on the downhill side (and thus oppositely directed)

$$\partial_x r_{ml}\left(\hat{\rho}_s\right) = -\partial_x v_y \tag{5.26}$$

has been found to be consistent with a value of $\hat{\rho}_s \approx 0.15 - 0.20$. Locally, the transitional value may vary since a smaller density gradient increases $\hat{\rho}_{s,local}$, enabling zonal flows to form within an otherwise hostile environment.

However, a third case is also conceivable. For low enough values of $\hat{\rho}_s$, even high artificially prescribed flow shears (up to the maximum as determined in Section 5.3) are insufficient to uphold these flows. For high enough $\hat{\rho}_s$, even small initial drift wave turbulence fluctuations will be sufficient to act as local flows for other drift waves, causing zonal flows to grow from nonlinear interaction between drift waves. But there might also be a transitional regime -

existence of some k_x (as well as k_y) which necessitates the presence of Reynolds stresses. These modes always drift in the direction into which the Reynolds stresses act.

[9] A more detailed analysis may arise from different choices of wavenumbers - a mixture of all modes has been examined, while the positive $k_\parallel$-modes are located on the one side and the negative ones on the other - and a consideration of the decreased lifetime of low-$\hat{\rho}_s$-modes. However, these drift wave mode characteristics are only statistically relevant for the comparison of the shearing rates and thus should not influence any of the large-scale results.

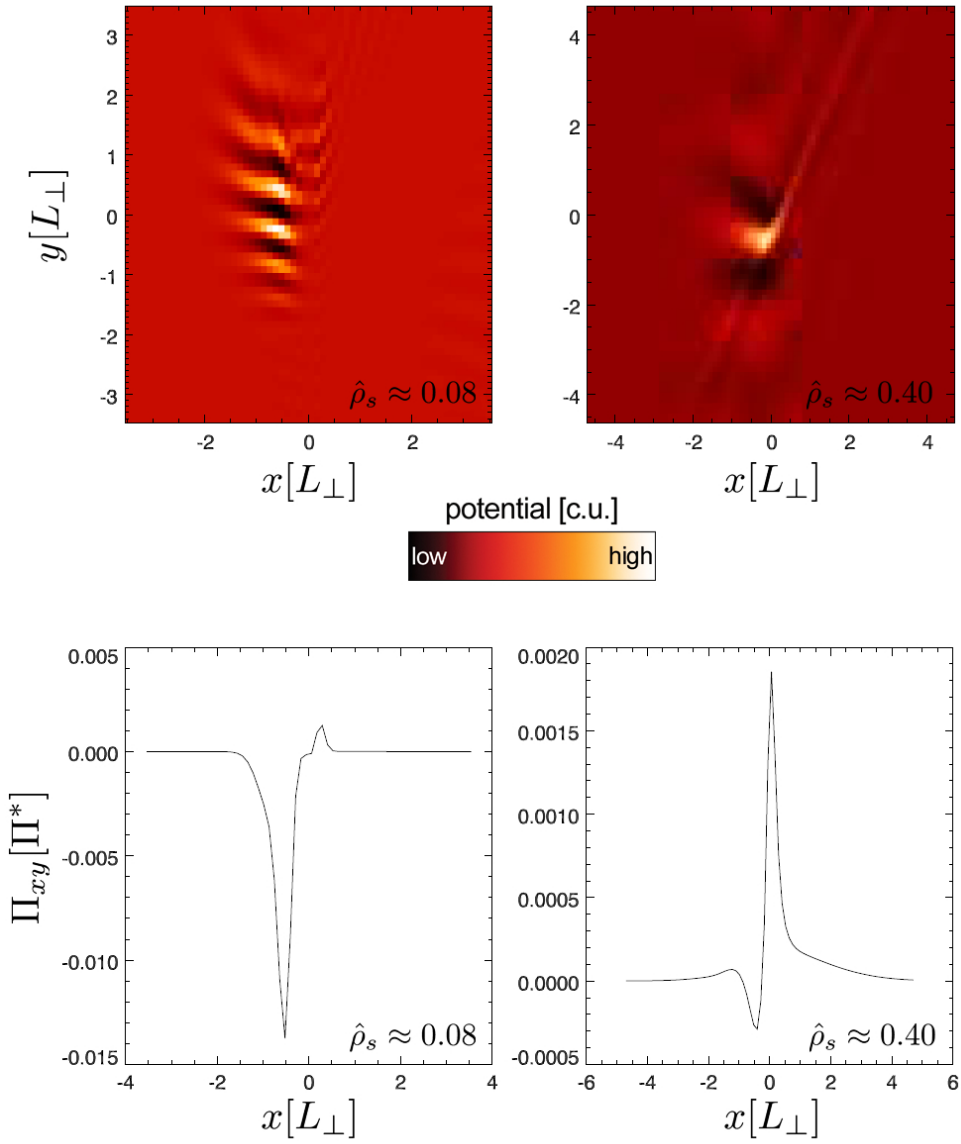

Figure 5.7: The same-time evolution of the radial-poloidal potential and the Reynolds stress (relative to the maximum particle flux) of linear drift wave modes initiated at the resonant surface $x(L_\perp) = 0$ in the presence of a positive flow shear $v_y' > 0$ is analyzed for $\hat{\rho}_s \approx 0.08$ and $\hat{\rho}_s \approx 0.40$ respectively. For low $\hat{\rho}_s$, the uphill acceleration only serves to decelerate the modes at negative radial positions, enabling them to grow stronger due to their vicinity to the resonant surface, causing pronounced negative Reynolds stress while moving downhill. For high $\hat{\rho}_s$, the resonant surface potential is much weaker in comparison to the shear flow potential, leading to uphill acceleration of all modes and thus positive Reynolds stresses, fueling the flows instead of dampening them - thus defining the zonal flow regime.

presumably somewhere below $\hat{\rho}_s \approx 0.15 - 0.20$ - where no zonal flows are able to emerge on their own (as the local shear flow potentials are insufficient to overcome the resonant surface potentials), but where an artificially prescribed zonal flow close to the maximum flow shear values will be able hold its ground against the resonances. This appears to indeed be the case, albeit with caveats: A sinusoidal flow artificially implanted into a low-$\hat{\rho}_s$-system (e.g. $\hat{\rho}_s \approx 0.115$) will degrade into a rectangular flow pattern, with the low-shear areas flattening while only the high-shear areas dominate over the resonant surface potential. This leads to increasingly edged domain walls in between, and thus second radial derivative effects causing the domain wall to move and consume the high-shear areas.

Chapter 6

Bifurcations

Building on the definitions and derivations of all previous Chapters, one of the core findings of this work is finally presented: A robust transport bifurcation, associated with density corrugations as well as asymmetric zonal flows. Bifurcations concerning the shear flow structure and the density gradient are of serious concern to fusion research, being capable of influencing radially outwards directed turbulent transport: Notably, the most important breakthrough in the last thirty years of fusion research has been the finding of the H-mode, caused by a bifurcation from the standard low-confinement edge gradient.

Due to the revelations within Sections 5.2 and 5.3, chiefly the difference in drift wave behavior between the vicinities of the negative and positive flows, the main focus of the numerical studies is put on the search for asymmetrical behavior within the zonal flow regime. And indeed, for the first time in self-sufficient numerical simulations of drift wave turbulence, a transport bifurcation associated with asymmetrical zonal flows and corrugated density gradients has been observed - developing self-consistently.

In Section 6.1, an extensive study of the bifurcations is realized. The robustness of these findings is thoroughly checked by both analytical and numerical means, followed by a parameter analysis comparing zonal flows at different values of $\hat{\rho}_s$. This examination is implemented for a wide array of parameters, including the flows' energy distribution, their spectra (with special focus on self-similar behavior), the strength of their bifurcations, their time scales of emergence and their correlation with drift wave intensity (as well as other drift wave parameters), while also highlighting the differences between the zonal flow regime and the low-$\hat{\rho}_s$-regime. In the end, the zonal flow dependencies on the parameter $\hat{\rho}_s$ are discussed.

Finally, in Section 6.2, a basic bifurcation mechanism is proposed, reproducing both the density corrugations and the flow asymmetry. A more detailed discussion delves into the finer sub-structure of both phenomena, before analyzing a promising-looking quantitative ansatz based on a chemical potential argument.

Section 6.3 deals with the only apparent contradiction within an otherwise sound set of explanations: Radial streaks in the density flux pattern, which - counterintuitively - propagate opposite to the flow gradient instead of exhibiting an uphill movement (as according

to Section 5.2). Following an extensive analysis of these streaks, dealing with their origin and their spectral propagation patterns under various parameters, four alternatives for their generation are proposed, leading to a viable explanation.

6.1 Transport bifurcation

Due to the observed asymmetry in the interaction between zonal flows and drift waves described in Section 5.2 - where the negative flows repulse the turbulence while the positive ones attract it - the focus of this work was put on a joint study of the development of the drift wave turbulence, the density gradient and the zonal flow structure. This decision has most certainly been worthwhile, with a major observation being achieved:

During the long saturation and stabilization phase of the zonal flows, an asymmetry was found to emerge within the flow pattern[1]. The negative flows - those opposite to the electron diamagnetic drift direction - were discovered to appear distinctively deeper than their counterparts, while the positive flows appeared flattened as well as broadened (the latter a necessary requirement of the former due to conservation of the flow mean: $\langle v_y \rangle = 0$) on top of the basic triangle wave pattern exhibiting the maximum flow shear as described in Subsection 5.3.1. Accordingly, the derivative of v_y was observed to become steepest for all radii r where $v_y(r) < 0$, surrounding the deepened negative flow peaks.
These unusual flow patterns were found to be linked to a severe change in the local density gradient. At the location of the negative flow peaks - the negative flow shear domain wall - the density gradient is increased strongly, while it is flattened in the entire rest of the domain, being centered around the positive flows. These density profile corrugations can be associated with two stable, distinctly different transport states, one - correlating with the positive flows - with high diffusivity and low gradients while the opposite occurs around the negative flows. Thus, a genuine transport bifurcation has been found at the flow shear domain walls, joining the ranks of a number of other bifurcations which were discovered under different conditions in the wake of L-H-transition research [55, 57, 59, 58, 60, 25].
A visual overview of these main features can be found in Figure 6.1.

6.1.1 Robustness of the stationary states

The combined phenomenon of flow asymmetry and density corrugations occurs consistently throughout an overwhelmingly large set of parameters, being extremely robust when disturbed under many different conditions. The fully converged runs have been performed with $n_{x,y} = 512$ and $L_{x,y} = 64$ (compare Table 5.1), varying ϵ_n between 0 and 0.48 (with $\hat{\rho}_s$ of up to 0.804, using $\alpha_d = 1.25$ and $s = 1$) and using the numerical parameters (as defined in Subsection 4.3.3) $\nu_4 = 1.e\text{-}7 - 5.e\text{-}6$, $\mu_{grid} = 0.09 - 0.12$ and $\alpha_{m_{add}} = 4.e\text{-}5 - 6.4e\text{-}4$.
Basically, whenever drift wave zonal flows are formed, they are accompanied by a noticeable asymmetry, most commonly with effect strengths around

[1] In earlier studies [25], asymmetries in the radial heat flux patterns had been observed.

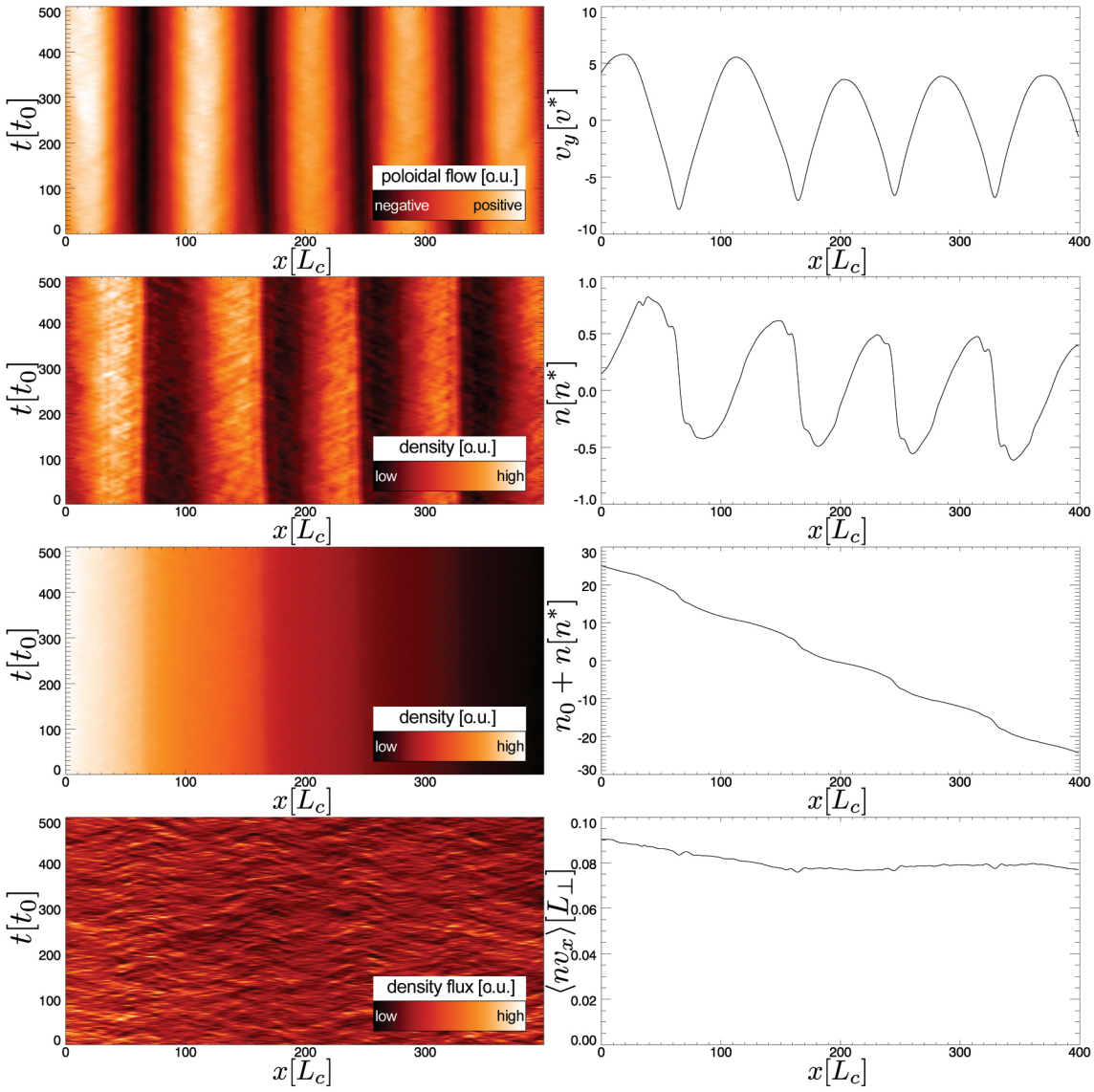

Figure 6.1: For $\hat{\rho}_s \approx 0.28$ (with $\epsilon_n = 0.06$, $\alpha_d = 1.25$ and $s = 1$), poloidal flow v_y, density corrugations n, the total density gradient $n_0 + n$ and the density flux nv_x are presented in a 2D plot yielding radius vs time (left hand side) next to the associated time-averages for all radii (right hand side). All major bifurcation-related findings are visible in this high-resolution run ($n_{x,y} = 512$, $L_{x,y} = 64$): Flow asymmetry - with flattened positive flows and steepened negative flows -, a corrugation on top of the density gradient - with steepened areas around the negative flow domain wall -, and the radial streaks which are observed to contradict the intuitive expectation by moving downhill (with a detailed discussion following in Section 6.3).

$$|v_{y,min}| \approx 2 \cdot |v_{y,max}| \tag{6.1}$$
$$n'|_{v_{y,min}} \approx 2 \cdot n'|_{v_{y,max}} \tag{6.2}$$

while remaining overall momentum-conserved: $\langle v_y \rangle = 0$ holds true due to sharpened negative flows and broadened positive flows.
Even constraining the zonal flows into a strictly sinusoidal shape does not succeed in keeping the flows from returning to this asymmetric shape[2] the moment the external forces cease to be applied. Any distortion of either the flow pattern or the density corrugations - or of both - , changing amplitude, number or shape in either direction, will not derail the observed pattern for long. Additionally, artificially changing the frequency instead of the amplitude of the flows does not cause any significant change for the mean values of the density flux and the drift wave intensity.
Flow asymmetry has been confirmed through other means as well, by analyzing the Reynolds stress pattern. In all cases, the flow asymmetry - while approaching the steady state - is mirrored by the associated asymmetry in a sawtooth-shaped Reynolds stress, with a sharp increase at the negative flows and a slow decline in between. The positive-turning zero-crossing occurs at the location of the negative flow peak and vice versa, self-evidently associating the positive Reynolds stress area with the developing $v_y' > 0$-regime.
Replacing the natural flow or density corrugation pattern with a constant, artificially described pattern of similar shape is of no consequence to the remaining parameters, indicating that these bifurcated patterns do indeed describe the final steady state. Long-term stability of the resulting zonal flow state has also been confirmed by means of three extremely long-running simulations, utilizing more than 25,000 CPU hours each.

Generally, these results mark a first for an observation of robust transport bifurcations containing two different stable gradients in self-consistent drift wave turbulence simulations.

It has also been established that the two main features - the flow asymmetry and the density corrugations - exhibit a major dependence asymmetry, as seen in Figure 6.2. Artificially leveling the density corrugations and subsequently forcing them to remain so has considerable impact on the strength of the asymmetry since drift wave carry-off is impeded by the restrained density gradient. On the other hand, artificially symmetric flows do not cause the density corrugations to weaken significantly, with the argumentation presented in Section 6.2 still being valid. Thus, while the flow asymmetry depends on the density corrugations to a major degree, the inverse is not the case.
This result implies that the flow asymmetry is merely following from the more fundamental picture of density corrugations caused by drift wave repulsion asymmetries, having only an indirect retroaction effect on the transport by increasing drift wave generation at its steepened flow gradients as well as further fanning (and possibly even ceasing, as shown

[2] It is important to note that the asymmetry effect is never constrained to the radial-poloidal plane, but occurs similarly in the toroidal direction as well.

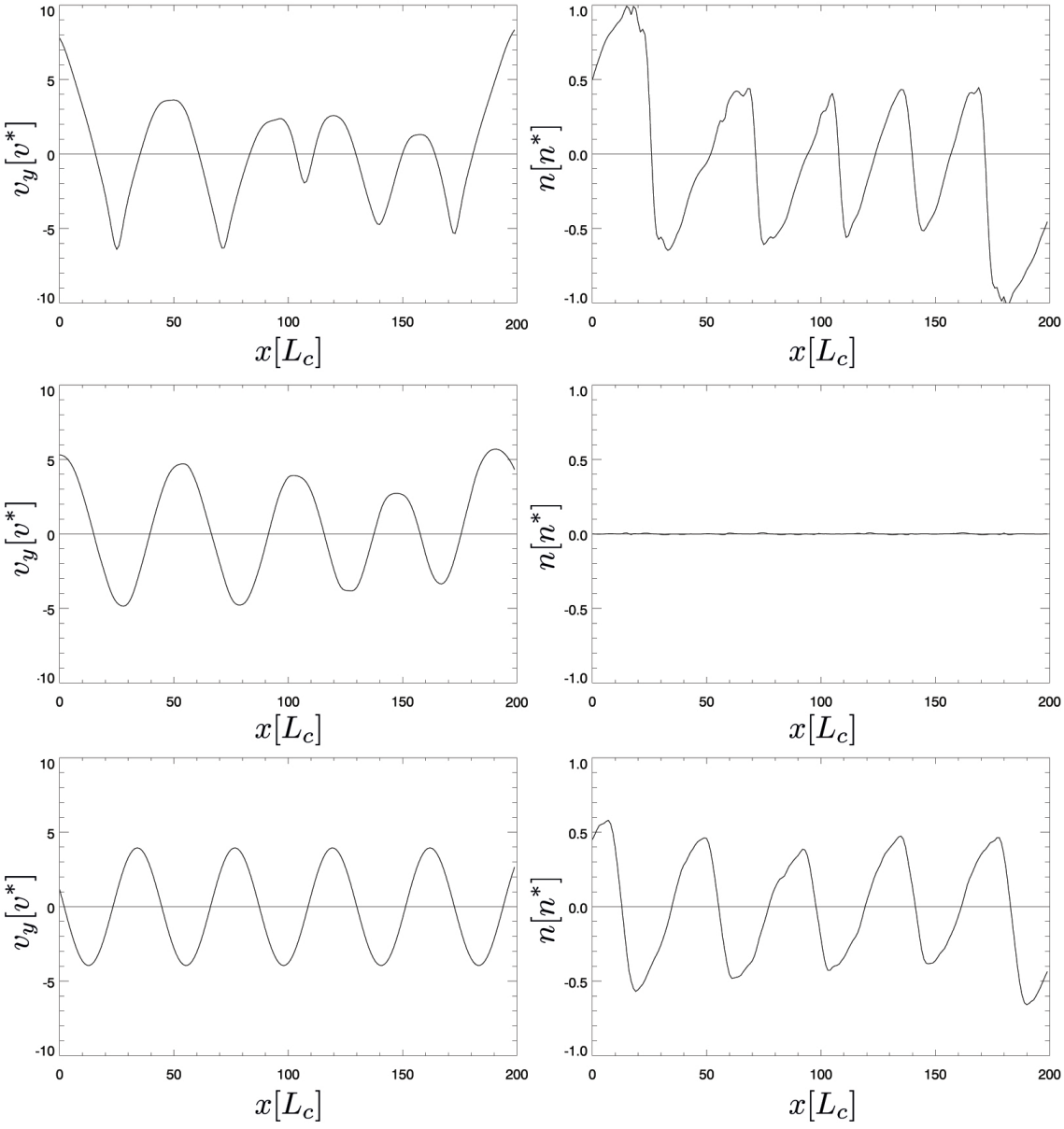

Figure 6.2: For $\hat{\rho}_s \approx 0.28$, poloidal flow v_y and density corrugations n are plotted against radius. In the top row, natural flow development is permitted (expect around the walls of the computational domain), yielding both flow asymmetry and density corrugations. In the center graph, the density is kept artificially constant at its initial smooth gradient - with the resulting zonal flow pattern being almost perfectly symmetrical. Below, such a symmetrical flow pattern is prescribed, however, this does not prevent density corrugations from developing. While the drop-off around the negative flows is not quite as sharp as in the natural case, it does exhibit a similar absolute change in amplitude.

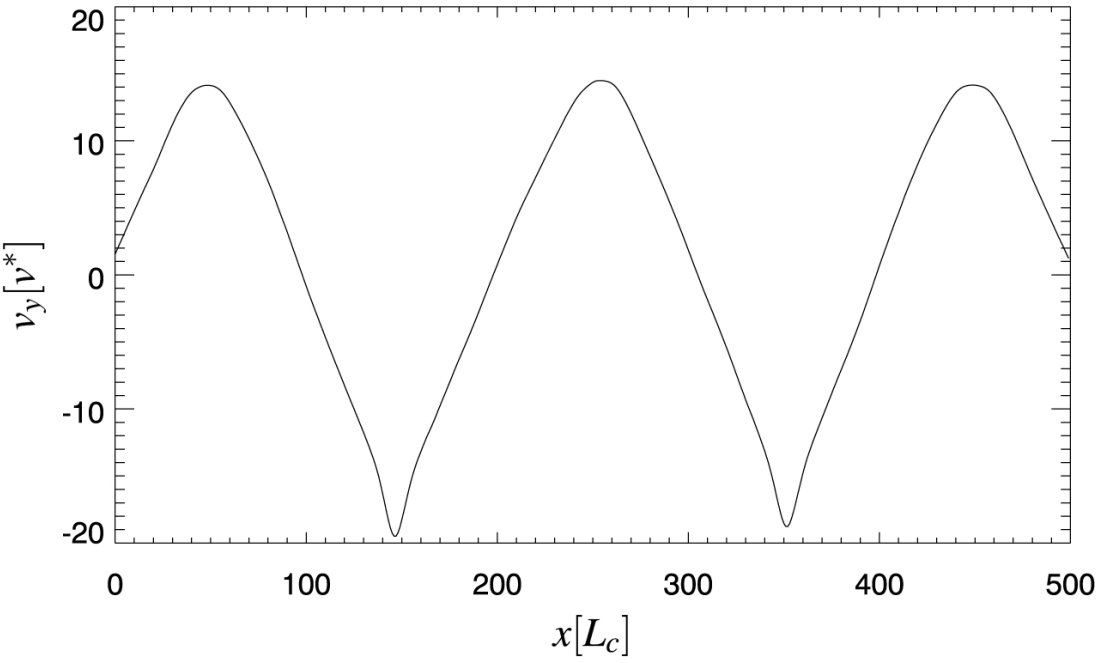

Figure 6.3: For a computation with $\hat{\rho}_s \approx 0.28$, steady-state poloidal flow v_y is plotted against radius, with a sinusoidal base pattern being prescribed artificially for v_y. Previously, the flow shear levels have asymptotically reached their maximum values almost everywhere within the domain. Noticeable exceptions occur next to the flow peaks, where the locally increased density gradient around the negative flow peak allows for an increased flow shear and thus also steeper flow minima in comparison to the flow maxima.

in (5.8)) drift wave repulsion around the location of the negative flows.

6.1.2 Parameter analysis

A more detailed parameter scan for $\hat{\rho}_s$ based on runs performed with up to $n_{x,y} = 512$ and $L_{x,y} = 32$ (close to the upper limits shown in Table 5.1) is presented in Table 6.1, including the ratio between the turbulent energy density $E_{tur} = n^2/(2\epsilon_n)$ and the ordered kinetic energy density $E_{kin} = v^2/2$ as well as their respective values, the onset $k_{y,fall}$ of the drop-off in the k_y-spectra (in units of ρ_s) towards higher values of k_y, the parameter $k_{y,fall} \cdot \rho_s$ as well as the stage of zonal flow development and their subsequent mean amplitude $\langle |v_y| \rangle$ as well as their asymmetry as measured by $v_{y,asy} = \langle max(v_y)/|min(v_y)| \rangle$. The same results hold true for negative shear as well since shear is a symmetry operation.
The results from these examinations as presented in Table 6.1 and in Figure 6.4 are consistent with all previous considerations. While the turbulent energy decreases for increasing $\hat{\rho}_s$, the kinetic energy peaks in the range were zonal flows form (especially so if they form on short time scales). The most significant parameter here is E_{tur}/E_{kin}, which drops below 1

Table 6.1: $\hat{\rho}_s$-parameter scan

$\hat{\rho}_s$	E_{tur}/E_{kin}	E_{tur}	E_{kin}	$k_{y,fall}$	$k_{y,fall} \cdot \rho_s$	$< \lvert v_y \rvert >$	$v_{y,asy}$
0.100	30.881	15.830	0.512	2.1	0.210	0.1 (chaotic)	n.a.
0.142	21.956	8.377	0.381	1.9	0.270	0.5 (chaotic)	n.a.
0.169	6.713	7.619	1.134	1.8	0.304	0.7 (chaotic)	n.a.
0.176	8.574	6.263	0.730	1.9	0.334	0.7 (chaotic)	n.a.
0.184	3.662	5.499	1.501	1.8	0.331	1.1 (transitional)	n.a.
0.192	3.338	5.771	1.728	1.8	0.346	1.2 (transitional)	n.a.
0.201	2.695	4.970	1.843	1.8	0.362	1.7 (zonal flows)	2.2
0.239	1.499	3.866	2.578	1.7	0.406	2.0 (zonal flows)	2.0
0.284	0.218	2.379	10.884	1.5	0.426	2.1 (zonal flows)	1.8
0.402	0.176	0.626	3.557	1.1	0.442	1.9 (zonal flows)	1.5

in the main zonal flow regime, strongly indicating the dominance of ordered kinetic energy over unordered kinetic energy for stable large-scale phenomena.
The spectra fit into this picture, with their drop-off wavenumber (in units of ρ_s multiplied with $\hat{\rho}_s$) remaining constant[3] in the zonal flow regime where ρ_s dominates, once again indicating that $\hat{\rho}_s$ is indeed the single dimensionless parameter determining the long-scale behavior of the system.
It is interesting to note that while $k_{y,fall}$ stays approximately constant in the turbulence regime (in units of ρ_s, as presented here) as well as constant in the zonal flow regime (in units of $L_\perp$), $k_{y,fall} \cdot \rho_s < 1$ remains true, always - reinforcing the result from Chapter 4 that drift waves modes beyond $k_{y,fall} \cdot \hat{\rho}_s \approx 1$ (in units of $\hat{\rho}_s$) exhibit next to zero growth.
Flow development behaves as expected, with higher flows occurring for higher values of $\hat{\rho}_s$. Flow asymmetry, however, is declining with higher $\hat{\rho}_s$ as seen in Figure 6.5, as the nonlinearity decreases - a circumstance that will become clearer after Section 6.2. Accordingly, the density corrugations have been shown to decrease somewhat for higher $\hat{\rho}_s$ as well. Maximum asymmetry of both parameters is reached close to the transitional value of $\hat{\rho}_s \approx 0.15 - 0.20$, where both estimates of (6.1) and (6.2) are surpassed.

Several reruns have been performed for all simulations, yielding the averages plotted in Table 6.1 and Figure 6.4[4] (for $n_{x,y} = 256$ and $L_{x,y} = 16$). Due to turbulent variations, the error bars for all measured parameters - primarily gained through differences in multiple runs based on the almost exact same initial distribution - are between 5 and 10% (and up to 20% for the more erratic energies). As always, these error bars could be minimized

[3] It is important to bear in mind that the non-linear distribution of the values of $\hat{\rho}_s$ is centered around $\hat{\rho}_s \approx 0.15 - 0.20$.

[4] In order to yield the average maxima and minima of the flow by a simple approximation - not considering the flow asymmetry, assuming a sinusoidal base shape instead - the values for $\langle |v_y| \rangle$ need to be multiplied by $\pi/2$. It should further be noted that a factor $2\pi/n_{x,y}$ is required to extract $k_{y,fall} \cdot \rho_s$ (for $L_\perp = 1$) from the raw code data.

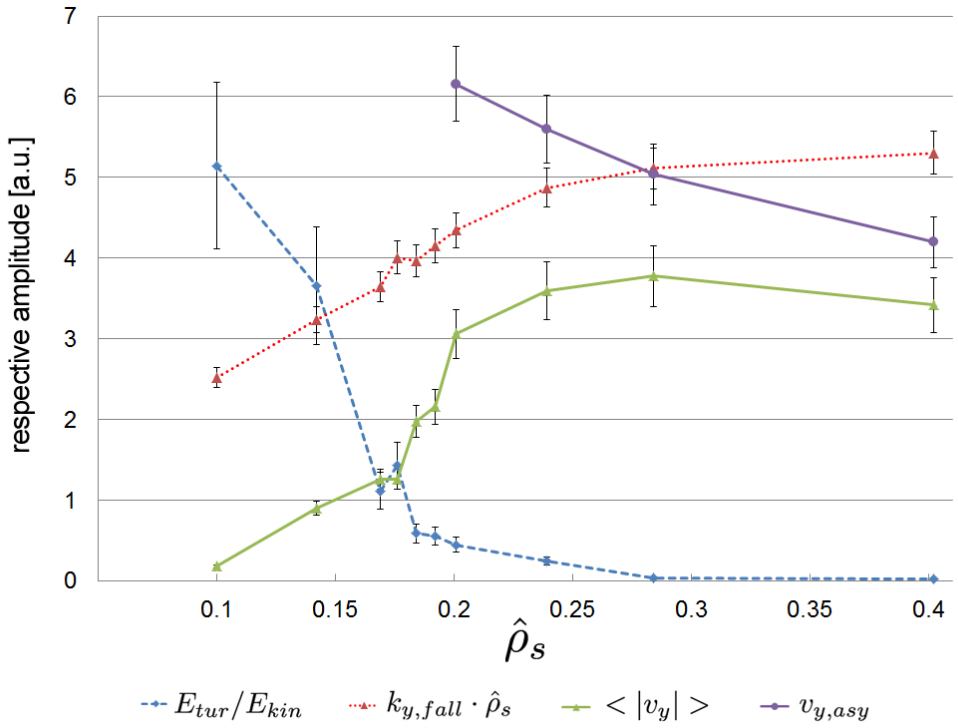

Figure 6.4: Four numerically calculated variables are plotted against $\hat{\rho}_s$, their respective values being adjusted to arbitrary units in order to depict them within one figure: Marked with blue dashes, the ratio between turbulent and kinetic energy is seen to drop to almost parity at the onset of the zonal flow regime, falling below 1 down the line. The red dots are associated with the $k_{y,fall}$-value (in dimensionless units of $\hat{\rho}_s$) right before the onset of the k_y-spectrum drop-off. The green line marks the mean associated zonal flow strength, whereby the weak values below $\hat{\rho}_s \approx 0.2$ are caused by chaotic and transitional zonal flows. Finally, in purple, the zonal flow asymmetry - only meaningful to be determined within fully developed flows - can be seen to decline for higher $\hat{\rho}_s$. Generally, the highest density of runs has been performed around the onset of zonal flow formation at around $\hat{\rho}_s \approx 0.15 - 0.20$, where they transition from semi-chaotic to large-scale stable behavior.

considerably by performing even more batches of runs - ultimately sinking well beyond 5% until other systematic errors not caused by turbulent fluctuations become dominant. And again, these results hold true even for values undershooting the zonal flow regime by far, no matter which combination of ρ_s, α_d or s is used to achieve a certain $\hat{\rho}_s$.

It is important to note that while simulations with $\hat{\rho}_s \gtrsim 0.5$ do still develop flow patterns, they take disproportionally long to reach a near-steady state behavior. The final flow states have been found to emerge on time scales $\sim (k^2 D)^{-1} \sim O(10^0)$ (with D being the particle

diffusion coefficient, marking turbulent transport as in Chapter 4) for $\hat{\rho}_s \approx 0.14$, of $O(10^1)$ for $\hat{\rho}_s \approx 0.28$ and of $O(10^2)$ for $\hat{\rho}_s \approx 0.56$, or, stemming from a more precise analysis,

$$\tau_{ZF_{numerical}} \propto \hat{\rho}_s^{3.5\pm0.8} \tag{6.3}$$

for the time scale of zonal flow emergence (compare Figure 5.6).
This result is in agreement with the theoretical expectations for drift wave growth and flow emergence stemming from time scale proportionality to $k^{-2}D^{-1} \propto \hat{\rho}_s^2\hat{\rho}_s^2$ (by utilizing the results from Subsection 4.4.3 within the high-$\hat{\rho}_s$ zonal flow regime and in units of $L_\perp$):

$$\tau_{ZF_{theoretical}} \propto \hat{\rho}_s^{4.0} \tag{6.4}$$

This revelation also leads to one of the reasons - next to looking in the wrong place or using a too cost-intensive gyro code - why prior [63, 96] investigations[5], with 3D turbulence studies just beginning to emerge [97], have never yielded asymmetrical drift wave zonal flows - or zonal flows at all, even though they have always been expected in an electrostatic resistive sheared-slab drift wave turbulence model following the Hasegawa-Wakatani equations [63]. Since the pure flow regime requires $\hat{\rho}_s \gtrsim 0.2$, it also requires long-running numerical computations in order for these flows to reach their asymmetric steady state[6]. A well-developed zonal flow with $\hat{\rho}_s \approx 0.2 - 0.5$ calls for something of the order of a few thousand CPU hours (or more, inflation-adjusted) to reach a steady state for a satisfactory resolution - a feat which was hardly achievable until a few years ago, preventing most computational endeavors from crossing the zonal flow threshold.

More detailed studies of the influence of the two scales, ρ_s and $L_\perp$, have yielded a number of additional insights:
Not only does the drift wave transport - as shown in Chapter 4 -, but also do the Fourier spectra peaks of the drift waves - as seen in Table 6.1 - scale perfectly with ρ_s as long as being in the zonal flow regime ($\hat{\rho}_s \gtrsim 0.15 - 0.20$). Of course, the same holds true for the $L_\perp$ scale in the case of $\hat{\rho}_s \lesssim 0.15 - 0.20$.
As these two insights imply, the transitional regime between these two scales seems to differ in length scale dependency between the drift wave and zonal flow pictures. In order to clarify this occurrence and to examine the behavior in the regime where $\rho_s > L_\perp$, zonal flow runs with $\hat{\rho}_s > 1$ would have to be performed. Unfortunately though, the respective run time increases too strongly with higher $\hat{\rho}_s$ so that the resources required for such a test could not yet be acquired.

As determined in Section 5.2, the observed flows are generated by negative turbulence viscosity, conveyed by Reynolds stresses. Scanning across all performed runs, this viscosity

[5] In 1996, matching numerical experiments by Zeiler, Biskamp and Drake could neither reach sufficient resolutions or domain sizes nor values beyond $\hat{\rho}_s \approx 0.16$, noting the high computational expense.

[6] Steadiness is always guaranteed by the flows themselves. In a purely turbulent case on the other hand, circumstances which permit a return to zero turbulence can theoretically exist [98].

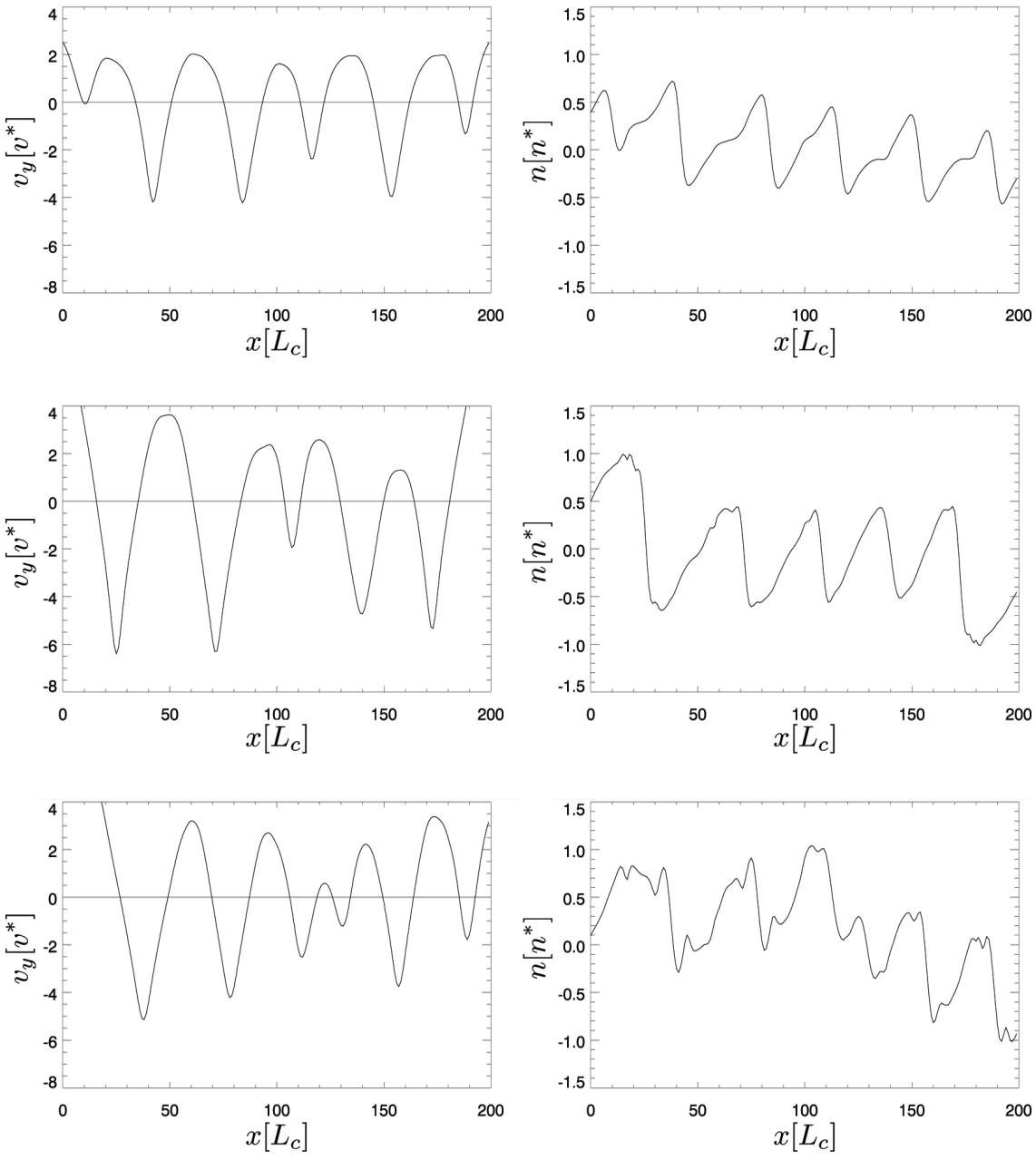

Figure 6.5: Poloidal flow and density corrugations are plotted versus radius for three different values of $\hat{\rho}_s$, with $\hat{\rho}_s \approx 0.20$ at the top, $\hat{\rho}_s \approx 0.28$ in the middle and $\hat{\rho}_s \approx 0.40$ at the bottom. Flow asymmetry can already be seen with the naked eye to diminish considerably, while the associated density corrugations tend to become equally less focused around the negative flow domain wall.

has been determined to depend only on four local parameters: The local flow shear v_y', the density gradient $\partial_x n$, the ion sound Larmor radius ρ_s and the shear length L_s.
Without flow shear (its direct result) or a density gradient (its energy source), there can by definition be no Reynolds stress. ρ_s is dominant within the zonal flow regime while the shear length L_s has been shown ((3.18)) to influence the drift wave zonal flow relationship by changing $\hat{\rho}_s$.
More surprising to these revelations is the fact that no non-local parameters exert influence over the turbulent viscosity, confirming that the Reynolds stress remains unaffected by any effects arising far from it.
As could be expected, turbulence intensity depends on the same four local parameters as well. However, it also depends on the second derivative of the flow.

6.1.3 Correlation with drift wave intensity

It can easily be seen in Figure 6.6 that the drift wave intensity does indeed correlate with flow strength, confirming that the negative flows repulse the turbulence while the positive flows attract the drift wave eddies.

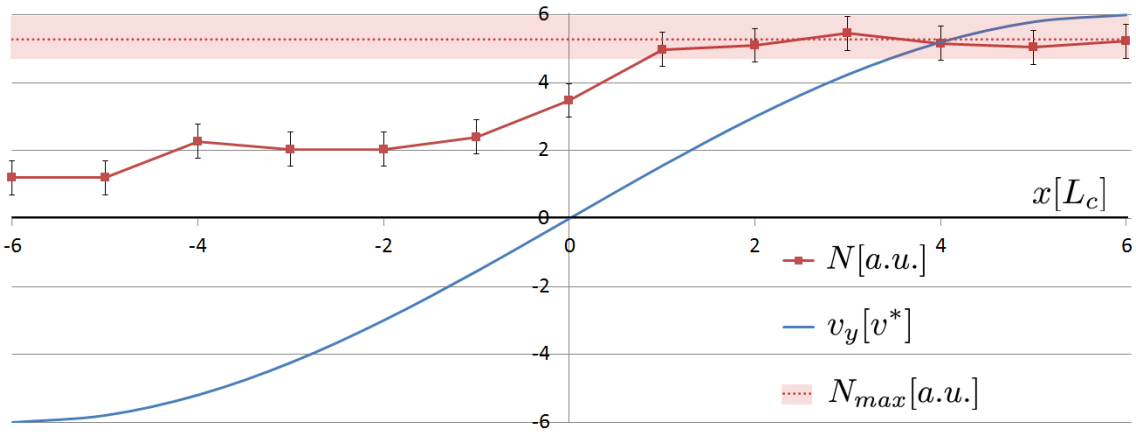

Figure 6.6: Against a radially sinusoidal flow pattern (the blueish curve), the numerically calculated drift wave intensity N is drawn in red. It increases with higher flow but begins to saturate soon after the zero-crossing, asymptotically approaching a limit marked by the reddish area around the dotted value of the approximate limit. Naturally occurring fluctuations within the turbulence are almost independent of the respective flow strength, causing constant, medium-amplitude error bars.

Yet, another few batches of run series have been performed in order to determine the relation between flow strength and drift wave intensity in further detail. The most important was a series where a certain sinusoidal flow pattern was prescribed while monitoring the development of the drift wave intensity by measuring the density square. Figure 6.6 shows a comparison between the peak flow strength v_y and the associated density square N at the flow maxima - not only supporting the picture of drift wave repulsion by negative

flows, but also showing that, while the positive flow peaks correlate nicely with the drift wave intensity in general, an upper limit N_{max} for the drift wave intensity is reached soon, already so for medium-strength positive flows with around $v_y \approx 2$.

6.1.4 Spectral dependencies

In addition, a more detailed look at the drift wave spectra is required. Orthogonal spectra always consist of a white noise plateau above the scale of fluctuations, followed by a bend at $k_{y,fall}$ as introduced in Table 6.1, kick-starting the self-similar polynomial decay which has been observed. Parallel spectra feature just the self-similar polynomial decay.
Generally, the structure of the spectra does not only scale with ρ_s and $L_\perp$ in the zonal flow regime as well as below, but also declines polynomially for high wavenumbers k over the entire $\hat{\rho}_s$ parameter range, thus exhibiting the same self-similar behavior for all relevant $\hat{\rho}_s$.
Apart from noise effects and once a sufficiently high resolution is reached, this cascade has to be linear down to the smallest resolvable scales[7] in both a $log\,(RMS(n))$-$log(k_\perp)$-plot and a $log\,(RMS(n))$-$log(k_\parallel)$-plot. Convergence can always be checked by verifying that $k_{\perp,fall}$ remains constant with respect to a further increase in resolution or domain size.
A detailed analysis reveals that in the zonal flow regime, the exponent e_{k_y} for this decline increases with $\hat{\rho}_s$ - albeit less than linearly. Specifically, it behaves as

$$\Delta e_{k_y}|_{\hat{\rho}_s \gtrsim 0.15-0.20} \propto (\Delta \hat{\rho}_s)^{0.6} \tag{6.5}$$

while remaining constant in the $L_\perp$ regime

$$\Delta e_{k_y}|_{\hat{\rho}_s \lesssim 0.15-0.20} \propto (\Delta \hat{\rho}_s)^{0.0} \tag{6.6}$$

with a smooth transition in between.

A typical center snapshot of the mean square density amplitude for a single point in time for k_y and $k_\parallel$ is provided in Figure 6.7. Even there, this massive increase of the exponent within the zonal flow regime is strongly visible.

6.2 Basic bifurcation mechanism

The different pieces in the puzzle necessary for a qualitative explanation of the basic bifurcation mechanism have been assembled.
The general shape of the flow pattern has been observed, most importantly an evolution towards a sawtooth-shaped state (ever more pronounced as higher resolutions are chosen), with the saturation levels of the symmetric flow shear - which approximates a perfect square wave - prescribing the same flow steepness at every radial location. More so, this

[7] These scales are still way above the dissipation scale, requiring $4-5$ orders of magnitude instead of just 2 between $k_{\parallel,min} = 2\pi$ and $k_{\parallel,max} = \pi n_z \approx 100$.

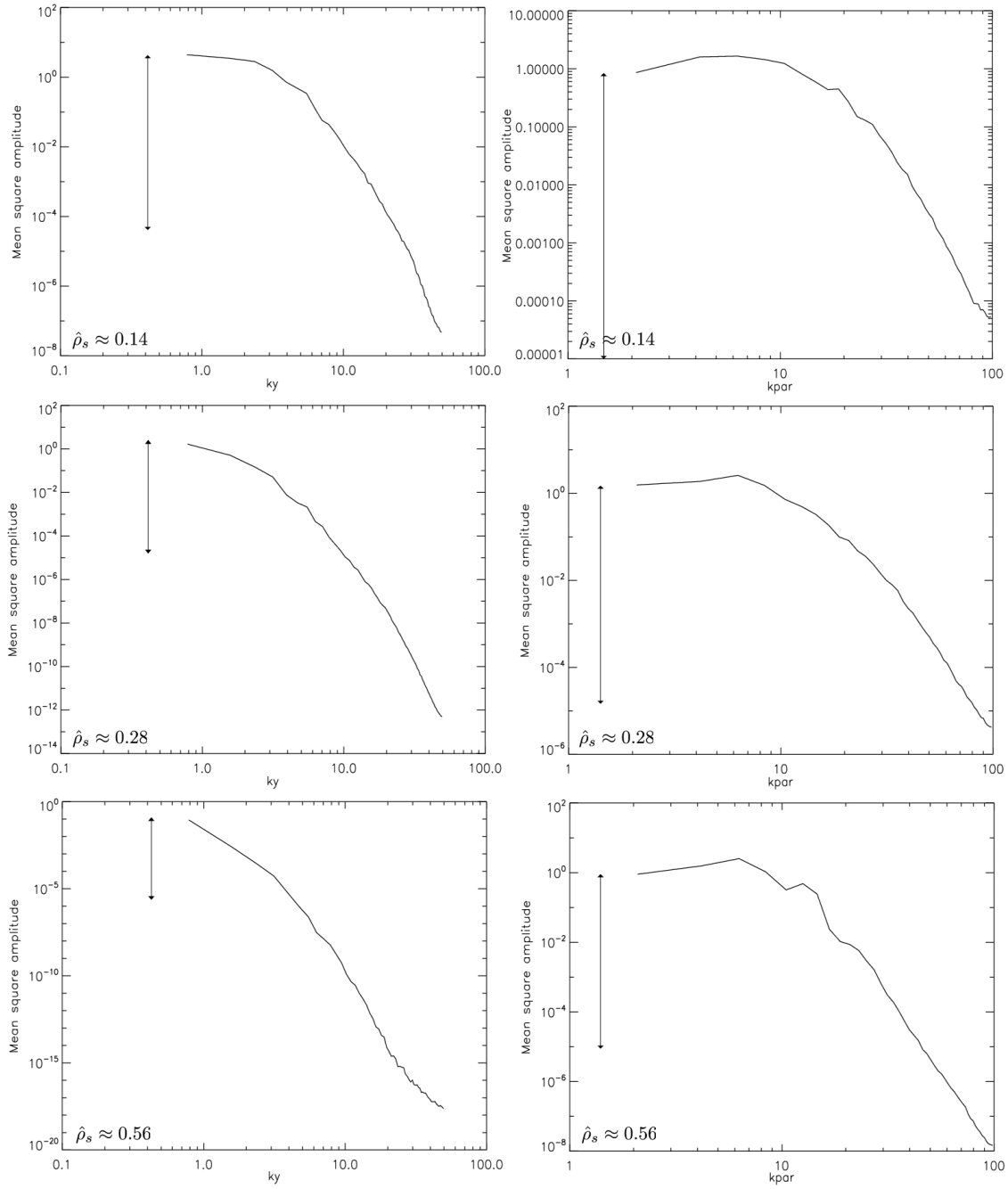

Figure 6.7: Spectra of the mean square density amplitude are plotted in the radial center (innermost 10% of the simulation domain) for three different values of $\hat{\rho}_s$, with k_y on the left and $k_{\|}$ on the right. Even on this single-time snapshot of the center, high-k self-similar polynomial behavior is recognizable. Comparison of the steepness of the decline then yields a stark increase for higher values of $\hat{\rho}_s$, pointed out by the two-way arrows depicting a delta of five orders of magnitude each.

maximum shear flow value also remains approximately constant (within all uncertainties) for a large variety of values of $\hat{\rho}_s$.
On top of this basic shape, the local, secondary influence of the density gradient[8] causes an increased generation of drift waves at the location of the negative flows, enabling a steepening of the flow gradient in close proximity around these while causing the opposite behavior for the rest of the domain.

Now, flow generation, saturation and asymmetry all follow from the aforementioned local dependencies, enabling a qualitative understanding of both the density corrugations and the flow asymmetry, founded on the repulsion of turbulence by the negative flows as derived in Section 5.2.

Density corrugations can be explained via the transport balance:

Negative flows repulse the turbulence according to $v_{gr,x} \approx -2k_{x_0}k_y\hat{\rho}_s^2 + 2v_y' t k_y^2 \hat{\rho}_s^2$ (as shown in (5.7)).
$\Rightarrow$ Since almost all transport (including diffusivity) is turbulence-related, transport is suppressed within an eddy length scale of the borders of the negative flow regime.
$\Rightarrow$ However, the overall transport balance[9] $\partial_x \Gamma(x) = 0$ has to be upheld (this is the same argument that was used for the turbulent cascades in Section 2.4).
$\Rightarrow$ Thus, higher density gradients are required to counter-balance the transport-diminishing effects of the turbulence suppression at the negative flows, developing on transport time scales.
$\Rightarrow$ Together with the associated density gradient flattening at the positive flows, this yields a breaking of the initial symmetry between positive and negative flows through ripples in the density gradient: The density corrugations.

Similarly, the flow shear can be drawn upon to understand the flow asymmetry:

Negative flows repulse the turbulence.
$\Rightarrow$ This leads to a carry-off of drift waves towards the positive flows.
$\Rightarrow$ This drift wave movement is associated with Reynolds stresses, especially so close to the negative flow peaks within the heightened density gradient regime.
$\Rightarrow$ This leads to increased drift wave generation rates, with those new drift waves constantly propagating towards the positive flow peaks.
$\Rightarrow$ These Reynolds stresses associated with drift wave propagation in turn change the zonal flow structure.
$\Rightarrow$ While radially drifting away from the negative flows towards higher values of $v_y(x)$, the $|\tilde{v}_x|$ of the drift waves begins to decrease, leading to a radial reduction in $-\langle \tilde{v}_x \tilde{v}_y \rangle$ and thus, according to (5.1), an increase in $-\langle y_y \rangle$ over time.

[8] Any increase in density gradient correlates to a decrease in ϵ_n on the $\hat{\rho}_s$-scale.
[9] In contrast to the drift waves themselves, transport is stationary.

⇒ The same drift wave movement leads to a slow decrease in $+\langle v_y \rangle$ around the positive flows.
⇒ In order to uphold total flow balance $\int v_y(x)dx = 0$ over the entire domain, the deepened negative flows are required to narrow down[10] while the flattened positive flows need to broaden, ensuring that the observed asymmetrical zonal flow pattern emerges.
⇒ The process of steepening flows finally stops and settles into a steady state free of net Reynolds stress effect once - as shown in (5.8) - the flow gradients become impenetrable to the drift wave flow.

6.2.1 Sub-structure

A more detailed examination yields flow ramp overshoots prior to the long-term steady state. Within an eddy length scale of both the sheared region in an artificial zonal flow pattern[11] as well as the mid-term, emerging natural flows, flow overshoot occurs, accompanied by an undershoot further away from the sheared region. The overshoot at the positive flows coincides with a positive change in turbulence levels while the overshoot at the negative flows is associated with a reduction in turbulence, both of which has been verified.
This serves to match the force field exerted by the flows (by changing the k_r of drift wave modes) at the locations of transition from flow shear to a flow plateau.

The shear flow pattern is still associated with a transport of turbulence - both from the main shear flow and from the positive flow undershoot - towards the positive flow plateau, or, more precisely, the positive overshoot region. With the opposite behavior at the negative flows (albeit with invisible undershoots due to the narrowing of the negative flow peaks), the turbulent transport can now be associated with the changes in the density gradient in greater detail, explaining the fine structure in n': The turbulent transport pattern not only causes a strong increase in density gradient strength around the negative flows, yielding an even deeper, steeper negative flow peak but also - due to the undisbanded overshoots - two smaller bumps of a decrease in density gradient located around the edges of the positive flows.
These patterns have been observed both in n' and v_y. They are most pronounced in the initial zonal flow regime, for sufficiently, yet not exceedingly high values of $\hat{\rho}_s$ (with the sweet spot being around $\hat{\rho}_s \approx 0.2$), and show behavior proportional to the overall flow asymmetry thereafter.

6.2.2 Influence of a chemical potential?

A more quantitative approach to explain the specific phenomena associated with this bifurcation mechanism examines the introduction of a chemical potential. The basic idea is described in Figure 6.8.

[10] This can only happen until a certain maximum steepness is reached and drift wave stalling occurs. Alternatively, numerical hyperviscosities do the trick once their resolution limit is reached.

[11] This pattern was prescribed in the shape of a logistic function, with smooth transitions to a positive and a negative plateau.

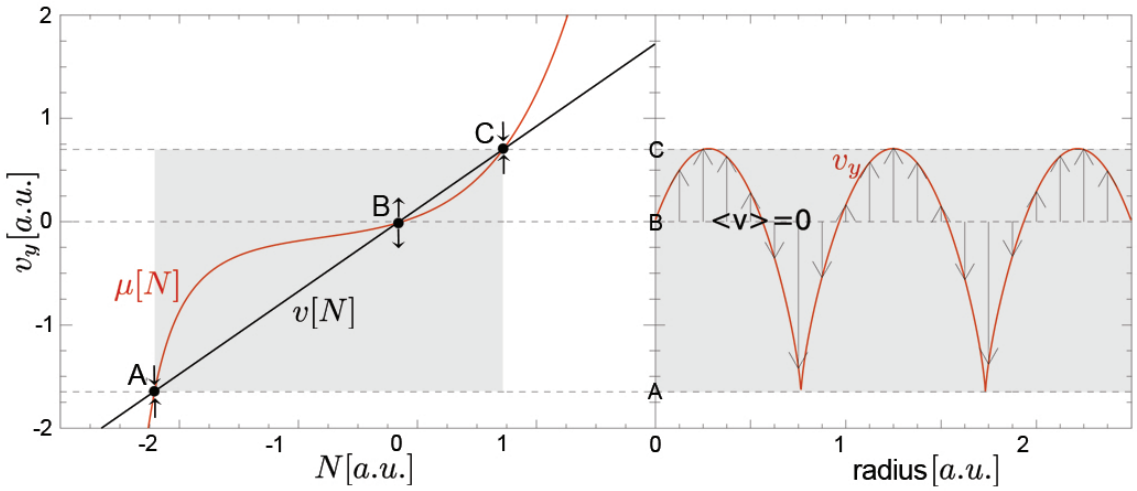

Figure 6.8: A mockup model mechanism for zonal flow asymmetry based on a chemical potential ansatz is presented. On the left hand side, $v_y[N]$ is plotted against the drift wave intensity N. Since chemical potentials behave as $\mu[N] \to -\infty$ for $N \to 0$ and since nonlinearity is crucial to positive flow saturation and stability, the ansatz $\mu[N] \propto N + N^2$ is chosen. At the same, the velocity $v[N]$ depends linearly on the drift wave intensity due to their direct correlation with the flows, $v_y[N] = N + const.$ is utilized. The three stationary points of intersection between these two equations encompass an unstable one at $v_y = v_0 = 0$ (denoted by the diverging arrows at point B) and two stable ones at points A and C (denoted by the converging arrows), confining the values of v_y and N within the zonal flows to the greyish rectangular box in the center. This corresponds with the zonal flow pattern v_y, plotted versus radius, on the right hand side. The asymmetry in $\Delta(v_{y,C} - v_{y,B})$ and $\Delta(v_{y,B} - v_{y,A})$ leads to an asymmetric shape of the resulting zonal flows due to the requirement that $\langle v_y \rangle$ must remain zero.

Based on this concept, a nonlinear equation system based on three balances has been created.

The first equation describes the correlation between the amplitude of the zonal flows and the respective drift wave intensity. Due to the repulsion of drift waves by the negative flows, N grows for increasing v_y:

$$\mu[N] = v_y + const. \tag{6.7}$$

Next is the transport balance required in any equilibrium state, as expected for the long-term behavior:

$$\Gamma[N] = const. \tag{6.8}$$

Finally, the drift wave intensity changes through growth as detailed in Section 4.2. Drift wave growth depends on the flows as well as on the density gradient, its energy source:

$$\dot{N} = \gamma[v_y, n'] \tag{6.9}$$

These equations are as plausible as they are vague. Attempts at constructing a quantitative set, modeled numerically with hyperviscosity terms[12], have led to inconclusive results, with the simulations tending to yield flow asymmetry and density corrugations, but at the same time depending too strongly on the choice of input parameters. The influence of a chemical potential could thus not be verified[13].

6.3 Radial downhill streaks

Contrary to all other tests aimed at verifying the results presented in Chapter 6, an analysis of the apparent radial flow of drift eddies - by imposing a modulation upon the drift wave pattern in order to make the underlying movement stand out - has yielded an apparent contradiction: Visible drift wave streaks (where streaks denote propagating fluctuations in transport) are not uncommon in zonal flow simulations [99], however, the streaks examined in this work with $k_{x,y} \approx 5 - 7$ in dimensionless code units seem to flow opposite to the flow gradient and thus downhill, towards the negative flow peaks[14]. While doing so, they bundle together, forming radial avalanches such as the ones shown in Figure 6.9.
This outward density movement for negative flow shear is highly counterintuitive, since uphill movement is expected in accordance with (5.7), or

$$\frac{\partial v_{gr,x}}{\partial t} = 2v_y' k_y^2 \hat{\rho}_s^2 \tag{6.10}$$

which is always negative for $v_y' < 0$.
The apparent contradiction occurs uniformly over the entire spectrum and can therefore not be discarded as a simple Galilei shift effect or fake downhill motion, with waves propagating without actually increasing the flux surface average[15]. Numerical effects, especially due to grid sizes, artificially high frequencies (reaching the Nyquist cut-off) or hyperviscosities

[12] Precisely speaking, these prerequisites lead to both a drift wave equation $\partial_t N = -\gamma (N - N_0) - \partial_x \left(-N\partial_x \left(\mu[N] - v_y\right)\right) - \beta\partial_x \left(N \left(\partial_x^3 N\right)\right)$ and a zonal flow term $\partial_t v_y = -\partial_x \left(-N\partial_x \left(\mu[N] - v_y\right)\right) - \beta \left(\partial_x^4 v_y\right)$, where $\mu[N] = \eta N \left(\alpha - 1 + N\right)/\alpha$ includes the first nonlinear term providing stabilization for saturation.

[13] Indeed, it seems very likely that no chemical potential exists at all since the drift wave propagation is insufficient to promptly relay enough information about the relative flow pattern on scales of the zonal flow wavelength.

[14] Accordingly, a n^2-v_y-plot yields drift wave intensity peaks at the negative flows which increase for stronger flows (approximately according to an amplification factor of $a + 0.5 \cdot |v_y|$ with v_y in dimensionless numerical units).

[15] It is crucial to consider the correct parameter for describing these streaks, this being a local mean for the streaks, denoted $\langle v_r n \rangle$, instead of the flux-surface averaged density transport (which even comes down to zero in the adiabatic case, when $\langle v_r n \rangle = \phi \cdot \partial_y \phi = 0$ since $\phi \perp \partial_y \phi$).

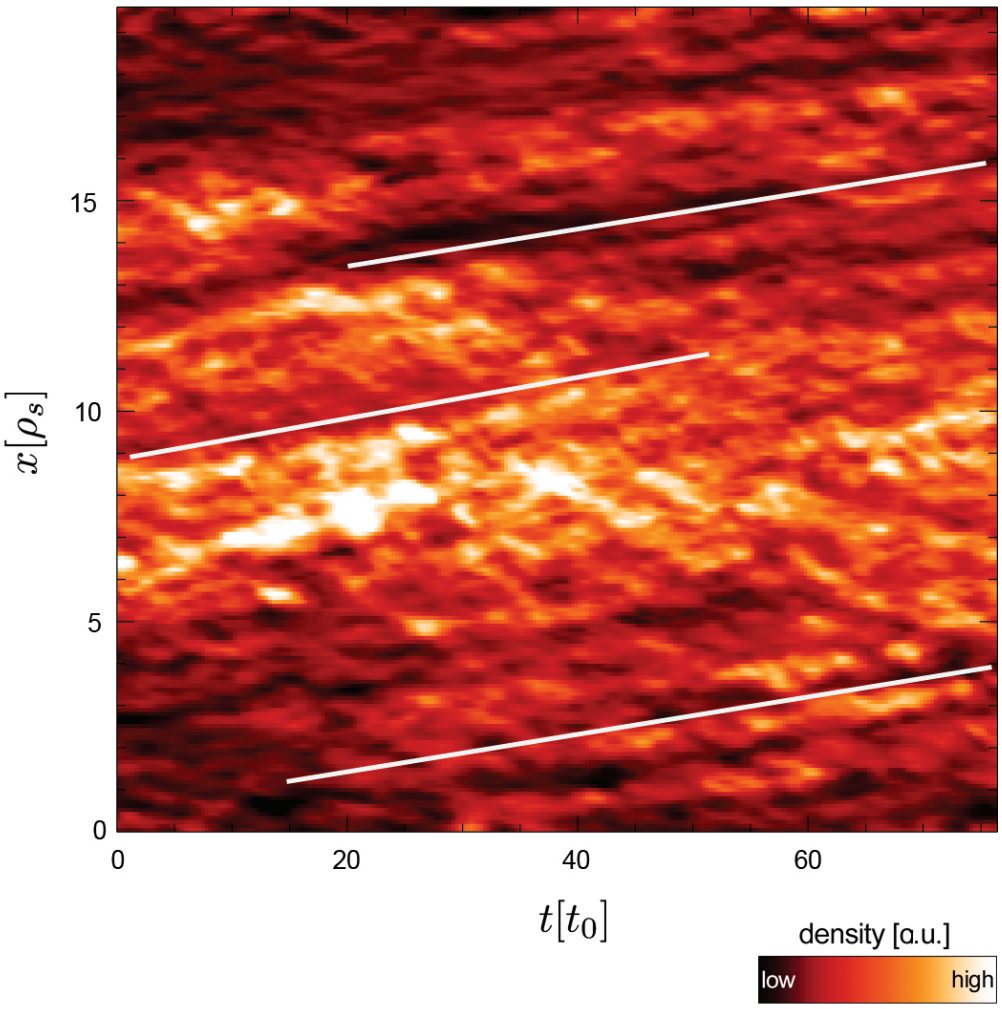

Figure 6.9: Radial streaks moving outwards over time. The y-axis marks the minor radius (or, in a slab system, the x-coordinate), brighter colors mark higher densities. A few selected streak events within the radial density transport picture and their consistent movement over larger time scales are highlighted by drawing white lines next to them.

can be discarded as well according to several test batches. Also, the damping rate is found to be negligible.

A more detailed analysis (with the results shown in Figure 6.10) of the apparent drift wave movement shows that the migration velocity decreases for steeper flows, with the system becoming more asymmetrical: Fewer eddies move against the flow gradient, while yielding a perfectly symmetrical net of diagonal streaks for $v_y' = 0$. The flux-surface averaged density transport will always be directed radially outwards, since the drift wave turbulence necessarily draws its energy from the density gradient, reducing it in the

process, transporting density down the density gradient - which, by definition, is always directed radially outwards.

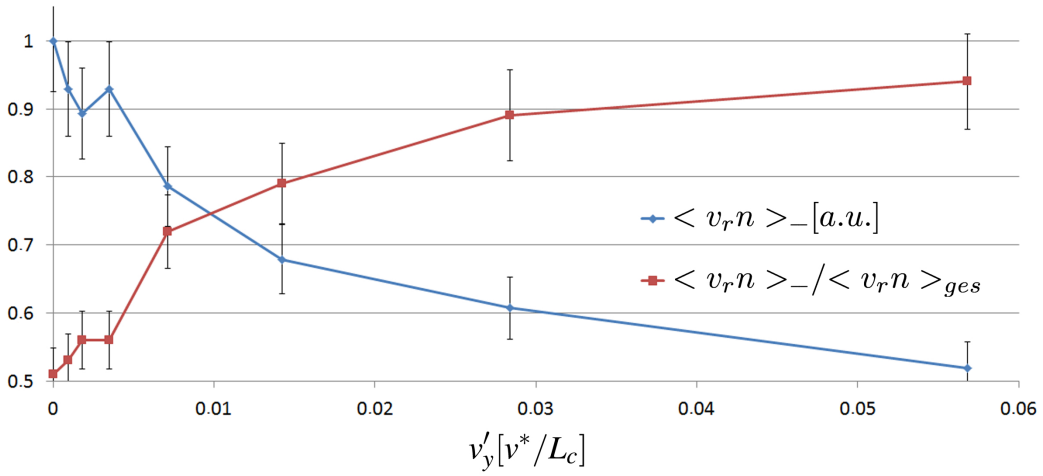

Figure 6.10: The numerical mean of the inwards directed radial density transport within streaks, $\langle v_r n \rangle_-$ is plotted in blue (in arbitrary units) against a wide variety of constant positive artificial flow gradients v_y'. As always, a nonlinear nonadiabatic sheared drift wave system is prescribed. Also pictured in red is the asymmetry between the inward and outward movement, $\langle v_r n \rangle_- / (\langle v_r n \rangle_- + \langle v_r n \rangle_+)$, with a value of 0.5 signifying a symmetrical 50-50 distribution between both types of streaks, while 1.0 means that only inward streaks are left. It is important to note that the exact same picture can be retrieved if the flow gradient is chosen to be positive and $\langle v_r n \rangle_+$ is measured instead (in fact, the mean depicted in this figure includes such batches of runs as well). The results are clear: With increasing v_y', the system becomes more asymmetrical with fewer outwards-moving streaks in comparison. At the same time, however, $\langle v_r n \rangle_-$ decreases considerably (while $\langle v_r n \rangle_+$ - not depicted here - increases). Generally, systematic irregularities lie below $\pm 10\%$.

Generally, as examinations e.g. with artificially reduced natural flow states show, drift waves still put energy into the system during zonal flow growth, with the Reynolds stress being in phase. But if the natural final flow state is artificially increased, enforcing massive reduction of the flow, this picture reverses, and Reynolds stresses become out of phase: Drift waves subsequently move downhill, reducing the flow, resembling the situation of the apparent contradiction concerning the radial streaks. So why does this also happen in a supposedly neutral final state, where neither zonal flow increases nor decreases are measured, but negative flows still reject the drift wave vortices?

Another puzzle piece has been provided by a large number of linear runs where only a single $k_x = -k_y$ mode was prescribed, with a negative flow gradient being present in the background. The development of this mode can be seen in detail in Figures 6.11 and

6.12: According to $\frac{\partial k}{\partial t} = -k_0 \cdot \frac{\partial v_y}{\partial x} \propto k_y$, the mode will topple over into positive k_x values, evolving proportionally to both time t and poloidal wavenumber k_y (accordingly, doubling the flow shear increases the propagation speed of the effect twofold). Broadening effects are especially prominent with the weak and weakly-growing high-wavenumber drift waves, leading to a fraying out for high k_y (an effect caused by the artificial hyperviscosities, which lead to a narrowing in real space in order to keep the system stable). Also observed is some lagging behind of the high k_y modes in comparison with their low-k_y-counterparts, with this effect becoming more pronounced for later times.
These results hold true for the nonadiabatic $s = 1$ case as well. Generally, growth in drift wave intensity can always be derived via (5.13) or (5.18).

Within the real space picture in Figure 6.12, on the other hand, the location displacement can simply be determined by integrating the group velocity, which comes down to (4.5) in the most simple case for adiabaticity and $s = 0$.
There, some initial movement directed radially outwards is followed by an oscillation through the $t = 0$ position and further elongation radially inwards (without flow shear, constant movement radially outwards would follow when still initialized with $k_x = -k_y$. For all times, a $k_{y,elong_{max}}$ where displacement is maximal exists, while δx approaches zero for both $k_y \to 0$ and $k_y \to \infty$. This behavior has been verified in its entirety by means of an analytical calculation. With non-negligible shear, however, analytical calculation of an eigenmode becomes impossible - as discussed in Section 4.3 -, rendering any comparison with the numerical experiment unviable. Numerically, though, only small changes occur to this pattern when either shear or nonadiabaticity join the picture (with the oscillation taking place faster and with a lower $k_{y,elong_max}$), yielding the same qualitative behavior as before.
This does not remain true anymore in the case of nonadiabaticity with shear. For some $s > 0$, - while the development of $k_x = -k_y$ still remains qualitatively the same as in the adiabatic $s = 0$ case - the oscillation properties cease to play a role, yielding (slow) radially outwards movement instead of allowing an inwards-directed propagation. Thus, for nonadiabaticity and shear $s \neq 0$ a strong discrepancy is found (as seen Figure 6.13), causing the linear approximation to break down in this limit.
The $k_x = -k_y$ considerations for small times t within a quasi-linear framework therefore do need to be contrasted with the late-time nonlinear picture.

A possible solution explaining this change in behavior is hidden within the drift wave action invariant introduced in (5.9). Analyzing the development of its mean with respect to time t and radial wavenumber k_x in a constant negative flow gradient environment yields a stark asymmetry in the pattern of the invariant, with a negative peak for small values of $k_x > 0$ and positive values for larger $k_x > 0$. But as described before, the negative invariant regime coincides with out-of-phase positive Reynolds stresses, leading to downhill drift wave movement. So it appears these few large-wavelength modes are the ones observed to move into the supposedly wrong direction while a majority of high k_x modes - moving in the previously expected direction - cannot be spotted due to their tiny wavelengths.
However, there are some caveats to this ansatz, mainly that Reynolds stresses are only

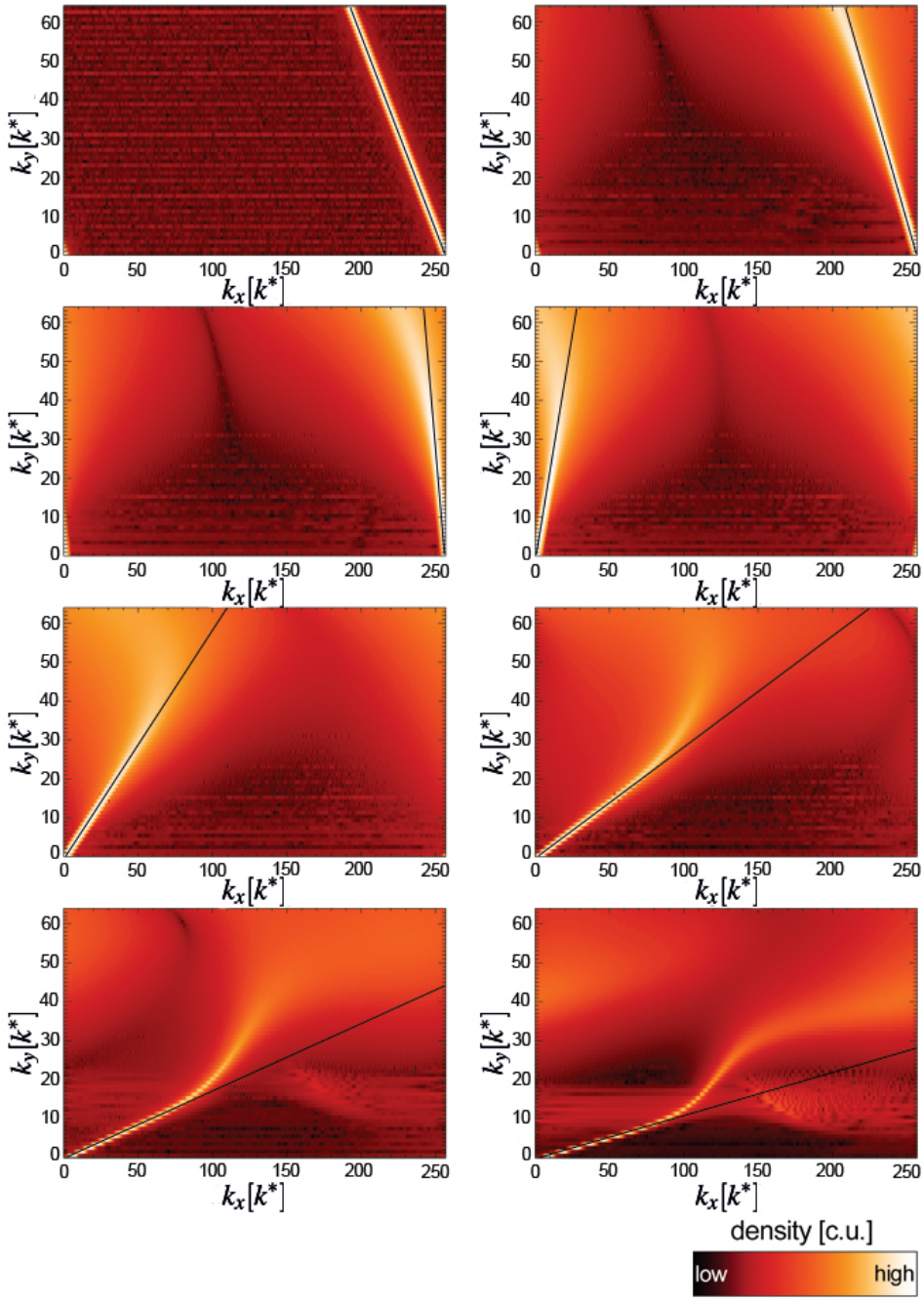

Figure 6.11: Logarithmic drift wave intensity under the influence of a constant negative flow gradient $v_y' < 0$ is compared to the analytical expectations (marked by thin black lines). Both are shown with respect to k_x and k_y (in dimensionless numerical units). For eight different times t, increasing from left to right, a sharp initial distribution $k_x = -k_y$ is observed to broaden while moving according to $\frac{\partial k}{\partial t} = -k_0 \cdot \frac{\partial v_y}{\partial x} \propto k_y$, with the k_x-values turning increasingly positive proportional to time t and poloidal wavenumber k_y.

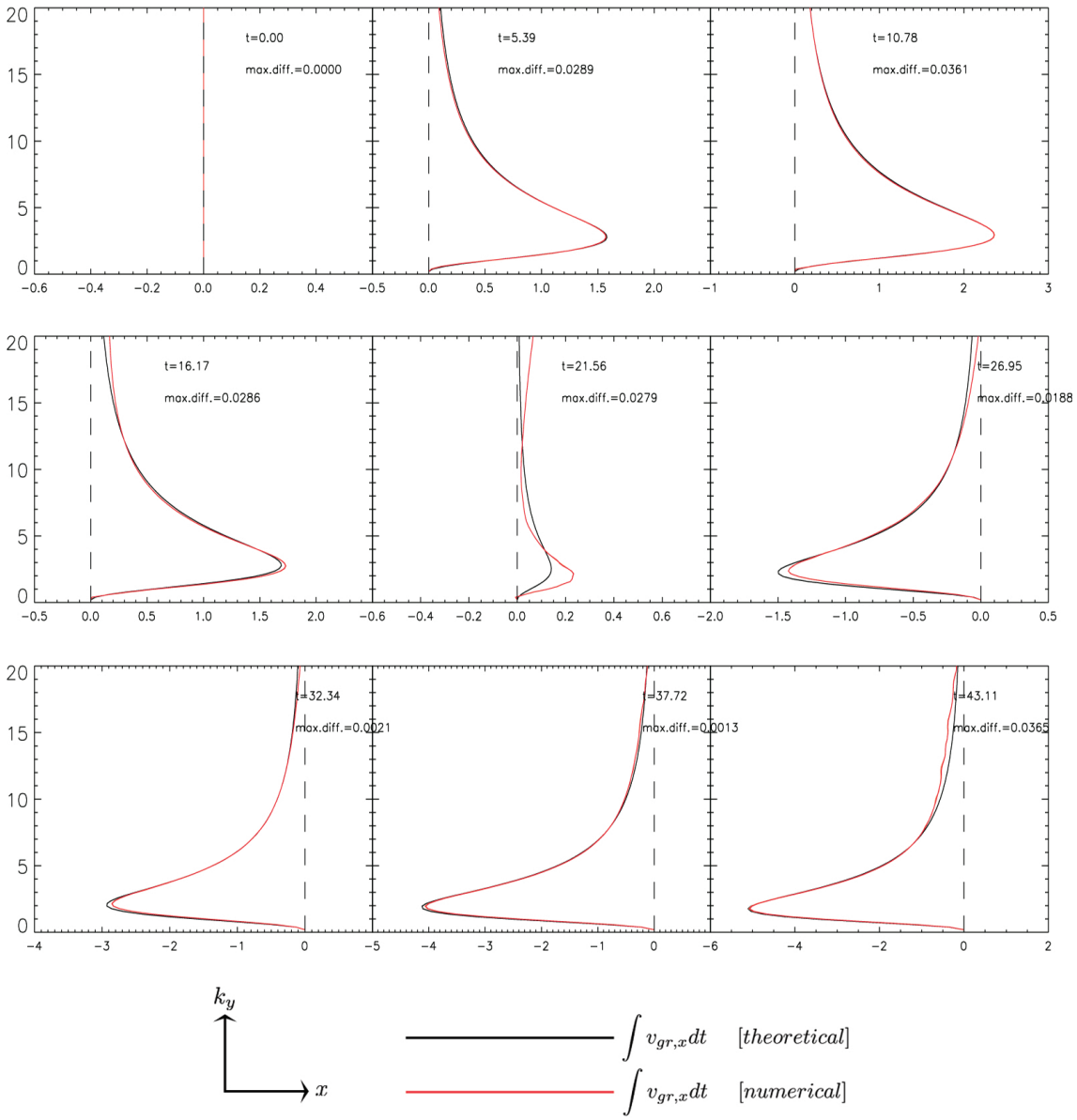

Figure 6.12: The adiabatic case for $s = 0$: The theoretically expected radial location of the maximal density (shown in black) for constant $v_y' < 0$ everywhere is determined for every value of k_y and different times t_0 (in dimensionless numerical units) by integrating $v_{gr,x}$ over time, beginning with $k_x = -k_y$. The results are subsequently compared to the numerical values of the density maximum (shown in orange), for which a tracking algorithm was devised. Excellent agreement between the linear expectations and the nonlinear numerical experiment is reached - in contrast to the nonadiabatic case for $s = 1$ described in Figure 6.13.

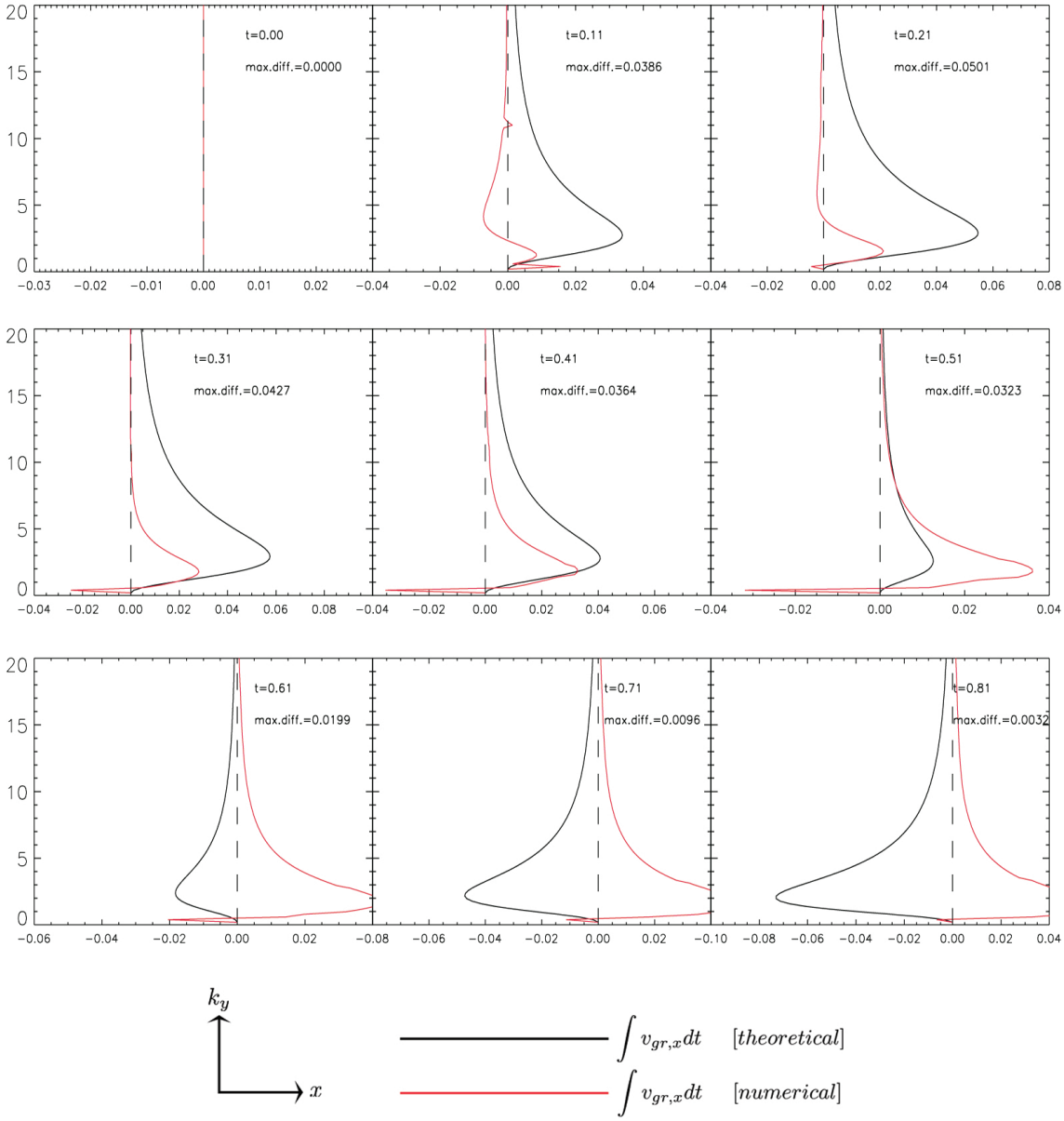

Figure 6.13: The nonadiabatic case for $s = 1$: The theoretically expected radial location of the maximal density (shown in black) for constant $v_y' < 0$ everywhere is determined for every value of k_y and different times t_0 (in dimensionless numerical units) by integrating $v_{gr,x}$ over time, beginning with $k_x = -k_y$. The results are subsequently compared to the numerical values of the density maximum (shown in orange), for which a tracking algorithm was devised. A stark qualitative difference between the linear expectations and the nonlinear numerical experiment is reached - in contrast to the adiabatic case for $s = 0$ described in Figure 6.12.

important in the transient stages, becoming increasingly irrelevant over time as the zonal flow pattern nears its final state. As seen in (5.1), the gradients in $\langle \tilde{v}_x \tilde{v}_y \rangle_{y,z}$ are proportional to the change in the flow pattern. In the end the only feature the Reynolds stresses still balance are weak hyperviscosities - which can be shown empirically to always hold true for high enough t.

Energy considerations provide another ansatz. The shear flow increases the wavenumber k_x of the drift waves during the swiveling of $\vec{k}_x$ experienced in Figure 6.11, yielding first an increasingly negative and finally a saturated group velocity $v_{gr,x}$ directed radially inwards (based on the above-used conventions). Since it is observed that (positive density) streaks propagate outwards, a possible solution to the apparent contradiction could be gained by introducing a solid state analog, with radially outwards moving positive density streaks providing a positive outwards transport corrugation on top of the constant density gradient-mining transport, with inwards moving negative density streaks satisfying the group velocity expectations.
The essential flaw here is that nothing equivalent to the opposite charges of electrons and holes exists: The sign of a density perturbation is irrelevant to the group velocity.

6.3.1 Streak generation

So there are only four different options left to explain the apparent contradiction associated with these streaks: Amplification, acceleration or scattering of the drift wave modes, with all of these possibly being wavenumber-dependent, as well as transport effects.
After all, the movement of the general energy directed radially outwards (for negative flow shear) or radially inwards (for positive flow shear) does not necessarily imply that the energy of an associated mode is transported inwards (or outwards, respectively) as well.

- Amplification via shear flow interaction is only expected to occur for high wavenumbers where the $\Delta\phi$ term in the vorticity equation becomes dominant. Generally, the growth rate is too small for direct amplification since $k_x = k_{x_0} - \partial_x v_y t |k_y|$ leads to $-k_x \ll 0$ very soon, while notable drift wave growth only occurs around $k_x \approx 0$ according to (4.19). Aside from actual growth, there is only the possibility of modes joining forces at a certain location, causing slow rearrangement of drift waves and the density profile within a quasi-steady state context. However, the apparent streaks have been observed over considerable amounts of time without much growth, thus dismissing the amplification theory.
- Acceleration up the hill, even applicable to only a few growing modes, is also no real option: Although $\partial_t v_{gr,x} \propto v_y'$ for small $|k_x|$, a finite $max(v_{gr,x})$ is necessarily reached soon for higher $|k_x|$ due to the growing denominator in the group velocity as described in (4.5).
- Scattering $\vec{k}_1 + \vec{k}_2 \rightarrow \vec{k}_3$, is a possibility, if drift wave turbulence levels reach an adequately high mean value: Once the Laplacian vorticity term in the Hasegawa-Wakatani equations becomes significant (which occurs roughly at $k\rho_s \approx 1$), drift

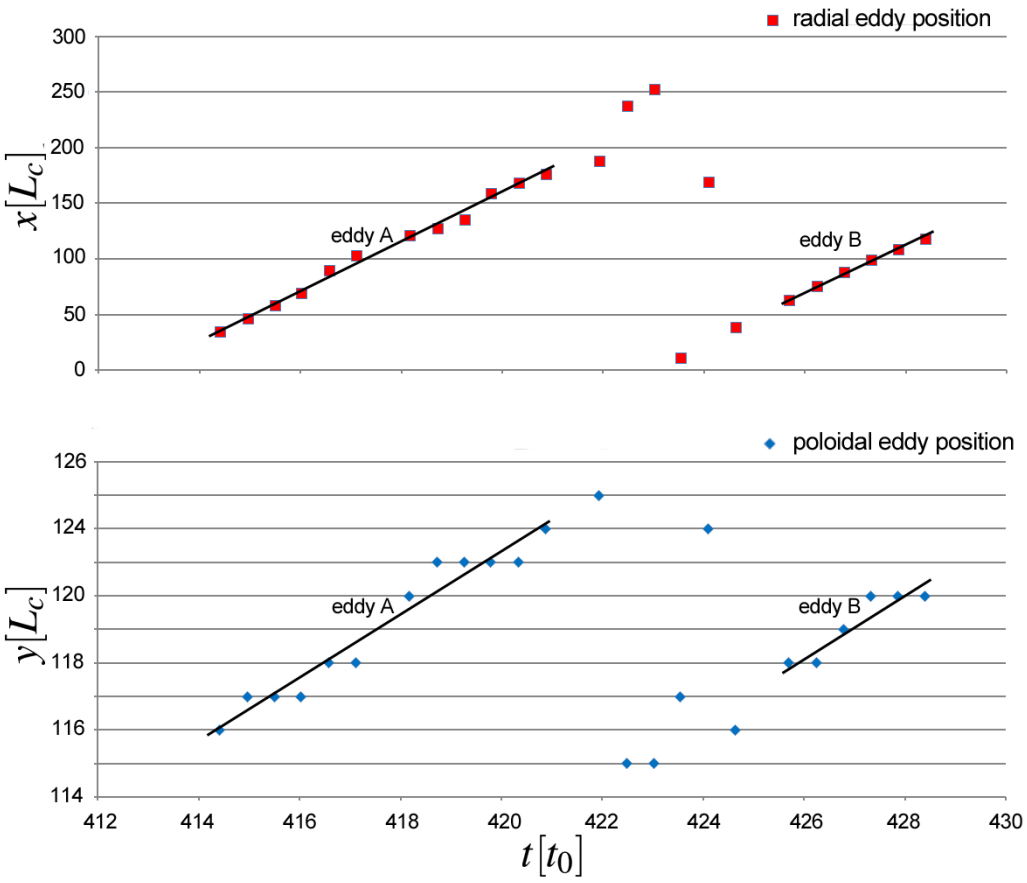

Figure 6.14: A tracking routine has been designed to lock onto a large number individual eddies - more specifically, their density maximum - emerging on a strong negative flow gradient background. Radial and poloidal position of the tracking results are plotted versus time. In this figure, a small exemplary section of a much larger domain with hundreds of individually tracked eddies is highlighted. An eddy A is tracked until it disperses. After a short interlude, during which this specific section remains streak-free, a second eddy B emerges, streaming radially (and somewhat poloidally, although these results are more coarse due to the low poloidal velocity and finite resolution) outwards with exactly the same speed as Eddy A. This picture repeats itself over and over, yielding precise statistics over time. All these eddies move radially outwards (thus downhill) with exactly the same velocity as has been measured for the streaks, strongly indicating that both are in fact the same - a theory further corroborated by a subsequent analysis of the spectra. These eddies are strongly associated with the density corrugations (holding the density gradient constant removes all counter-propagation).

wave modes with short wavelengths can experience sufficient scattering - something resembling shear flow optics - from high negative values $-k_x$ to high positive values k_x in order to never die out, keeping the circle going.

But do these specific high-frequency streak modes extract energy from the flow shear, keeping the flows in check? Or do they cause energy input (a process for which the exact timing of the backscattering proves essential, and an analytical calculation is impossible to implement)? Fueling the flows would be consistent with the classical drift wave picture valid for most modes, moving uphill, while energy extraction would be consistent with the observed, downhill-moving $k_{x,y} \approx 5$-streaks - a behavior which would help to keep the shear flows in check but which would also serve to explain their visual prominence in the radial density transport picture. When individual streaks are being followed by a sophisticated tracking routine (shown in Figure 6.14) - showing that the streaks are indeed the drift wave eddies[16] - while simultaneously monitoring the associated spectra, energy extraction seems to take place.

However, this does not appear to suffice to explain the complete picture: When the flux surface average of the density profile is held constant - still allowing for local distortions, and thus also streaks - the streak direction reverses.

- Corrugation-based transport could provide the solution. Assuming e.g. a negative flow shear profile $v_y' < 0$ and a negative density gradient $\partial_x n < 0$ with a corrugation on top, then the resulting transport peak around the location of the increased density gradient - attempting to diffuse the very corrugation itself - will be displaced to the left by the flow, moving to higher v_y. If this displacement is of the right magnitude (around $\pi/2$ of the density corrugation wavelength at the negative flow peak), the effect reverses: Instead of destroying the density corrugations through uphill streaks, the transport actually stabilizes the density corrugation steps. Thus, the observed downhill streak movement is a pure transport effect due to the transport peak displacement caused by the density corrugations - if only the effect strength is of a certain amplitude. And, as has been verified by a number of numerical computations, this happens to be just the case for non-artificial zonal flows within the observed range of $\hat{\rho}_s \approx 0.2 - 0.6$.

  This thought can be substantiated by a short calculation. Imagining a sinusoidal density distortion

$$\delta n = e^{ikx} \tag{6.11}$$

  with the transport Γ proportional to the density gradient

$$\delta\Gamma \propto -\nabla\delta n = -ik\delta n \tag{6.12}$$

  a displacement δx leads to

$$\delta\Gamma' = e^{-ik\delta x}\delta\Gamma \tag{6.13}$$

[16] This is further bolstered by a striking resemblance between the density flux and density patterns.

and therefore

$$\delta\dot{n} = -\partial_x \delta\Gamma' = -ike^{-ik\delta x}\partial_x \delta n \tag{6.14}$$

$$\approx k^2 \left(1 - ik\delta x\right) \delta n = k^2 \delta n - k^2 \delta x \partial_x \delta n \tag{6.15}$$

Now, if $k\delta x = \pi/2$ (where δx depends on the turbulence correlation time), pure displacement without any damping takes place.

Thus, the most important puzzle pieces have been assembled: These streaks do indeed consist of turbulent eddies - both streaks and eddies occupy the same space and move with the same velocity. In contrast to these streaks with increased density, their weaker - both amplitudes are equal only if a symmetric $v_y' = 0$ is prescribed - oppositely moving counterparts are marked by decreased density. Both kinds of streaks do not cause any significant amount of actual density transport, rendering them compatible with all previous energy considerations where only minor flow shear energy losses have been observed.
Artificially reducing the self-consistent zonal flows below a certain threshold percentage of their natural amplitude reverses the picture, yielding uphill streaks which reinforce the flows. Artificially keeping the density profile constant also leads to uphill streaks. Thus, without density corrugations, the drift waves would indeed flow in the correct direction. It is merely the corrugations in the density profile which cause the apparent contradiction by displacing the transport peak to such a degree that it actually stabilizes the corrugations instead of destroying them, reversing the direction in which the streaks naturally flow.

Chapter 7

Implications

The implications of this work reach beyond purely academic interest in the behavior of drift-wave based zonal flows. Zonal flows are ubiquitous both in experiment and nature - and in all of these cases, the long-term behavior of these macroscopic systems depends decisively on the interaction and properties of the small-scale fluctuations occurring within. A transport bifurcation found in any one of these systems opens up the possibility of them being commonplace.

Accordingly, Section 7.1 deals with the most obvious target: Actual fusion devices. Any change in transport levels - and even more so actual transport bifurcations - contains implications for confinement, which need to be discussed. Additionally, experimental examinations of predominantly drift wave-based zonal flows are still in their infancy, increasing the importance of numerical simulations in providing lines of attack for the experimentalists. One of the most interesting endeavors, especially with respect to the zonal flow asymmetry and density corrugations found in this work, is identified to be the targeting of the onset section of the high $\hat{\rho}_s$-regime as the easiest means of confirming (or refuting) the existence of transport bifurcations within actual fusion devices.

In Section 7.2, a completely different potential application of this work is presented: Two-dimensional atmospheric zonal flows in gas giants (and beyond), fostered by strong Taylor-Proudman columns due to fast rotation speeds. Here, geostrophic modes take the place of the drift waves, with Coriolis and pressure forces instead of the magnetic field and the density gradient. Accordingly, a finding of a transport bifurcation within Jupiter's atmosphere (such as the one described in this work) could lead to a much improved understanding - and possibly, long-term prediction - of its climate.

And since zonal flows are influential in numerous systems, ranging from interstellar nebulae and protoplanetary disks to the Venusian atmosphere, they occur on our home planet as well, with the jet stream being the most well-known example. The aforementioned bifurcations might thus even prove to be an important ingredient to future models of climate change for Earth itself.

7.1 Fusion devices

While drift waves in fusion devices have been measured for more than a decade [100], and even long-living large-scale structures [101] as well as basic zonal flows [102], mainly in the form of geodesic acoustic modes [103, 104], have been found[1], actual precision measurements of drift wave zonal flows in tokamaks have just recently begun [106], and, apart from a confirmation of an expected ρ_s transport scaling in the turbulence [107], observation of their major characteristics seems still a few years off. Any prediction of this work thus still has to await its verification - or its rebuttal.

An ideal way of testing the existence of bifurcations in actual fusion plasmas would be to try and attain the lowest $\hat{\rho}_s$-values still within the zonal flow regime, close to the transitional value. Exactly how this can be achieved depends on the actual device, with variation of the system size or the gradients usually not being a viable option, but the most promising approach is to regulate the external magnetic fields, thus controlling the ion mass electron temperature gyroradius ρ_s and accordingly the drift wave velocity α_d as well as changing the shear level s, both contributing towards getting the single dimensionless parameter $\hat{\rho}_s$ from (3.18) close to

$$\hat{\rho}_{s,target} = \epsilon_n^{1/2} \left(\alpha_d s\right)_{target}^{2/3} \approx 0.15 - 0.20 \tag{7.1}$$

where, according to Chapter 6, the strongest bifurcations are expected.

Experimental confirmation of the numerical and analytical results presented in this work could lead to important consequences for confinement. The single most important aspect is the flow shear around the steep negative flows, which is increased up to three-fold beyond bifurcation-free expectations, exerting exceptionally strong tearing forces on the drift wave vortices. Deepened flow minima could cause more drift waves to be reflected back inwards according to (5.7) before even reaching the negative flow peaks, becoming trapped and subsequently sheared apart in the broad positive flow pans.

After crossing a high-shear area, $|k_x|$ increases strongly, requiring the full expression of (5.7), not limited to $\left(k_x^2 + k_y^2\right) \hat{\rho}_s^2 \ll 1$

$$v_{gr,x} \approx -\frac{2k_{x_0}k_y}{\hat{\rho}_s^2 \left(k_x^2 + k_y^2\right)^2} + \frac{2v_y' t k_y^2}{\hat{\rho}_s^2 \left(k_x^2 + k_y^2\right)^2} \tag{7.2}$$

which leads to $|v_{gr,x}| \to 0$, a stalling of the drift waves.

For cleverly chosen parameters, the bifurcation-caused increase in gradient strength could thus suffice in severely hampering radially outwards directed turbulent transport, with the drift waves getting slowed down to the point of immobilization in steep enough flow gradients - possibly even cutting off a majority of the density flux altogether.

[1] A recent review of experimental zonal flow measurements can be read in [105].

7.2 Two-dimensional atmospheric zonal flows

As seen in Section 2.4, and in contrast to three-dimensional turbulence, the inverse energy cascade of two-dimensional turbulence favors large structures. This is important in many practical cases, such as in the rapidly rotating, convectively unstable (due to heating of the core) and thus strongly turbulent[2] atmospheres of gas giants [11] which are covered by a thin, stably stratified layer where the visible weather phenomena take place. In these systems, the Navier-Stokes equations apply, with both a Coriolis force term (the analog in a plasma would be a gradient in the potential) and a pressure gradient term entering:

$$\rho \left(\vec{v} \cdot \nabla \right) \vec{v} = \vec{F}_{ext} - \nabla p \tag{7.3}$$

Assuming the Rossby number - the ratio between inertial and Coriolis forces - to be small (which is true for all gas giants in the solar system, as they rotate rapidly), the advection term may be omitted. An incompressible flow under the impact of a scalar potential $F = \nabla \phi$ will now behave as

$$2\rho \vec{\omega} \times \vec{v} = \nabla \phi - \nabla p \tag{7.4}$$

where $\vec{\omega}$ marks the divergence-free angular velocity vector. Taking the curl of (7.4) now results in the Taylor-Proudman theorem

$$\left(\vec{\omega} \cdot \nabla \right) \vec{v} = 0 \tag{7.5}$$

This eliminates the possibility of velocity components parallel to the direction of the rotation axis of the planet and thus leads to quasi-two-dimensionality. Taylor-Proudman columns develop, rolls caused by the turbulent thermal convection originating in the hot interior of the gas giants. As shown in (7.5), these are parallel to the rotation axis. The intersection between these columns and the outer atmosphere leads to marked bands enclosing the entire planet with alternating directions at different latitudes: Atmospheric zonal flows.
The wind velocity for these zonal flows can be determined by simply equating both force densities, $\vec{F}_c = 2\rho \vec{\omega} \times \vec{v}$ and $\vec{F}_p = -\nabla p$, yielding the balance velocity

$$\vec{v} = \frac{\nabla p \times \vec{\omega}}{2\rho \vec{\omega}^2} \tag{7.6}$$

Thus, the alternating east-west winds are caused by the interplay of strong Coriolis forces and marked density gradients between high pressure and low pressure zones[3].

[2] Jupiter's atmosphere is even more turbulent than a typical tokamak plasma, which, at $Re \approx 10 - 100$ is better described by wave turbulence.

[3] On Jupiter, white clouds mark high pressure, while the higher-lying low pressure clouds get their brownish color from phosphorus and sulfur compounds.

The similarities between fusion devices and the atmospheres of gas giants are extensive. A planet's gravitation is equivalent to the curvature in a tokamak or stellarator. In fusion, the frozen-in magnetic field forces the vortices to align, while the Taylor-Proudman columns handle the same function in the upper layers of Jupiter (how deep into the planet's atmosphere they actually reach is controversial, see [64] and [108]). Finally, $\vec{E} \times \vec{B}$ drift velocity is the analog of the flow velocity in the hydrodynamic case, with nonlinearities in both cases being caused by vorticity advection [109].
This leads to the zonal flows on Jupiter posing as very close analogs of drift wave-based plasma zonal flows.

But of even greater importance is the close physical analogy between the low Rossby number geostrophic modes [18] (or Rossby waves) caused by instabilities in the atmospheres of gas giants and the drift waves in a drift-wave centric plasma [39] like the one analyzed here. Geostrophic modes are the small-to-medium-scale turbulent result of a local force balance between Coriolis and pressure forces, which substitute for the magnetic field and density gradient in the case of drift waves. Both act as turbulent fuel for their respective large-scale zonal flows.

7.2.1 Geostrophic modes: About climate change

The implications of the findings presented in this work for gas giants such as Jupiter could be severe. Their highly turbulent planetary atmospheres are still poorly understood, even more so due to their inaccessibility. Numerical models have thus far been unable to reproduce any features beyond the basic Taylor-Proudman structure.

Now that a transport bifurcation has been found in a purely drift-wave based plasma, it seems very likely that the existence of similar stable states in planetary atmospheres is no far-fetched assumption. Their understanding could lead to a much improved model for the changes of large atmospheric flows, and thus their very structure.
Since zonal flows heavily affect the level of turbulence and thus influence both confinement and density distribution within fusion devices, it is straightforward to propose that atmospheric zonal flows exhibit similar control over the pressure and flow distribution in their proximity[4]. An improved understanding of these flows could lead to an equally improved understanding of their effects on the climate of a gas giant. Going beyond that, the existence of a transport bifurcation in these atmospheric zonal flows could very well correlate with two different climate states, corresponding to high-impact events with severely dissimilar global climate conditions.

This realization could lead to a much refined model for Jupiter (via a yet-to-create fluid code based on spherical harmonics), and be a big step toward a long-term goal: A comprehensive and global climate forecast for Jupiter.

[4]Consequentially, a secondary bifurcation approach based on a tilting instability of the Taylor-Proudman columns [64] is the second promising ansatz for the generation of zonal flows on Jupiter and their effects on its climate - the first being the turbulence-based inverse cascade scenario.

7.2.2 Beyond Jupiter

But zonal flows (and drift waves, or their analogs) are not limited to Jupiter. They are ubiquitous in the universe [11], and so are the discussed ramifications of any bifurcation of theirs.

Small density inhomogeneities have been found to lead to ultra-low-frequency drift waves in magnetized dusty space plasmas [110]. Diamagnetic currents of heavier plasma species then drive these modes unstable, yielding a possibility of subsequent structure formation in these ionized gas clouds, easily spanning several a.u. [111]. Another likely birthplace for astrophysical zonal flows has been located within inhomogeneous rotating astrophysical fluids exciting geostrophic modes [112] - while even the wisps of the Crab nebula may be caused by an electron-positron plasma drift instability [113].
Zonal flows also appear to play an important role in protoplanetary disks [114], becoming excited by radial stress fluctuations driven by higher-than-expected turbulent diffusion. The resulting sub- and super-Keplerian flows are in geostrophic balance with density corrugations, determining future condensation clusters. The underlying Rossby waves in such protoplanetary nebulae, caused by mean vorticity gradients [115], are found to grow in the radial direction while propagating freely in the azimuthal direction [116].

Even in our own solar system, there are not only the Jovian flows, but also superrotating, self-organized bands on Venus [117], zonal flows on the Sun (the activity of which is an important contributor to the many solar effects crucial to Earth's climate) [118] and in the depths of Earth's oceans [119] - but most importantly, also in Earth's atmosphere. The jet stream with its iconic Rossby wave meanders [120] may be the most well-known example of a high-altitude zonal band spanning Earth, though it is just one of many. Even parts of the low-lying global atmospheric circulation can be considered blurred zonal flows.

Therefore, any insight gained from transport bifurcations leading to two stable states in planetary atmospheres does not only have consequences for gas giants, but also for our home planet. It is possible that its global climate models can thusly be refined to include potential climate bifurcations and therefore even have implications for climate change on Earth itself.

Chapter 8

Conclusions

Zonal flows are an essential asset in any high-confinement fusion device, controlling radial turbulent transport through high flow shear. Consequently, they may be connected to the generation of many transport bifurcations, including the fast-developing H-mode occurring up to the high-gradient, drift wave-populated edge, making a better understanding of their underlying principles indispensable. Due to the nonlinearities and disparate scales involved, any examination requires costly numerical computations in addition to analytical work. These were performed with the help of the nonlinear two-fluid Braginskii code NLET, with the underlying theme of this work revolving around an analysis of bifurcations in the drift wave-based zonal flow regime. The main results concerning the discovery of two transport scales, the origin of the zonal flow transition and a subsequent transport bifurcation associated with density corrugations and a zonal flow asymmetry are derived in Section 4.4, Section 5.4 and Sections 6.1-6.3, respectively.

First, the specific characteristics of the turbulence in this sheared-slab collisional drift wave system had to be analyzed. The associated Hasegawa-Wakatani equation set was transformed into a shape where a single dimensionless parameter $\hat{\rho}_s$ - defined in [63] as $\hat{\rho}_s = \rho_s/L_\perp$, the ratio between the ion sound Larmor radius ρ_s and a second orthogonal length scale $L_\perp$ which increases with the drift wave velocity α_d and decreases with magnetic shear s - determines the entire behavior of the density and potential, apart from quantization effects for insufficient domain sizes and the secondary influence of the radial positioning of resonant surfaces. Numerical cross-checks by varying either α_d, ϵ_n (relating gradient and system sizes) or s - all of which are contributors to $\hat{\rho}_s = \epsilon_n^{1/2}(\alpha_d s)^{2/3}$ - confirmed that $\hat{\rho}_s$ is indeed the single factor of influence within the system. This allowed for a reliable calculation of the exact group and phase velocities for both adiabatic and nonadiabatic drift waves in the new units, as well as the nonadiabatic $\hat{\rho}_s$-based drift wave growth rate. Subsequently, the influence of magnetic shear as well as of resonant surfaces and the general conditions for drift wave stability and instability in this system were discussed. A number of numerical issues - notably parallel hyperviscosities, boundary effects, artificial flows and choosing the correct value of the substitute Alfvén parameter $\alpha_{m_{add}}$ - were identified and dealt with.

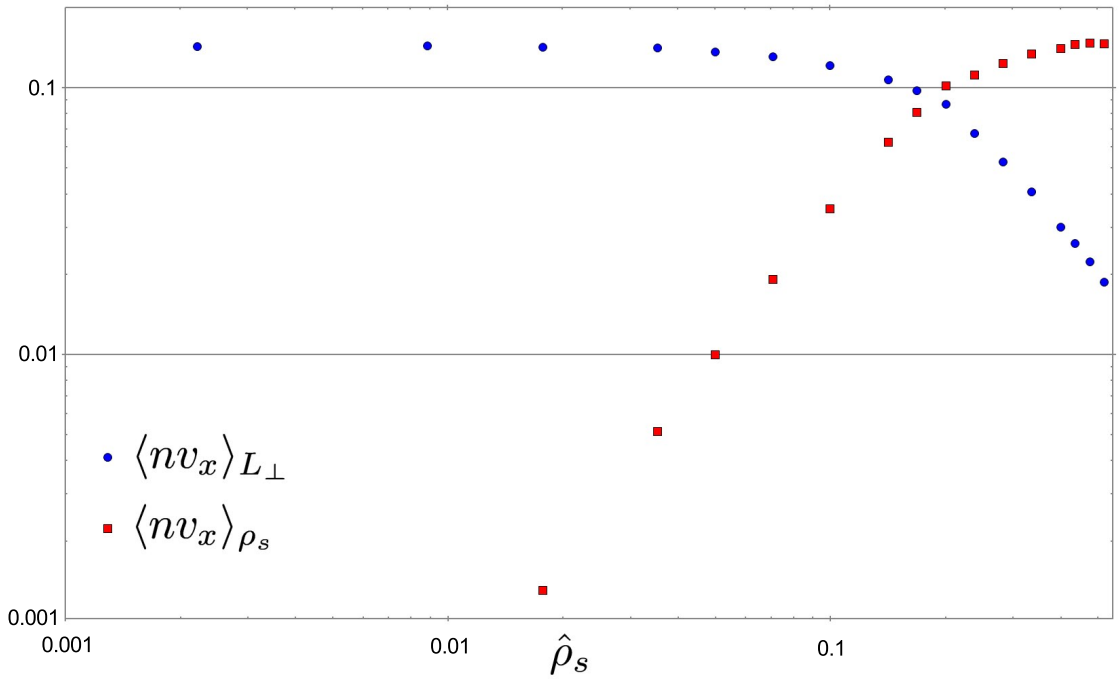

Figure 8.1: In this graph, resembling the core information of Figure 4.6, density flux is plotted versus the dimensionless parameter $\hat{\rho}_s$, according to the values presented in Tables A.1 and A.2. The averaged computational data for the density flux $\langle nv_x \rangle$ in units of the radial length scale $L_\perp$ (marked in blue) converges for low levels of $\hat{\rho}_s$ and decreases $\propto \hat{\rho}_s^{-2}$ for higher values of $\hat{\rho}_s$, while the density flux in units of the second orthogonal length scale ρ_s (marked in red) exhibits the opposite behavior, with a plateau for high $\hat{\rho}_s$ following an increase $\propto \hat{\rho}_s^2$ for low values of $\hat{\rho}_s$. Thus, the transport values in units of ρ_s converge to a constant for high $\hat{\rho}_s$ while those in units of $L_\perp$ converge for low $\hat{\rho}_s$. The transitional region with respect to the two convergence regimes positions itself around $\hat{\rho}_{s,transition} \approx 0.15-0.20$ (determined more precisely to be $\hat{\rho}_{s,transition} = 0.185$). The reddish density flux values in units of $L_\perp$ are therefore plotted increased by a factor of $1/(\hat{\rho}_{s,transition})^2 \approx 29$ in order to be shown in the same graph (and in order to visualize the transition between the two transport regimes), since by definition they reach a similar level as those in units of ρ_s only for $\hat{\rho}_s = 1$.

Finally, the influence of the parameter $\hat{\rho}_s$ was analyzed in detail. The existence of two dominant scales, the ion gyroradius scale (which, as expected, has been found to scale perfectly with the drift wave vortices) and the resistivity length scale, was derived analytically and subsequently confirmed numerically. In order to determine the influence of the remaining two scales ρ_s and $L_\perp$ on the density flux, the expected diffusion coefficients were derived analytically using a mixing length estimate, ultimately yielding a simple relation (4.50) between the units of D_{ρ_s} and the units of $D_{L_\perp}$,

$$\frac{D_{L_\perp}}{D_{\rho_s}} = \hat{\rho}_s^{-2} \tag{8.1}$$

where $D_{L_\perp}|_{\hat{\rho}_s \to 0} \to const.$ and $D_{\rho_s}|_{\hat{\rho}_s \to \infty} \to const.$. After predominantly domain size-based convergence issues in the high-$\hat{\rho}_s$-regime had been resolved and analyzed (approximated in an empirical relation for different $L_{x,y}$ and $\hat{\rho}_s$ shown in (4.56)), numerical experiments were able to confirm these expectations to an excellent degree when examining the computational values of the density flux, with both the $\hat{\rho}_s^{-2}$-relation as well as the two transport plateaus in their respective units being verified as shown in Figure 8.1 (originally from Figure 4.6) and equations (4.53) and (4.55):

$$\langle nv_x \rangle_{L_\perp}|_{\hat{\rho}_s \to 0} \propto \hat{\rho}_s^{-0.004 \pm 0.02} \qquad \langle nv_x \rangle_{\rho_s}|_{\hat{\rho}_s \to \infty} \propto \hat{\rho}_s^{0.06 \pm 0.20} \tag{8.2}$$

Finally, the transitional value of $\hat{\rho}_s$ between the scales was identified with the onset of zonal flows, which emerge solely within the more adiabatic and thus only weakly nonlinear ρ_s-regime for high $\hat{\rho}_s \gtrsim 0.15 - 0.20$, allowing large-scale structures to develop. An analytical explanation for the zonal flow regime transition based on a resonant surface gradient has been proposed for the first time. The frequency gradient length of the resonances gained through a mixing length argument - describing the approximate distance up to which significant repulsion by the resonant surfaces can be felt for the drift waves - decreases with increasing $\hat{\rho}_s$ since the gyroradius and the distance between two resonant surfaces grow.

There is also the issue of the $\hat{\rho}_s$-independent flow gradient. As is known [47], a wavekinetic analysis of the nonlinear drift wave self-interaction mechanism causing Reynolds stresses - which in turn fuel the zonal flows - leads to a modified radial group velocity equation accounting for the now shear-flow-gradient-dependent radial mode wavenumber $k_x = k_{x_0} - v_y' t |k_y|$ (where $v_y' = \partial_x v_y$). The consequences of this alteration are considerable, as it implies repulsion of the drift waves by the flows opposite to the electron diamagnetic drift direction - dubbed negative flows - and subsequent attraction (and possibly even trapping) by the positive flows, as seen in Figure 5.3. Thus not only resonant surfaces but also zonal flow minima act such that they repulse the drift wave turbulence. Using the $\left(k_x^2 + k_y^2\right) \hat{\rho}_s^2 \ll 1$ solution (5.7) to $v_{gr,x}$ for large k_x, $v_{gr,x} \approx 2k_y \left(v_y' t k_y - k_{x_0}\right) / \hat{\rho}_s^2 \left(k_x^2 + k_y^2\right)^2$, it can be seen that the drift waves can - in addition to being trapped at the positive flows - even become stuck in steep enough flow gradients, cutting off radial density transport altogether.

Now, when the resonance gradient length is compared to the flow shear gradient length, two cases are possible. For low $\hat{\rho}_s$, the resonance gradient is stronger than the shear flow gradient. Thus, uphill (as defined with respect to the flow pattern) acceleration by the flow as described in (5.7) merely serves to decelerate the downhill propagation due to the resonance gradient on the downhill-side, presenting these modes with more time next to the resonant surface, growing stronger than their uphill-side counterparts. The resulting, predominantly negative Reynolds stress as seen in Figure 8.2 (originally from Figure 5.7) prevents zonal flows from forming. For high $\hat{\rho}_s$, on the other side, only uphill

acceleration remains, leading to positive Reynolds stresses and thus zonal flow growth. A transitional third regime seems conceivable where the local flows caused by drift waves are insufficient to overcome the resonance gradient, but artificially induced high-amplitude shear flows are not. This is possible shortly below the transition (5.26) between dominance of the resonance gradient derived from its radial resonance mixing length distance r_{ml} and dominance of an (oppositely directed) zonal flow gradient $\partial_x v_y$. This threshold occurs at

$$\partial_x r_{ml}\left(\hat{\rho}_s\right) = -\partial_x v_y \tag{8.3}$$

Ordered flows were shown to emerge - a first within a Hasegawa-Wakatani equation set due to the high-ρ_s high-resolution computations required - on time scales τ that are increasing rapidly with $\hat{\rho}_s$ (as shown in Figure 5.6), tenfolding for each doubling of the parameter, making high-$\hat{\rho}_s$-studies beyond $\hat{\rho}_s \approx 0.5 - 0.8$ increasingly unfeasible. While a derivation via the proportionality $\tau \propto k^{-2} D^{-1} \propto \hat{\rho}_s^2 \hat{\rho}_s^2$ gained from a mixing length discussion yields good agreement between the theoretically expected (6.4) and the experimentally measured values (6.3) of the inverse zonal flow growth rate

$$\tau_{ZF_{theoretical}} \propto \hat{\rho}_s^{4.0} \qquad\qquad \tau_{ZF_{numerical}} \propto \hat{\rho}_s^{3.5 \pm 0.8} \tag{8.4}$$

this result also explains why prior enterprises have failed to muster the computational power required to pass over the previously motivated $\hat{\rho}_s \approx 0.15 - 0.20$-threshold (which coincides very well with the $\hat{\rho}_s \approx 0.15 - 0.20$-transition between the two transport scales) from pure drift wave turbulence to large-scale structure formation.
Also, through an analysis of a relation between the zonal flow amplitude and the drift wave intensity, the retroaction of the drift waves on the zonal flows could be examined, and evidence challenging the predator-prey-model was found, with e.g. trapped prey at the positive flows thriving particularly well in close proximity to its predator.
Most importantly though, with the two transport regimes identified and the associated zonal flow transition as well as the general drift wave zonal flow interaction better understood, extensive parameter studies for $\hat{\rho}_s$ were conducted, focusing on the expected consequences of the behavioral asymmetry created due to the drift wave repulsion by the negative flows. Joint studies of the development of the drift wave turbulence pattern, the density gradient and the zonal flow structure resulted in a numerical confirmation of the theoretical considerations, yielding transport bifurcations within all final zonal flow steady states. The negative flows were observed to be steepened and narrowed while the positive flows exhibit unusually broad, shallow plateaus, satisfying conservation of the zonal flow mean value: $\langle v_y = 0 \rangle$. As is shown in Figure 8.3 (originally from Figure 6.1) within a comprehensive presentation of the major findings of Chapter 6, this zonal flow asymmetry is linked to density corrugations, with the gradient being increased around the shear flow domain wall at the negative flow peaks and decreased in the rest of the domain centered on the positive plateaus. Thus, the system was found to exhibit two different transport states, with low diffusivity and high density gradients around the negative flows and vice

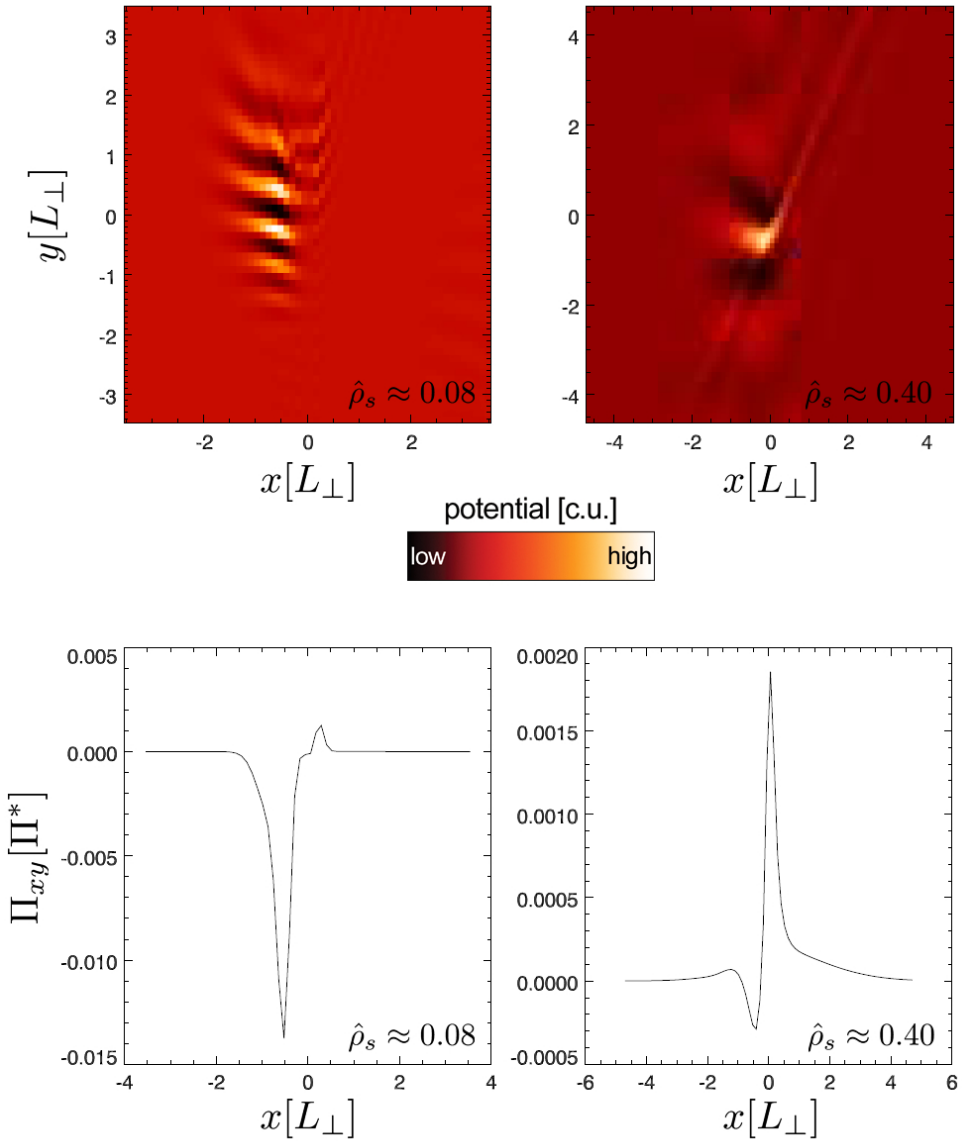

Figure 8.2: As seen in 5.7, the same-time evolution of the radial-poloidal potential and the Reynolds stress (relative to the maximum particle flux) of linear drift wave modes initiated at the resonant surface $x(L_\perp) = 0$ in the presence of a positive flow shear $v_y' > 0$ is analyzed for $\hat{\rho}_s \approx 0.08$ and $\hat{\rho}_s \approx 0.40$ respectively. For low $\hat{\rho}_s$, the uphill acceleration only serves to decelerate the modes at negative radial positions, enabling them to grow stronger due to their vicinity to the resonant surface, causing pronounced negative Reynolds stress while moving downhill. For high $\hat{\rho}_s$, the resonant surface potential is much weaker in comparison to the shear flow potential, leading to uphill acceleration of all modes and thus positive Reynolds stresses, fueling the flows instead of dampening them - thus defining the zonal flow regime.

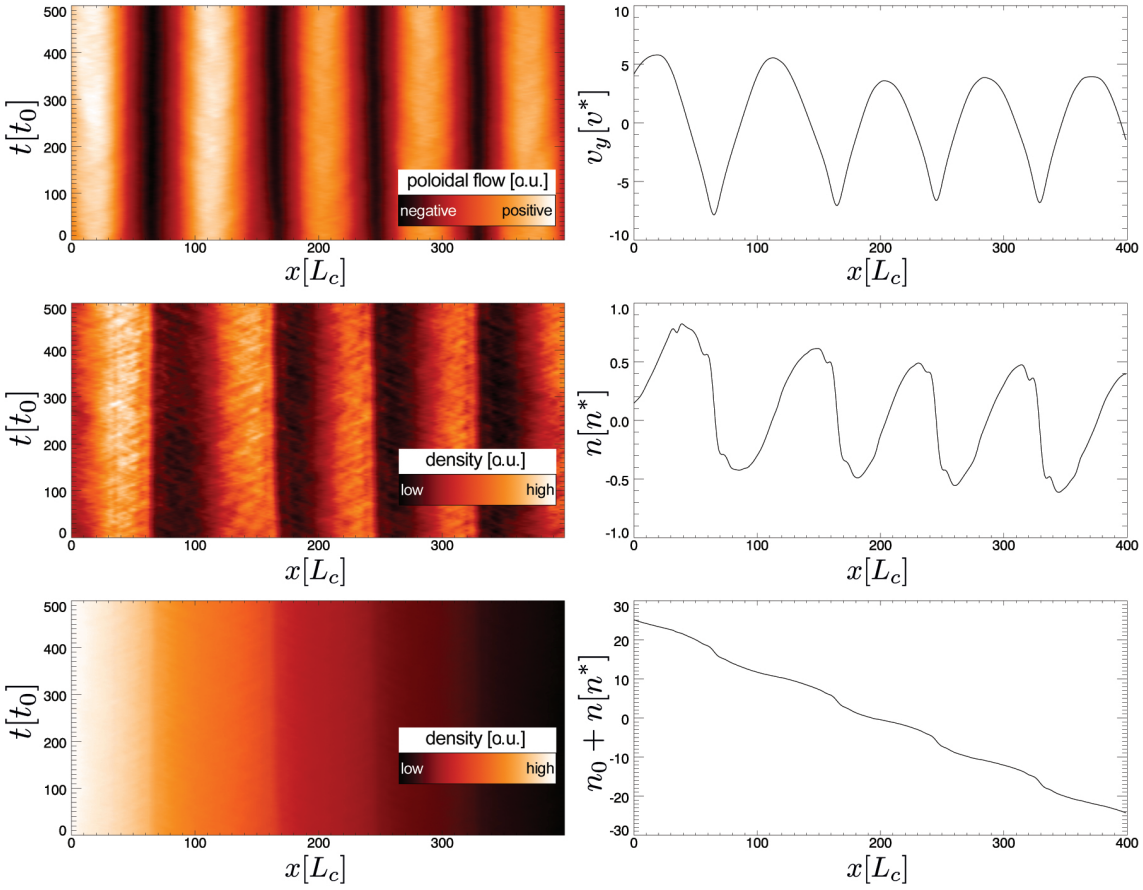

Figure 8.3: Presenting the main results shown in 6.1, for $\hat{\rho}_s \approx 0.28$ (with $\epsilon_n = 0.06$, $\alpha_d = 1.25$ and $s = 1$), poloidal flow v_y, density corrugations n and the total density gradient $n_0 + n$ are shown in a 2D plot yielding radius vs time (left hand side) next to the associated time-averages for all radii (right hand side). All major bifurcation-related findings are visible in this high-resolution run ($n_{x,y} = 512$, $L_{x,y} = 64$): Flow asymmetry - with flattened positive flows and steepened negative flows - and, most importantly, a corrugation on top of the density gradient, associated with steepened areas around the negative flow domain wall.

versa high diffusivity and low density gradients around the positive flows: A transport bifurcation. As seen in (6.1) and (6.2), this effect is strongly noticeable, with typical values for the flow asymmetries and density gradients $n' = \partial_x n$ of

$$|v_{y,min}| \approx 2 \cdot |v_{y,max}| \qquad n'|_{v_{y,min}} \approx 2 \cdot n'|_{v_{y,max}} \tag{8.5}$$

while remaining overall momentum-invariant according to $\langle v_y \rangle = 0$ (due to sharpened negative flows and broadened positive flows on top of a triangular flow pattern corresponding

with the maximum flow shear which does not eclipse the drift wave growth rate). These bifurcations remain robust under a wide variety of distortions; any forced short-term alteration is followed by a swift return to the asymmetric steady state on the transport time scale. While the density corrugations survive even under a continuous artificially symmetrical flow pattern (only disappearing when no flows are present at all), it was shown in Figure 6.2 that the zonal flow asymmetry vanishes when confronted with a density gradient which is kept constant artificially, rendering the asymmetric flows a subdominant feature of the more basic density corrugations. Flow asymmetry is thus shown to bring about only indirect implications for transport (which is determined by the density gradient) - a result which holds true no matter which $\hat{\rho}_s$ is chosen. Other characteristics are less constant, with the expanded parameter studies including (among others) both the fluctuation and kinetic energy, the orthogonal drift wave spectra with their respective drop-off values as shown in Figure 6.7 and both a measure for the mean zonal flow amplitude and the mean flow asymmetry, where applicable (depicted in Figure 6.4). Turbulent energy declines self-similarly within the entire $\hat{\rho}_s$-spectrum, while the simultaneous increases in the flow energy turned out to be less pronounced. Combined, flow energy reaches the same order of magnitude as the turbulent energy as soon as the transition from the chaotic flow onset to ordered zonal flows is achieved. The drop-off value $k_{y,fall}$ of the spectra - beyond which their shape bends from a white noise plateau above the scale of the fluctuations to a polynomial cascade (the smoothness of which was used as one of several tests for the sufficiency of the employed numerical resolution, next to e.g. the convergence of the turbulent transport) - stays constant in the turbulence regime (in units of ρ_s) as well as in the zonal flow regime (in units of $L_\perp$). Accordingly, $k_{y,fall} \cdot \rho_s < 1$ holds true always, supporting the previous insight that drift modes beyond $k_{y,fall} \cdot \hat{\rho}_s \approx 1$ - in dimensionless $\hat{\rho}_s$-units for $k_{y,fall}$ - exhibit next to zero growth (this could, however, also be caused by suppressed modes). The exponent e_k for the self-similar decay of the spectra increases sublinearly with $\hat{\rho}_s$ in the zonal flow regime (6.5) while remaining constant for low values of $\hat{\rho}_s$ (6.6), with a smooth transition in between:

$$\Delta e_k|_{\hat{\rho}_s \gtrsim 0.15-0.20} \propto (\Delta\hat{\rho}_s)^{0.6} \qquad \Delta e_k|_{\hat{\rho}_s \lesssim 0.15-0.20} \propto (\Delta\hat{\rho}_s)^{0.0} \tag{8.6}$$

While the flow wavelength is not strongly prescribed intrinsically (in contrast to ITG-based zonal flows) and while the flow amplitude was found to grow and finally saturate under an increasing $\hat{\rho}_s$, the flow asymmetry actually decreases with higher values of $\hat{\rho}_s$, as seen in Figure 6.5. The same holds true for the density corrugations, rendering the transport bifurcations the more pronounced the closer they get to the transitional value $\hat{\rho}_s \approx 0.15 - 0.20$. Within the zonal flow regime, all parameters scale with ρ_s as expected. Further connections with theory are derived by analyzing the correlation between drift wave intensity and peak flow amplitude, yielding the expected low turbulence intensity around the negative flows as well as a quickly-saturated plateau for arbitrarily strong positive flows (Figure 6.6). Finally, a qualitative bifurcation mechanism was developed, based on the paradigm of turbulence repulsion by the negative flows. Accordingly, overall transport balance requires the heightening of density gradients to counteract the reduction in diffusivity, yielding density corrugations, while at the same time radial carry-off of drift

waves fuels Reynolds stresses prior to steady state saturation, resulting in the observed asymmetric flow pattern.
However, one apparent contradiction remained. Radial drift wave streaks (where streaks denote propagating fluctuations in transport measured as local regions of increased density flux, as seen in Figures 6.1 and, more clearly, in 6.9) were observed to propagate downhill, opposite to the flow gradient, apparently contradicting the negative flows' repulsion paradigm. They exhibit an asymmetry in behavior between inwards and outwards directed streaks of their own: While streaks in both directions occur for zero flow gradient - spanning a diagonal net - any increase in the flow gradient makes the uphill streaks become weaker in amplitude and fewer in between, yet also faster in comparison to their downhill counterparts (Figure 6.10). These effects, as well the streak generation itself, are neither caused by a Galilei shift nor artificial numerical effects. Instead, it could be verified via a tracking routine shown in Figure 6.14 that these streaks are in fact identical to the turbulent drift wave eddies associated with the density corrugations (holding the density gradient constant removes all counter-propagation). Subsequently, only four possible explanations remain: Amplification via shear flow interaction (which only occurs for high wavenumbers, while generally leading to too small growth rates as $k_x \to -\infty$), acceleration in the gradient direction (which is impossible due to a ceiling $max(v_{gr,x})$ being reached soon), scattering (which occurs for high enough drift wave intensity, where the drift waves begin to resemble shear flow optics for $k\rho_s \gtrsim 1$) and transport effects. The characteristics of the streaks' backscattering process were found to be consistent with the observed downhill movement. However, this picture proves incomplete: For a constant density profile, the streak direction reverses, matching the initial expectations. It is only the corrugations in the density profile which cause the apparent contradiction by displacing the transport peak to such a degree that it actually stabilizes the density corrugations instead of destroying them, effectively reversing the direction in which the streaks flow - rendering the apparent contradiction a corrugation-caused transport effect.

The obtained bifurcation picture has far-reaching consequences, since zonal flows appear in a large number of real-world applications, ranging from fusion plasmas to atmospheric, submarine or even solar modes. Several characteristics of the bifurcations in this work are suspected to possibly play a role in confinement, chiefly the increase in flow shear (strongly exceeding flow shear levels under bifurcation-free symmetric flow conditions) occurring around the negative zonal flows, as well as shear flow stalling effects. Under the right device parameters, coming in at just above the transitional value of $\hat{\rho}_s$, the resulting shearing effect might even be sufficient to cut off significant portions of the radially propagating drift wave turbulence. While experimental evidence for the characteristics of drift wave-based zonal flows is still scarce, a mid-term goal for experimentalists was derived, proposing to attain the transitional value of $\hat{\rho}_s$ in order to confirm (or refute) the existence of the numerically and analytically discovered bifurcations. Atmospheric zonal flows, on the other hand, are more accessible via empirical methods. Similarities between these two systems were discussed, citing geostrophic modes, Coriolis forces and pressure forces as the atmospheric counterparts to drift waves, magnetic fields and density gradients in a plasma.

The consequences of conveying such bifurcations to planetary atmospheres (as well as numerous other astrophysical systems such as protoplanetary disks or interstellar nebulae) were then examined. Due to the high rotation speeds on Jovian planets, their zonal flows exert a substantial amount of control over their respective body's climate. Consequently, any transport bifurcation in these systems would have a strong impact, possibly correlating with two severely different climate states. Further research - including the creation of a high-resolution fluid code for gas giants - might thus prove to be the first step towards a comprehensive and global climate forecast for Jupiter. But zonal flows are not limited to gas giants or outer space. Albeit being weaker than their Jovian counterparts, the globe-spanning jet streams on our home planet do still exert a considerable amount of influence on its climate. Therefore, atmospheric flow bifurcations could even have implications for climate change on Earth itself.

Appendix A

Turbulent transport measurements

Table A.1: Turbulent transport in units of $L_\perp$

$\hat{\rho}_s$	0	5.55e-4	2.22e-3	8.88e-3	1.78e-2	3.55e-2	5.02e-2
$\langle nv_x \rangle_{L_\perp}$	0.1459	0.1439	0.1427	0.1432	0.1419	0.1407	0.1363
$\hat{\rho}_s$	0.071	0.100	0.142	0.169	0.201	0.239	0.284
$\langle nv_x \rangle_{L_\perp}$	0.1303	0.1209	0.1070	0.0976	0.0868	0.0672	0.0527
$\hat{\rho}_s$	0.337	0.402	0.438	0.478	0.521		
$\langle nv_x \rangle_{L_\perp}$	0.0407	0.0299	0.0261	0.0222	0.0186		

Table A.2: Turbulent transport in units of ρ_s

$\hat{\rho}_s$	0	5.55e-4	2.22e-3	8.88e-3	1.78e-2	3.55e-2	5.02e-2
$\langle nv_x \rangle_{\rho_s}$	-	9.45e-8	1.51e-6	2.42e-5	8.87e-5	1.82e-4	3.41e-4
$\hat{\rho}_s$	0.071	0.100	0.142	0.169	0.201	0.239	0.284
$\langle nv_x \rangle_{\rho_s}$	6.52e-4	1.21e-3	2.16e-3	2.79e-3	3.51e-3	3.84e-3	4.25e-3
$\hat{\rho}_s$	0.337	0.402	0.438	0.478	0.521		
$\langle nv_x \rangle_{\rho_s}$	4.62e-3	4.83e-3	5.01e-3	5.07e-3	5.05e-3		

Bibliography

[1] F Wagner, G Becker, K Behringer, and D Campbell. Regime of improved confinement and high beta in neutral-beam-heated divertor discharges of the ASDEX Tokamak. *Physical Review Letters*, (49):1408–1412, 1982.

[2] J Wesson. *Tokamaks*. Oxford University Press, 2004.

[3] B Lehnert. Experimental evidence of plasma instabilities. *Plasma Physics*, 301, 1967.

[4] FL Hinton. Theory of plasma transport in toroidal confinement systems. *Reviews of Modern Physics*, 48:239–308, 1976.

[5] J Hugill. Transport in tokamaks – a review of experiment. *Nuclear Fusion*, 331, 1983.

[6] PC Liewer. Measurements of microturbulence in tokamaks and comparisons with theories of turbulence and anomalous transport. *Nuclear Fusion*, 543, 1985.

[7] A. J. Wootton, B. A. Carreras, H. Matsumoto, K. McGuire, W. A. Peebles, Ch. P. Ritz, P. W. Terry, and S. J. Zweben. Fluctuations and anomalous transport in tokamaks. *Physics of Fluids B: Plasma Physics*, 2(12):2879, 1990.

[8] AA Galeev and SS Moiseev. The theory of the stability of non-uniform plasma and anomalous diffusion. *Plasma Physics*, 645, 1964.

[9] B Coppi and MN Rosenbluth. Instabilities due to temperature gradients in complex magnetic field configurations. *Physics of Fluids*, 10:582–587, 1967.

[10] F Wagner. Transport in toroidal devices-the experimentalist's view. *Plasma physics and controlled fusion*, 1321, 1993.

[11] P H Diamond, S-I Itoh, K Itoh, and T S Hahm. Zonal flows in plasma - a review. *Plasma Physics and Controlled Fusion*, 47(5):R35–R161, 2005.

[12] W Horton. Spectral distribution of drift-wave fluctuations in tokamaks. *Physical Review Letters*, 37(x):1269–1272, 1976.

[13] A Hasegawa. Stationary spectrum of strong turbulence in magnetized nonuniform plasma. *Physical Review Letters*, 39(4):205–208, 1977.

[14] A Hasegawa and K Mima. Pseudo-three-dimensional turbulence in magnetized nonuniform plasma. *Physics of Fluids*, 21(1):87, 1978.

[15] T Stoltzfus-Dueck and JA Krommes. Steep-gradient tokamak edge turbulence and the nonlinear instability. *Bulletin of the American*, 1(11):1829–1841, 2008.

[16] A Zeiler. *Tokamak edge turbulence*, volume 5. IPP Report 5/88, 1999.

[17] LF Richardson. *Weather prediction by numerical process.* Cambridge University Press, 1922.

[18] GP Williams. Planetary circulations: 2. The Jovian quasi-geostrophic regime. *J. Atmos. Sci*, 36:932–968, 1979.

[19] A Hasegawa. Self-organization of electrostatic turbulence in a cylindrical plasma. *Physical review letters*, 59(14):1581–1584, 1987.

[20] P H Diamond, S-I Itoh, K Itoh, and T S Hahm. Zonal flows in plasma—a review. *Plasma Physics and Controlled Fusion*, 47(5):R35–R161, 2005.

[21] P Kaw, R Singh, and P H Diamond. Coherent nonlinear structures of drift wave. *Plasma Physics and Controlled Fusion*, 51, 2002.

[22] H. Biglari, P. H. Diamond, and P. W. Terry. Influence of sheared poloidal rotation on edge turbulence. *Physics of Fluids B: Plasma Physics*, 2(1):1–4, 1990.

[23] Z Lin, TS Hahm, WW Lee, WM Tang, and RB White. Turbulent transport reduction by zonal flows: massively parallel simulations. *Science*, 281(5384):1835–7, 1998.

[24] FL Hinton. Dynamics of axisymmetric and poloidal flows in tokamaks. *Plasma physics and controlled fusion*, 653, 1999.

[25] K Hallatschek. Transport control by coherent zonal flows in the core/edge transitional regime. *Physical Review Letters*, pages 1–5, 2001.

[26] K. Hallatschek. Turbulent Saturation of Tokamak-Core Zonal Flows. *Physical Review Letters*, 93(6):1–4, 2004.

[27] T S Hahm, M A Beer, Z Lin, G W Hammett, W W Lee, W M Tang, and I Introduction. Shearing rate of time-dependent ExB flow. *Physics of Plasmas*, 6(3), 1999.

[28] C. Z. Cheng and Liu Chen. Unstable universal drift eigenmodes in toroidal plasmas. *Physics of Fluids*, 23(9):1770, 1980.

[29] W Horton. Nonlinear drift waves and transport in magnetized plasma. *Physics Reports*, 192(1-3):1–177, 1990.

[30] W Horton. Drift waves and transport. *Reviews of Modern Physics*, 71(3):735–778, 1999.

[31] V. B. Lebedev, P. H. Diamond, V. D. Shapiro, and G. I. Soloviev. Modulational interaction between drift waves and trapped ion convective cells: A paradigm for the self-consistent interaction of large-scale sheared flows with small-scale fluctuations. *Physics of Plasmas*, 2(12):4420, 1995.

[32] BD Scott. Energetics of the interaction between electromagnetic ExB turbulence and zonal flows. *New Journal of Physics*, 92, 2005.

[33] MA Malkov and PH Diamond. On the stability of drift wave spectra with respect to zonal flow excitation. *Physics of Plasmas*, 8(5), 2001.

[34] K Itoh, SI Itoh, PH Diamond, and TS Hahm. *Physics of PlasmasPlasmas*, 13(5):1–11.

[35] SI Braginskii. Transport processes in a plasma. *Reviews of Plasma Physics*, page 205, 1965.

[36] A Hasegawa. Plasma edge turbulence. *Physical Review Letters*, 50:682–686, 1983.

[37] A Hasegawa. A collisional drift wave description of plasma edge turbulence. *The Physics of fluids*, 27(3):611–618, 1984.

[38] PH Diamond and YB Kim. Theory of mean poloidal flow generation by turbulence. *Physics of Fluids B: Plasma Physics*, (September 1990):1626–1633, 1991.

[39] A Hasegawa and CG Maclennan. Nonlinear behavior and turbulence spectra of drift waves and Rossby waves. *Physics of Fluids*, 22:2122–2129, 1979.

[40] A. Muhm, A. M. Pukhov, K. H. Spatschek, and V. Tsytovich. Interaction of regular structures with small-scale fluctuations in drift-wave turbulence. *Physics of Fluids B: Plasma Physics*, 4(2):336, 1992.

[41] Z. Lin, T. Hahm, W. Lee, W. Tang, and P. Diamond. Effects of Collisional Zonal Flow Damping on Turbulent Transport. *Physical Review Letters*, 83(18):3645–3648, 1999.

[42] Z Lin, TS Hahm, WW Lee, and WM Tang. Gyrokinetic simulations in general geometry and applications to collisional damping of zonal flows. *Physics of Plasmas*, 7(5), 2000.

[43] A. E. Koniges. Structure formation and transport in dissipative drift-wave turbulence. *Physics of Fluids B: Plasma Physics*, 34(9):1925, 1992.

[44] AI Smolyakov, PH Diamond, and M Malkov. Coherent structure phenomena in drift wave-zonal flow turbulence. *Physical review letters*, 84(3):491–4, 2000.

[45] K Itoh, K Hallatschek, S Toda, and H Sanuki. Coherent structure of zonal flow and nonlinear saturation. *J.Phys.Soc.Jpn.*, 73:2921–2923, 2004.

[46] K Itoh, K Hallatschek, SI Itoh, and PH Diamond. Coherent structure of zonal flow and onset of turbulent transport. *Physics of plasmas*, 12(6), 2005.

[47] K. Hallatschek and D. Biskamp. Transport control by coherent zonal flows in the core/edge transitional regime. *Physical Review Letters*, 86(1):1223–1226, 2001.

[48] K Hallatschek. *Interaction of Global and Microscopic Structures in Fusion Plasma Turbulence*. TUM, 2006.

[49] K Hallatschek. Nonlinear three-dimensional flows in magnetized plasmas. *Plasma Physics and Controlled Fusion*, 49(12B):B137–B148, 2007.

[50] M. A. Malkov, P. H. Diamond, and M. N. Rosenbluth. On the nature of bursting in transport and turbulence in drift wave–zonal flow systems. *Physics of Plasmas*, 8(12):5073, 2001.

[51] K Itoh, K Hallatschek, S Toda, and SI Itoh. Collisional effects on coherent structures of zonal flows and turbulent transport. *Plasma physics and controlled fusion*, 46:2004, 2004.

[52] PH Diamond, YM Liang, and BA Carreras. Self-regulating shear flow turbulence: A paradigm for the L to H transition. *Physical review letters*, 72(16):2565–2568, 1994.

[53] PH Diamond and MN Rosenbluth. Dynamics of zonal flows and self-regulating drift-wave turbulence. *17th IAEA Fusion*, 1998.

[54] A. M. Dimits, G. Bateman, M. A. Beer, B. I. Cohen, W. Dorland, G. W. Hammett, C. Kim, J. E. Kinsey, M. Kotschenreuther, A. H. Kritz, L. L. Lao, J. Mandrekas, W. M. Nevins, S. E. Parker, A. J. Redd, D. E. Shumaker, R. Sydora, and J. Weiland. Comparisons and physics basis of tokamak transport models and turbulence simulations. *Physics of Plasmas*, 7(3):969, 2000.

[55] L Chen, Z Lin, and R White. Excitation of zonal flow by drift waves in toroidal plasmas. *Physics of Plasmas*, 7(8):3129, 2000.

[56] M. A. Malkov and P. H. Diamond. Bifurcation and scaling of drift wave turbulence intensity with collisional zonal flow damping. *Physics of Plasmas*, 8(9):3996, 2001.

[57] PH Diamond, S Champeaux, and M Malkov. Secondary instability in drift wave turbulence as a mechanism for zonal flow and avalanche formation. *Nuclear Fusion*, 41(8):1–24, 2001.

[58] EG Highcock, M Barnes, AA Schekochihin, FI Parra, CM Roach, and SC Cowley. Transport bifurcation in a rotating tokamak plasma. *Physical review letters*, 105(21):215003, 2010.

[59] M A Malkov and P H Diamond. Bifurcation and scaling of drift wave turbulence intensity with collisional zonal flow damping. *Physics of Plasmas*, 8(9):3996–4009, 2001.

[60] L Chen and Z Lin. Excitation of zonal flow by drift waves in toroidal plasmas. *Physics of Plasmas*, 7(8):6–9, 2000.

[61] N Mattor. Drift wave propagation as a source of plasma edge turbulence. *Physical review letters*, 72:486–489, 1994.

[62] Eun-jin Kim. Mean shear flows, zonal flows, and generalized Kelvin–Helmholtz modes in drift wave turbulence: A minimal model for L-H transition. *Physics of Plasmas*, 10(5):1698–1704, 2003.

[63] A Zeiler and D Biskamp. Three-dimensional collisional drift-wave turbulence: Role of magnetic shear. *Physics of Plasmas*, 3(November):3947–3956, 1996.

[64] F. H. Busse. Convection driven zonal flows and vortices in the major planets. *Chaos*, 4(2):123–134, 1994.

[65] JD Jackson. *Classical Electrodynamics*. Wiley, 1999.

[66] H Zohm. *Plasmaphysik*. IPP, 2000.

[67] AH Aitken. Particle Drifts in Plasmas. *Report of NRL progress*, 1959.

[68] A Zeiler and JF Drake. Nonlinear reduced Braginskii equations with ion thermal dynamics in toroidal plasma. *Physics of Plasmas*, 4(6):2134–2138, 1997.

[69] F. L. Hinton. Amplitude Limitation of a Collisional Drift Wave Instability. *Physics of Fluids*, 14(1):116, 1971.

[70] FL Hazeltine, RD; Waelbroek. *The Framework of Plasma Physics*. Westview Press, 2004.

[71] AN Kolmogorov. Dissipation of energy in the locally isotropic turbulence. *Dokl. Akad. Nauk SSSR*, 1941.

[72] K. Hallatschek. Ideale Plasmaeffekte - Einführung in die Magnetohydrodynamik. Lecture at TUM, 2012.

[73] J. Candy and R.E. Waltz. An Eulerian gyrokinetic-Maxwell solver. *Journal of Computational Physics*, 186(2):545–581, 2003.

[74] K. Hallatschek and A. Zeiler. Nonlocal simulation of the transition from ballooning to ion temperature gradient mode turbulence in the tokamak edge. *Physics of Plasmas*, 7(6):2554, 2000.

[75] N Guertler. *Predicting zonal flows - The Reynolds-stress response functional for large-scale flows generated by turbulence in magnetized plasmas*. PhD thesis, TUM, 2011.

[76] A Zeiler, D Biskamp, and JF Drake. Three-dimensional fluid simulations of tokamak edge turbulence. *Physics of Plasmas*, 3(8):2951–2960, 1996.

[77] BD Scott. Low frequency fluid drift turbulence in magnetised plasmas. *IPP-Report*, 5(92), 2000.

[78] JF Drake, A Zeiler, and D Biskamp. Nonlinear Self-Sustained Drift-Wave Turbulence. *Physical review letters*, 75(23):4222–4225, 1995.

[79] D.W. Ross and S.M. Mahajan. Are drift-wave eigenmodes unstable? *Physical Review Letters*, 40(5):324–327, 1978.

[80] PN Guzdar, L. Chen, PK Kaw, and C. Oberman. Effect of magnetic shear on dissipative drift-wave instabilities. *Physical Review Letters*, 40(24):1566–1570, 1978.

[81] BD Scott. Self-sustained collisional drift-wave turbulence in a sheared magnetic field. *Physical review letters*, 65(26):3289–3292, 1990.

[82] P. N. Guzdar, R. G. Kleva, and Liu Chen. Shear flow generation by drift waves revisited. *Physics of Plasmas*, 8(2):459, 2001.

[83] K Hallatschek. Condensation of microturbulence-generated shear flows into global modes. *Phys. Rev. Lett.*, (84):5145–5148, 2000.

[84] B Scott. Global consistency for thin flux tube treatments of toroidal geometry. *Phys. Plasmas*, (5):2334, 1998.

[85] Benjamin C Kuo. *Automatic Control Systems*. Wiley, 2003.

[86] G Strang. On the construction and comparison of difference schemes. *SIAM J. Numer. Anal.*, 5(3):506–517, 1968.

[87] Peter J. Catto, Marshall N. Rosenbluth, and K. T. Tsang. Resistive drift-Alfven waves in sheared magnetic fields. *Physics of Fluids*, 22(7):1284, 1979.

[88] W Horton, C Correa, and GD Chagelishvili. On generation of Alfvenic-like fluctuations by drift wave – zonal flow system in large plasma device experiments. *Physics of Plasmas*, 16(9):1–11, 2009.

[89] W Rodi. Examples of calculation methods for flow and mixing in stratified fluids. *Journal of Geophysical Research*, 92(5):5305–5328, 1987.

[90] X Garbet. Introduction to drift wave turbulence modeling. *Fusion science and technology*, 45(2):1–8, 2004.

[91] K Hallatschek and A Kammel. Zonal flow induced bifurcations in first principles sheared-slab resistive drift wave turbulence simulations. *In preparation for Physical Review Letters*, 2012.

[92] A Zeiler, D Biskamp, and J F Drake. Three-dimensional collisional drift-wave turbulence: Role of magnetic shear. *Physics of Plasmas*, 3(3947), 1996.

[93] K Hallatschek. Condensation of microturbulence-generated shear flows into global modes. *Physical Review Letters*, 84:5145–5148, 2000.

[94] R Hager. *Radial propagation of geodesic acoustic modes - Analysis of magnetic geometry, nonlinear and non-Boussinesq properties of oscillating flows.* PhD thesis, TUM, 2011.

[95] AI Smolyakov. Generalized action invariants for drift waves-zonal flow systems. *Physics of Plasmas*, 6(12):4410–4413, 1999.

[96] SJ Camargo and D Biskamp. Resistive drift wave turbulence. *Physics of Plasmas*, 2(1):48–62, 1995.

[97] D Biskamp. Nonlinear instability mechanism in 3D collisional drift-wave turbulence. *Physical review letters*, 74(5):706–709, 1995.

[98] B Hof, J Westerweel, T M Schneider, and B Eckhardt. Finite lifetime of turbulence in shear flows. *Nature*, 443(7107):59–62, 2006.

[99] S Champeaux and P H Diamond. Streamer and zonal flow generation from envelope modulations in drift wave turbulence. *Physics Letters A*, 288(September):214–219, 2001.

[100] A Kendl. *Driftwellen in Helias-Konfigurationen.* PhD thesis, TUM, 2000.

[101] T. Windisch, O. Grulke, and T. Klinger. Radial propagation of structures in drift wave turbulence. *Physics of Plasmas*, 13(12):122303, 2006.

[102] A. Fujisawa, K. Itoh, H. Iguchi, K. Matsuoka, S. Okamura, A. Shimizu, T. Minami, Y. Yoshimura, K. Nagaoka, C. Takahashi, M. Kojima, H. Nakano, S. Ohsima, S. Nishimura, M. Isobe, C. Suzuki, T Akiyama, K. Ida, K. Toi, S.-I. Itoh, and P. Diamond. Identification of Zonal Flows in a Toroidal Plasma. *Physical Review Letters*, 93(16):1–4, 2004.

[103] D. Gupta, R. Fonck, G. McKee, D. Schlossberg, and M. Shafer. Detection of Zero-Mean-Frequency Zonal Flows in the Core of a High-Temperature Tokamak Plasma. *Physical Review Letters*, 97(12):1–4, 2006.

[104] A; et al Fujisawa, A; Itoh, K; Shimizu. Causal relationship between zonal flow and turbulence in a toroidal plasma. *Journal of the Physical Society of Japan*, 76(3)(033501), 2007.

[105] A Fujisawa. A review of zonal flow experiments. *Nuclear Fusion*, 49(1):013001, 2009.

[106] M Ramisch, F Greiner, N Mahdizadeh, K Rahbarnia, and U Stroth. Observation of large-scale coherent structures under strong ExB shear in the torsatron TJ-K. *Plasma Physics and Controlled Fusion*, 49(6):777–789, 2007.

[107] M. Ramisch, N. Mahdizadeh, U. Stroth, F. Greiner, C. Lechte, and K. Rahbarnia. ρ[sub s] scaling of characteristic turbulent structures in the torsatron TJ-K. *Physics of Plasmas*, 12(3):032504, 2005.

[108] J Liu and PM Goldreich. Constraints on deep-seated zonal winds inside Jupiter and Saturn. *Icarus*, 196:653–664, 2008.

[109] AI Smolyakov and PH Diamond. Zonal flow generation by parametric instability in magnetized plasmas and geostrophic fluids. *Physics of Plasmas*, 7(5):150–152, 2000.

[110] M Salimullah, M Salahuddin, and A A Mamun. Low-frequency drift wave instabilities in a magnetized dusty plasma. *Astrophysics and Space Science*, 205337(205337):215–222, 1999.

[111] Leonid Rudakov and Gurudas Ganguli. Magnetodynamics of a multicomponent (dusty) plasma. II. Magnetic drift waves in an inhomogeneous medium. *Physics of Plasmas*, 12(4):042111, 2005.

[112] P.K. Shukla and L. Stenflo. Generation of zonal flows in nonuniform rotating astrophysical fluids. *Physics Letters A*, 308(4):280–284, 2003.

[113] O Chedia, J Lominadze, and G Machabeli. Generation of Crab Nebulae Wisps by Plasma Drift Instability. *The Astrophysical Journal*, 10:313–317, 1997.

[114] Anders Johansen. The role of magnetic fields for planetary formation. *Proceedings of the International Astronomical Union*, 4(S259):249, 2009.

[115] SS Davis and DP Sheehan. On the persistence of small regions of vorticity in the protoplanetary nebula. *The Astrophysical Journal*, 10(1999):494–503, 2000.

[116] D P Sheehan. Rossby Wave Propagation and Generation in the Protoplanetary Nebula. *Icarus*, 248:238–248, 1999.

[117] M Yamamoto, M; Takahashi. The fully developed superrotation simulated by a general circulation model of a venus-like atmosphere. *J. Atmos. Sci*, 60(3):561–574, 2003.

[118] MJ Thompson. The Internal Rotation of the Sun. *Annual Review of Astronomy and Astrophysics*, 41(1):599–643, 2003.

[119] Richard D. Smith and James C. McWilliams. Anisotropic horizontal viscosity for ocean models. *Ocean Modelling*, 5(2):129–156, 2003.

[120] PB Rhines. *Rossby waves*. Enyclopedia of Atmospheric Sciences, 2002.